

S30
MAT

T299

INVESTIGATIONS OF TRANSPORT AND MAGNETIC PROPERTIES OF POLYANILINE NANOSTRUCTURES

**A thesis submitted in partial fulfillment of the
requirements for the degree of
Doctor of Philosophy**

Chandrani Nath

Registration No. 013 of 2011



**Department of Physics
School of Sciences
Tezpur University
Tezpur - 784 028, Assam, India**

February, 2014

Investigations of transport and magnetic properties of polyaniline nanostructures

Abstract

Traditionally, polymers have been considered and used as electrical insulators. The concept of polymers as insulators changed only after the discovery of high conductivity in polyacetylene, a conjugated organic polymer, in the year 1977 by A.J. Heeger, A.G. MacDiarmid and H. Shirakawa. This revolutionary discovery opened up new areas of research in similar materials. Thereafter, many new materials have been synthesized, designed and implemented in a variety of applications. The last 40 years have witnessed tremendous development in this field from both fundamental and technological viewpoints.

In recent times, conducting polymer nanostructures such as nanofibers, nanotubes and nanoparticles have been receiving great attention in nanoscience and nanotechnology, as they provide opportunities to develop new and efficient materials. The properties of conducting polymer nanostructures get modified due to an enhanced surface to volume ratio and finite size-effects. The nanostructured conducting polymers are much more complex systems as compared to their bulk counterparts and the charge transport in these materials gets affected by the quantum size-effects. Despite the attractive progress in the area of conducting polymer nanostructures, both in terms of basic science and technological viewpoints, a better understanding of the transport mechanism in these low dimensional systems is crucial to successful fabrication of efficient nanoscale devices. Moreover, nanodomain components of higher conductivity are inherent to conducting polymer nanostructures as compared to their bulk counterparts, indicating that nanodimensional control of synthesis improves the conducting properties of these materials. Besides charge transport, thermal

transport is a vital aspect that has to be focused while designing devices. It provides valuable information concerning thermal management issues for implementing these materials in sophisticated devices.

Among the family of organic conducting polymers, polyaniline (PANI) is one of the most important candidates for research, as well as for a wide range of applications owing to its many unique properties. The most significant properties are easy processability, high yield, simple protonic acid doping, environmental stability, relatively high levels of conductivity and inexpensive monomer. Above all, stable nanostructures of PANI with tunable morphologies can be readily synthesized using the chemical oxidative polymerization method by adjusting the reaction conditions and parameters.

The present thesis is a description of the transport properties in the dynamic research field of conducting polymer nanostructures, in general, and PANI nanostructures, in particular. We have synthesized different nanostructures of PANI, viz., hydrochloric acid (HCl) doped nanofibers and nanoparticles, dodecyl benzene sulfonic acid (DBSA) doped nanoparticles and camphor sulfonic acid (CSA) doped nanotubes by interfacial polymerization and self-assembly methods. The nanostructures have been characterized by X-ray diffraction (XRD), high resolution transmission electron microscopy (HRTEM), Fourier transform infrared spectroscopy (FTIR) and Raman spectroscopy. Different transport properties, namely, dc conductivity, magnetoresistance, current-voltage characteristics, thermal conductivity as well as thermodynamic property, viz., specific heat have been elaborately studied in a wide range of temperature from 5 - 300 K. Magnetization, as a function of magnetic field and temperature has also been investigated elaborately. The dependence of the properties on the dopant type and doping level, and also on the morphology of the nanostructures has been investigated.

The thesis contains eight chapters, each of which is divided into several sections and sub-sections. **Chapter 1** begins with an overview of the exciting and emerging field of conducting polymers with an emphasis on conducting

polymer nanostructures. The basic characteristics of conducting polymers have been discussed in this chapter. Introduction of charge carriers as a result of doping, charge transport and the influence of disorder on the charge transport have also been reviewed. The potential applications of the new research field of conducting polymer nanostructures have been presented briefly. The structure, doping and charge carriers of PANI have been concisely reviewed. At the end of the chapter, scope of the thesis along with the statement of the thesis problem, and the major objectives of the present work has been spelt out.

Chapter 2 embodies the description of the various models and mechanisms proposed to explain the observed charge transport in disordered organic semiconductors. This chapter includes a brief discussion on the theories and models used to explain the observed experimental findings in the present thesis. The models employed to explain the heat transport in amorphous materials have also been described in this chapter.

The properties of the materials used for synthesis of the PANI nanostructures, namely, monomer, oxidant, dopants, solvents and other reagents are presented in **Chapter 3**. The formation mechanism of the nanostructures by interfacial polymerization and self-assembly method has been described together with the elaboration of the synthesis route in block diagrams. The specifications of the various characterization techniques, viz., XRD, HRTEM, FTIR and Raman spectroscopy have been mentioned. The experimental setups and methods used to study the different transport properties i.e., dc conductivity, magnetoresistance, current-voltage characteristics, thermal conductivity and thermodynamic property i.e., specific heat are highlighted. The details of the measurement of magnetic properties have also been discussed.

Electrical and thermal transport, and magnetic properties of PANI nanostructures constitute the core of the present thesis which have been dealt with in **Chapters 5, 6 and 7**, respectively. However, for complete analysis and understanding of the electrical, thermal and magnetic properties of PANI nanostructures, structural characterizations such as XRD, HRTEM and

spectroscopic characterizations such as FTIR and Raman have been separately discussed in **Chapter 4**. The morphological studies to determine the shape, size and size distribution of the nanostructures were performed using HRTEM. XRD studies were carried out to study the ordering of the PANI chains and the resulting crystallinity of the nanostructures. XRD studies reveal the differences in the chain ordering due to the morphology of the nanostructures and the nature of the dopant used. Raman spectroscopy provides information regarding the crystalline structure and oxidation state of PANI in the present nanostructures. The variations in chemical interactions due to the change in doping level have been revealed by FTIR and Raman spectroscopy.

Chapter 5 deals with the electrical transport properties of the PANI nanostructures. The dc conductivity of the nanostructures has been studied in the temperature range of 5 - 300 K. The different nanostructures of PANI show different conduction mechanisms in the studied temperature range. Among all the nanostructures, CSA doped nanotubes exhibit the highest conductivity for the same concentration of dopant which is attributed to the ordered nature of the PANI-CSA chains. A metal-insulator transition is observed at ~ 20 K for all the nanostructures, as the temperature is increased. The metallic behavior is attributed to the electron-electron interaction effects. In the insulating regime, different mechanisms have been observed for different nanostructures which have been explained using Mott's variable-range hopping (VRH) model among localized states and VRH model among superlocalized states.

Isothermal magnetoresistance measurements have been performed at five different temperatures, viz., 30 K, 50 K, 100 K, 200 K and 300 K in the magnetic field range of 0 - 8 T. The magnetoresistance curves show a transition from positive to negative value as the temperature is increased above around 100 K, which is explained using the bipolaron model. The temperature dependent current-voltage characteristic measurements of PANI nanostructures were carried out in the temperature range of 80 - 300 K. Bulk-controlled space-charge-limited conduction (SCLC) mechanism prevails in the higher voltage (>

1 V) region while the Ohmic conduction dominates the lower voltage (< 1 V) region of the nanostructures. Trap-free SCLC controls the charge transport in the nanostructures. Moreover, the field and temperature dependence of mobility exhibit the universal Poole-Frenkel behavior. The influence of charge trapping centers in the form of energetic and structural (positional) disorders on the charge transport has been investigated in detail. The energetic disorder parameter, positional disorder parameter and inter-site distance have been extracted employing the uncorrelated and correlated Gaussian disorder models, and compared as a function of doping level and dopant type.

The thermal transport property, namely, thermal conductivity and thermodynamic property, viz., specific heat as a function of temperature have been investigated in **Chapter 6** to gain an insight into the heat carrying modes in the PANI nanostructure systems. The thermal conductivity measurements were performed in the temperature range of 10 - 300 K. The temperature dependence of thermal conductivity exhibits a peak in the low temperature region at ~ 30 K imitating crystalline materials, while in the high temperature region (> 100 K), thermal conductivity increases quasi-linearly with temperature similar to that observed in amorphous solids, such as metallic glasses. With doping, the peak value decreases, which is attributed to the defects introduced in the form of dopant counterions. The low-temperature thermal conductivity results thus reveal crystalline nature while the high-temperature data confirm the amorphous nature of the material, suggesting the order-disorder model for conducting PANI. Extended acoustic phonons dominate the low-temperature (< 100 K) heat conduction, while localized optical phonon hopping, assisted by the extended acoustic modes, account for the high-temperature (> 100 K) heat conduction. The specific heat measurements were carried out in the temperature range of 158 - 300 K. The specific heat increases rapidly upto ~ 200 K. Above 200 K, the specific heat increases gradually to a saturation value.

The magnetic properties of the nanostructures have been dealt with in **Chapter 7**. The temperature dependence of magnetic susceptibility of the

nanostructures has been measured at 10 kOe magnetic field in the temperature range of 2 - 300 K. The nanostructures exhibit a transition from Curie-type to Pauli-type paramagnetism at ~ 50 K. The Curie susceptibility arises from the localized spins in the amorphous regions while the Pauli susceptibility comes from the delocalized spins in the crystalline regions. From the Pauli susceptibility, density-of-states at the Fermi level has been extracted and compared for the different doped nanostructures. Magnetization as a function of magnetic field has been performed in the field range of 0 - 70 kOe at 10 K. With increasing magnetic field, magnetization increases almost linearly at low magnetic fields (upto 10 kOe). However, at higher magnetic fields (> 10 kOe) magnetization deviates from the linear behavior, which is attributed to the enhanced diamagnetic contribution of atomic core and/or Langevin function parameter that adds non-linearity to the magnetic behavior at higher field values.

Chapter 8 summarizes the major conclusions drawn from the present work. The morphology and, more importantly, the dopant type and doping level are found to significantly affect the transport and magnetic properties of the PANI nanostructures. Different charge transport behaviors are observed for the different nanostructures, viz., nanofibers, nanoparticles and nanotubes. The other major contribution of the present thesis is the thermal conductivity studies, as these have not been explored earlier. At the end of this chapter, the scope of further studies in the field of conducting polymer nanostructures has been mentioned briefly.

Declaration

I hereby declare that the thesis entitled “**Investigations of transport and magnetic properties of polyaniline nanostructures**”, submitted to the School of Sciences, Tezpur University in partial fulfillment of the requirements for the award of the degree of Doctor of Philosophy in Physics is a record of original research work carried out by me. Any text, figures, theories, results or designs that are not of my own devising are appropriately referenced in order to give due credit to the original author(s). All the sources of assistance have been assigned due acknowledgement. I also declare that neither this work as a whole nor a part of it has been submitted to any other university or institute for any degree, diploma, associateship, fellowship or any other similar title or recognition.

Date: 10.02.2014

Place: Tezpur

Chandrami Nath
(Chandrami Nath)

Department of Physics

School of Sciences

Tezpur University

Tezpur-784028, Assam, India



Tezpur University

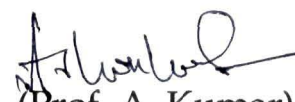
Certificate

This is to certify that the thesis entitled "**Investigations of transport and magnetic properties of polyaniline nanostructures**", submitted to the School of Sciences, Tezpur University in partial fulfillment of the requirements for the award of the degree of Doctor of Philosophy in Physics is a record of original research work carried out by **Ms. Chandrani Nath** under my supervision and guidance.

All help received by her from various sources have been duly acknowledged.

No part of the thesis has been submitted elsewhere for award of any other degree.

Signature of Supervisor:



(Prof. A. Kumar)

Designation: Professor

School: Sciences

Department: Physics

Date: 10.02.2014

Place: Tezpur-784028, Assam, India

Dedicated to

Maa
&
Baba

Acknowledgements

Time flies and it certainly does! Five years of PhD are coming to an end and although this thesis bears my name, this work involves very valuable contributions from a number of people. Hence, I would like to take this opportunity to express my gratitude to all.

First and foremost, I would like to acknowledge and extend my deep sense of gratitude to my thesis supervisor Prof. Ashok Kumar for his constant support, encouragement and guidance which has made the completion of this thesis possible. Through his endless enthusiasm for the subject matter, he was able to push me to achieve things which I initially believed impossible. He provided an academic environment of intellectual enrichment, advice, and stimulation to excel, and the lessons I learned under his guidance will serve me well in the future.

I would like to acknowledge UGC-DAE CSR, Indore and IUAC, New Delhi for the low temperature experiments. I sincerely acknowledge Dr. Alok Banerjee, Dr. Rajeev Rawat and Dr. Gunadhior Singh Okram for the magnetic and electrical transport measurements at UGC-DAE CSR, and for the many valuable comments that improved my knowledge about the subject. I extend my thanks to Dr. Vasant Sathe of UGC-DAE, CSR for the Raman spectroscopy measurements. I would like to extend my sincere gratitude to Dr. K. Asokan for his help and valuable comments during the current-voltage characteristic measurements at IUAC. I take this opportunity to acknowledge Prof. Yung-Kang Kuo of National Dong Hwa University, Taiwan for the thermal conductivity and specific heat measurements. Special thanks to Mr. Kranti Kumar Sharma and Mr. Sachin Kumar Dabaray of UGC-DAE CSR, Indore and Dr. Jitendra Pal Singh of IUAC for their help during the experiments.

I would like to thank Mr. Joston P. Nongkynrih of SAIF, NEHU, Shillong for helping me with the HRTEM experiments. I am grateful to Mr. Prakash Kurmi for the XRD measurements and Mr. Pranab Mudoj for the FTIR measurements. I would also like to acknowledge the Department of Chemical Sciences and the Department of Molecular Biology and Biotechnology, Tezpur University for co-operation to characterize some of the samples on various aspects.

I appreciate having capitalized on this great opportunity given to me at Tezpur University. The facilities at Tezpur University have allowed me to enhance my experience both at academic and personal level. I had already been a student at the Department of Physics, Tezpur University for MSc, and I deeply appreciate the constant encouragement and academic support received from all my teachers that motivated me to pursue research in Physics. The technical and office staff of the Department of Physics is highly acknowledged for their timely help on various aspects.

I would like to acknowledge Tezpur University for the institutional fellowship, IUAC, New Delhi for financial assistance (vide project no. UFR-48310) and DST, Government of India for INSPIRE fellowship which helped to carry out my research work and reach this stage.

I would also like to express my appreciation to the past and present members of the Materials Research Laboratory, Department of Physics, Tezpur University: Smriti ba, Somik da, Madhuryya da, Jayanta, Anup da, Parag and Inanendra. Special acknowledgement goes to Jagat and Prakash da.

It gives me immense pleasure to recall the sweet memories which I shared with my friends during this long period. I would like to specially thank Nomita for being such a wonderful friend in both good and bad times. I thank Sovan da for being there as an elder brother who believed and encouraged me in this long winding road. Special thanks to friends and colleagues: Saurav, Nayanmani, Runjun, Nibedita, Priyanka, Susmita, Rizwin, Kashmiri, Sayan da, Biswajit da, Sikha ba, Bondita ba, Madhulekha ba, Mayuri ba and Mahmuda ba. I am always thankful to my ex-roommate Simran for being such a caring friend. I sincerely acknowledge the help extended by the Researchhelp Google Group members.

I would like to specially mention the family I met during my stay at Indore. Thank you so much uncle, aunty, bhaiya, bhabhi and dadi for making me feel at home in an unknown place. I shall always be indebted to Gautam da and boudi for their support and shelter during my experimental work at New Delhi and Indore.

However, reaching this stage has never been an easy path for me. Before entering my PhD, I lost two of my dear ones in life. I lost my Didima who bestowed upon immense caring during my childhood. Subsequently, the sudden demise of my father was another shock

for me. Needless to say, I am indebted to my parents for their unconditional love and support and everything. The encouraging words and blessings of my late father are always motivating me to move ahead in life. My mother has always been a strong lady, and supported and encouraged me to strive towards success. Maa, it is because of your blessings and moral support at every stage of my life that I am able to overcome the hurdles easily, and words are falling short to describe the gratefulness. I sincerely acknowledge the constant support, encouragement and love from my elder sister and brother-in-law. I also thank my little niece whose cute smile refreshed my mind even at times of immense pressure. I extend my heartfelt thanks to my uncles, aunts, cousins and in-laws for their love and support throughout. I want to especially thank my husband for his constant love, support, patience and encouragement, without which I would not have succeeded this far. The long lasting discussions with him have really improved my conceptions and understanding. Thank you for being there whenever I needed. At the end, I thank the Almighty for giving me moral strength and courage to carry out my work.

Date: 10.02.2014

Place: Tezpur

*Chandrani Nath
(Chandrani Nath)*

CONTENTS

<i>a. Abstract.....</i>	<i>i</i>
<i>b. Declaration.....</i>	<i>vii</i>
<i>c. Certificate.....</i>	<i>viii</i>
<i>d. Acknowledgements.....</i>	<i>x</i>
<i>e. Contents.....</i>	<i>xiii</i>
<i>f. List of tables.....</i>	<i>xvii</i>
<i>g. List of figures.....</i>	<i>xxviii</i>
<i>h. List of abbreviations.....</i>	<i>xxiv</i>
<i>i. List of symbols.....</i>	<i>xxvii</i>

CHAPTER 1: Introduction [1-19]

1.1 Conducting polymer.....	1
1.1.1 Band structure.....	3
1.1.2 Doping and charge carriers.....	5
1.2 Charge transport in conducting polymers.....	8
1.2.1 Disorder in conducting polymers.....	8
1.2.2 Role of disorder on charge transport.....	9
1.2.3 Metal-insulator transition.....	11
1.3 Conducting polymer nanostructures.....	12
1.4 Polyaniline (PANI).....	13
1.5 Scope of the thesis and statement of the thesis problem	16

CHAPTER 2: Theoretical aspects [20-43]

2.1 Charge conduction mechanism in disordered organic semiconductors.....	20
2.1.1 Temperature dependence of conductivity.....	21
2.1.1.1 Hopping models.....	21
2.1.1.2 Tunneling models.....	24

2.1.1.3	Heterogeneous model.....	25
2.1.1.4	Metal-insulator transition and localization- interaction model.....	27
2.1.2	Current-voltage characteristics.....	30
2.1.2.1	Ohmic conduction.....	30
2.1.2.2	Space-charge-limited conduction.....	30
2.1.2.3	Poole-Frenkel mobility.....	32
2.1.2.4	Gaussian disorder model.....	33
2.1.3	Magnetoresistance.....	36
2.1.3.1	Positive magnetoresistance.....	36
2.1.3.2	Negative magnetoresistance.....	37
2.1.3.3	Bipolaron model.....	38
2.2	Heat transport mechanism in amorphous materials.....	40
2.2.1	Thermal conductivity.....	41
2.2.2	Thermally activated hopping model.....	42
 CHAPTER 3: Experimental details		[44-61]
3.1	Materials.....	44
3.2	Synthesis of PANI nanostructures.....	46
3.2.1	Synthesis of PANI nanofibers.....	46
3.2.2	Synthesis of PANI nanoparticles.....	48
3.2.3	Synthesis of PANI nanotubes.....	52
3.3	Characterization techniques.....	54
3.3.1	High resolution transmission electron microscopy..	54
3.3.2	X-ray diffraction.....	54
3.3.3	Fourier transform infrared spectroscopy.....	55
3.3.4	Raman spectroscopy.....	55
3.4	Transport property measurement techniques.....	56
3.4.1	DC conductivity and magnetoresistance.....	56

3.4.2	Current-voltage characteristics.....	57
3.4.3	Thermal conductivity.....	58
3.4.4	Specific heat.....	59
3.5	Magnetic property measurement technique.....	60
 CHAPTER 4: Structural and vibrational spectroscopic studies of polyaniline nanostructures		[62-80]
4.1	Introduction.....	62
4.2	Structural characterizations.....	64
4.2.1	High resolution transmission electron microscopy..	64
4.2.2	X-ray diffraction studies.....	69
4.3	Vibrational spectroscopic studies.....	72
4.3.1	Fourier transform infrared spectroscopy.....	72
4.3.2	Raman spectroscopy.....	75
4.4	Summary.....	79
 CHAPTER 5: Electrical transport in polyaniline nanostructures		[81-123]
5.1	Introduction.....	81
5.2	DC conductivity studies.....	85
5.3	Magnetoresistance studies.....	98
5.4	Current-voltage characteristics.....	107
5.5	Summary.....	121
 CHAPTER 6: Thermal transport in polyaniline nanostructures		[124-139]
6.1	Introduction.....	124
6.2	Thermal conductivity studies.....	126
6.3	Specific heat studies.....	136

6.4	Summary.....	138
CHAPTER 7: Magnetic properties of polyaniline nanostructures		[140-149]
7.1	Introduction.....	140
7.2	Temperature dependence of magnetic susceptibility.....	142
7.3	Field dependence of magnetization.....	146
7.4	Summary.....	148
CHAPTER 8: Conclusions and future prospects		[150-157]
8.1	Conclusions.....	150
8.2	Future prospects.....	157
References.....		[158-183]
List of publications.....		[184-185]

List of tables

Table	Caption	Page No.
Table 3.1	Some physicochemical properties of the materials used for synthesis	45
Table 4.1	Characteristic IR bands of doped PANI and their assignments	74
Table 4.2	Characteristic Raman bands of doped PANI and their assignments	77
Table 5.1	Parameters calculated from dc conductivity vs. temperature data in the insulating regime of PANI nanotubes, nanofibers and nanoparticles	96
Table 5.2	Fitting parameters of uncorrelated and correlated Gaussian disorder models	118
Table 6.1	Values of Debye temperature (θ_D) and exponents, n_1 and n_2 related to temperature dependence of κ_{ph} below and above the peak, respectively	130
Table 6.2	Values of the exponent (n_3) determined from the slope of κ_{ph} above 100 K, and the anharmonic coupling (C_{eff}) of the nanostructures	135
Table 7.1	Value of density-of-states at the Fermi level $[N(E_F)]$ and Curie constant (C) of the nanostructures	145

List of figures

Figure	Caption	Page No.
Figure 1.1	Chemical formulae of some important conducting polymers	2
Figure 1.2	The σ -and π -bonds between carbon atoms exhibiting sp^2 hybridization	4
Figure 1.3	Schematic of the formation of energy bands, HOMO and LUMO in conducting polymers	4
Figure 1.4	Schematic of formation of charge carriers and modifications in the band structure of conducting polymers upon doping	7
Figure 1.5	Different oxidation states of PANI	14
Figure 1.6	Schematic representation of doping in PANI	15
Figure 2.1	Schematic illustration of variable-range hopping behavior in the low temperature regime	22
Figure 2.2	Charge hopping process between localized states in a Gaussian DOS	34
Figure 2.3	Schematic illustration of the mechanism of bipolaron model	39
Figure 2.4	Schematic representation of hopping of localized phonons	42
Figure 3.1	Schematic representation of the formation of nanofibers in interfacial polymerization of PANI	47
Figure 3.2	Block diagram of the synthesis route of PANI nanofibers by interfacial polymerization technique	48
Figure 3.3	Block diagram of the synthesis of PANI nanoparticles via soft-template technique	49

Figure 3.4	Schematic of the formation of a nanoparticle in the micellar solution of surfactant	51
Figure 3.5	Block diagram of the synthesis of PANI nanotubes via soft-template technique using CSA	53
Figure 3.6	Schematic of the formation of PANI nanotubes in the micellar solution of CSA	53
Figure 3.7	Image of the setup used for measuring dc conductivity with variation of temperature and magnetic field, and a schematic of four probe measurement	57
Figure 3.8	Photograph of the setup used for measuring current-voltage characteristics	58
Figure 3.9	Schematic of the setup used for measuring thermal conductivity	59
Figure 3.10	Schematic of working principle of a DSC and the image of the DSC instrument used for specific heat measurement	60
Figure 3.11	Image of the SQUID magnetometer used for magnetic property measurements and a schematic of superconducting coil through which sample is scanned	61
Figure 4.1	HRTEM images of PANI nanofibers doped with HCl	64
Figure 4.2	Diameter distributions of PANI nanofibers doped with HCl	65
Figure 4.3	HRTEM images of PANI nanoparticles doped with HCl	65
Figure 4.4	Diameter distributions of PANI nanoparticles doped with HCl	66
Figure 4.5	HRTEM images of PANI nanoparticles doped with DBSA	67
Figure 4.6	Distributions of diameter of PANI nanoparticles	67

	doped with DBSA	
Figure 4.7	HRTEM images of PANI nanotubes doped with CSA	68
Figure 4.8	Distributions of inner and outer diameter of the lowest doped PANI-CSA nanotubes	69
Figure 4.9	Distributions of inner and outer diameter of the highest doped PANI-CSA nanotubes	69
Figure 4.10	X-ray diffraction patterns of HCl doped PANI nanofibers and nanoparticles	70
Figure 4.11	X-ray diffraction patterns of DBSA doped PANI nanoparticles and CSA doped PANI nanotubes	71
Figure 4.12	FTIR spectra of HCl doped PANI nanofibers and nanoparticles	72
Figure 4.13	FTIR spectra of DBSA doped PANI nanoparticles and CSA doped PANI nanotubes	73
Figure 4.14	Raman spectra of HCl doped PANI nanofibers	75
Figure 4.15	Raman spectra of HCl doped PANI nanoparticles	76
Figure 4.16	Raman spectra of DBSA doped PANI nanoparticles	78
Figure 4.17	Raman spectra of CSA doped PANI nanotubes	79
Figure 5.1	Temperature dependence of conductivity for HCl doped PANI nanofibers and nanoparticles	86
Figure 5.2	Temperature variation of conductivity for DBSA doped PANI nanoparticles and CSA doped PANI nanotubes	87
Figure 5.3	Plots of W vs. T for HCl doped PANI nanofibers and nanoparticles	88
Figure 5.4	W vs. T plots of DBSA doped PANI nanoparticles and CSA doped PANI nanotubes	88
Figure 5.5	Two dimensional schematic representations of dopant counterions in between PANI chains	91
Figure 5.6	Schematic illustrations of charge hopping sites in the	92

	nanostructures	
Figure 5.7	$\ln\sigma$ vs. $T^{-1/2}$ plot of the insulating regime of CSA doped PANI nanotubes	93
Figure 5.8	$\ln\sigma$ vs. $T^{-3/7}$ plot of the insulating regime of HCl doped PANI nanofibers	94
Figure 5.9	$\ln\sigma$ vs. $T^{-0.66}$ plots of the insulating regime of HCl doped and DBSA doped PANI nanoparticles	95
Figure 5.10	$MR\%$ of HCl doped PANI nanofibers and nanoparticles at different temperatures	99
Figure 5.11	Temperature dependence of $MR\%$ at $H = 8$ T for HCl doped PANI nanofibers and nanoparticles	99
Figure 5.12	$MR\%$ of DBSA doped PANI nanoparticles and CSA doped PANI nanotubes at various temperatures	100
Figure 5.13	$MR\%$ (at $H = 8$ T) as a function of temperature for DBSA doped PANI nanoparticles and CSA doped PANI nanotubes	100
Figure 5.14	Representative fitting of MR using bipolaron model	105
Figure 5.15	Temperature dependence plots of H_0 for HCl doped PANI nanofibers and nanoparticles	106
Figure 5.16	Temperature variation plots of H_0 for DBSA doped PANI nanoparticles and CSA doped PANI nanotubes	106
Figure 5.17	J - V characteristics of HCl doped PANI nanofibers	108
Figure 5.18	J - V characteristics of HCl doped PANI nanoparticles	109
Figure 5.19	J - V characteristics of DBSA doped PANI nanoparticles	110
Figure 5.20	J - V characteristics of CSA doped PANI nanotubes	111
Figure 5.21	Energy level diagram of Ag-PANI Ohmic contact formation	111
Figure 5.22	Representative J - V characteristics in log-log plots for HCl doped PANI nanofibers and nanoparticles	112
Figure 5.23	Representative plot of the data of space-charge-limited	113

region in the form of logarithm of (Jd^3 / V^2) vs. square root of electrical field $(V/d)^{1/2}$

Figure 5.24	Temperature variation of zero-field mobility (μ_0) for HCl doped PANI nanofibers and nanoparticles	114
Figure 5.25	Variation of zero-field mobility (μ_0) as a function of temperature for DBSA doped PANI nanoparticles and CSA doped PANI nanotubes	114
Figure 5.26	Representative plots of temperature variation of field activation parameter (γ) for HCl doped PANI nanofibers and CSA doped PANI nanotubes	115
Figure 5.27	Plots of $\ln\mu_0$ vs. T^{-2} for HCl doped PANI nanofibers and nanoparticles	116
Figure 5.28	$\ln\mu_0$ vs. T^{-2} plots of DBSA doped PANI nanoparticles and CSA doped PANI nanotubes	116
Figure 5.29	Plots of γ vs. T^{-2} for HCl doped PANI nanofibers and nanoparticles	117
Figure 5.30	γ vs. T^{-2} plots of DBSA doped PANI nanoparticles and CSA doped PANI nanotubes	118
Figure 5.31	γ vs. $T^{-3/2}$ plots of HCl doped PANI nanofibers and nanoparticles	119
Figure 5.32	Plots of γ vs. $T^{-3/2}$ for DBSA doped PANI nanoparticles and CSA doped PANI nanotubes	120
Figure 6.1	Temperature dependence of thermal conductivity for HCl doped PANI nanofibers and nanoparticles	126
Figure 6.2	Temperature dependence plots of thermal conductivity for DBSA doped PANI nanoparticles and CSA doped PANI nanotubes	127
Figure 6.3	Temperature dependence of κ_e for HCl doped PANI nanofibers and nanoparticles	128

Figure 6.4	Temperature dependence plots of κ_e for DBSA doped PANI nanoparticles and CSA doped PANI nanotubes	128
Figure 6.5	Temperature dependence plots of κ_{ph} below 100 K for HCl doped PANI nanofibers and nanoparticles	129
Figure 6.6	Plots of κ_{ph} vs. T below 100 K for DBSA doped PANI nanoparticles and CSA doped PANI nanotubes	129
Figure 6.7	Temperature variation of κ_{ph} above 100 K for HCl doped PANI nanofibers and nanoparticles	133
Figure 6.8	Temperature dependence of κ_{ph} above 100 for DBSA doped PANI nanoparticles and CSA doped PANI nanotubes	134
Figure 6.9	Temperature dependence of specific heat for HCl doped PANI nanofibers and nanoparticles	137
Figure 6.10	Specific heat as a function of temperature for DBSA doped PANI nanoparticles and CSA doped PANI nanotubes	137
Figure 7.1	Temperature dependent variation of magnetic susceptibility for HCl doped PANI nanofibers and nanoparticles	143
Figure 7.2	Temperature dependence plots of magnetic susceptibility for DBSA doped PANI nanoparticles and CSA doped PANI nanotubes	143
Figure 7.3	Magnetization vs. field plots of HCl doped PANI nanofibers and nanoparticles	147
Figure 7.4	Plots of magnetization vs. field for DBSA doped PANI nanoparticles and CSA doped PANI nanotubes	147

List of abbreviations

Abbreviation	Meaning
A	Ampere
APS	Ammonium persulfate
B	Benzenoid
CCD	Charge coupled detector
CGDM	Correlated Gaussian disorder model
cm	centimeter
CSA	Camphor sulfonic acid
CTAB	Cetyl methyl ammonium bromide
DBSA	Dodecyl benzene sulfonic acid
DC (dc)	Direct current
DOS	Density-of-states
DSC	Differential scanning calorimeter
EB	Emeraldine base
emu	Electromagnetic unit
emf	Electromagnetic force
ES	Emeraldine salt
eV	electron Volt
FET	Field-effect transistor
FTIR	Fourier transform infrared spectroscopy
g	gram
GDM	Gaussian disorder model
h	hour
HCl	Hydrochloric acid
HOMO	Highest occupied molecular orbital
HRTEM	High resolution transmission electron microscopy

ID	Inner diameter
ILC	Injection limited conduction
I-V	Current-voltage
J	Joule
K	Kelvin
kOe	kilo Oersted
LB	Leucoemeraldine base
LUMO	Lowest unoccupied molecular orbital
m	meter
meV	milli electron Volt
mg	milligram
ml	milliliter
MIT	Metal-insulator transition
MPMS	Magnetic property measurement system
MR	Magnetoresistance
mT	milli Tesla
nA	nano Ampere
NF	Nanofiber doped with hydrochloric acid
nm	nanometer
NPa	Nanoparticle doped with hydrochloric acid
NPb	Nanoparticle doped with dodecyl benzene sulfonic acid
NT	Nanotube doped with camphor sulfonic acid
OD	Outer diameter
OLED	Organic light emitting diode
OMAR	Organic magnetoresistance
pA	pico Ampere
PA	Polyacetylene
PANI	Polyaniline

PB	Pernigraniline base
PC	Polycarbonate
PF	Poole-Frenkel
PPY	Polypyrrole
PT	Polythiophine
PTM	Particle track etched membrane
Q	Quinoid
s	second
S	Siemens
SCLC	Space-charge-limited conduction
SDS	Sodium dodecyl sulfate
SDBS	Sodium dodecyl benzene sulfonate
SL	Strongly localized
SQUID	Superconducting quantum interference device
SSH	Su, Schrieffer, Heeger
T	Tesla
TAH	Thermally activated hopping
TCR	Temperature coefficient of resistivity
ToF	Time-of-flight
UGDM	Uncorrelated Gaussian disorder model
V	Volt
VRH	Variable-range hopping
W	Watt
XRD	X-ray diffraction
β -NSA	β -naphthalene sulfonic acid
μ A	micro Ampere
μ m	micrometer
Ω	Ohm

List of symbols

Symbol	Meaning
a	Inter-site distance
C	Curie constant
C'	Scaling factor
C_P	Specific heat at constant pressure
C_{eff}	Third-order anharmonic coupling constant
d	Thickness
D	Electronic diffusion coefficient
d_f	Fractal dimensionality
e	Electronic charge
E	Energy
E_c	Mobility edge
E_F	Fermi level energy
E_g	Energy gap or band gap
F	Electric field
h	Planck's constant
H	Magnetic field
H_{lf}	Hydrogen hyperfine field
H_0	Characteristic magnetic field width
I	Current
J	Current density
k_B	Boltzmann constant
l_m	Mean-free path of electron
l_{ph}	Localization length of phonon
L_c	Localization length of electronic wavefunction
L_H	Magnetic length

L_0	Lorenz number
$L(A)$	Langevin function
M	Magnetization
M_s	Saturation value of magnetization
n	VRH exponent
$N(E_F)$	Density-of-states at the Fermi level
r	Distance
R_{hop}	Hopping distance or hopping length
T	Temperature
T_0	Characteristic temperature
v_s	Velocity of sound
V	Voltage
W	Reduced activation energy
z	Number of nearest neighbor chains
χ	Magnetic susceptibility
χ_C	Curie susceptibility
χ^P	Pauli susceptibility
ϵ_0	Permittivity of free space
ϵ_r	Relative permittivity
γ	Field activation parameter
κ	Thermal conductivity
κ_e	Electronic thermal conductivity
κ_{hop}	Thermal conductivity due to hopping of localized phonons
κ_{ph}	Phonon thermal conductivity
λ	Wavelength
μ	Mobility
μ_0	Zero-field mobility
μ_∞	Mobility at infinite temperature

μ_B	Bohr magneton
μ_m	Atomic magnetic moment
θ	Angle of incidence
ρ	Resistivity
ρ_d	Mass density
σ	Conductivity
σ'	Width of Gaussian distribution of sites or energetic disorder parameter
Σ	Structural or positional disorder parameter
ω	Phonon frequency
ω_c	Phonon mobility edge
ξ	Superlocalization exponent
\tilde{F}	Hartree coupling strength parameter
$^{\circ}\text{C}$	Degree celsius
\AA	Angstrom

CHAPTER 1

Introduction

This chapter presents an overview of the exciting and emerging field of conducting polymers with an emphasis on conducting polymer nanostructures. The basic characteristics, introduction of charge carriers, charge transport and influence of disorder on the charge transport of conducting polymers have been discussed. Towards the end, the chapter outlines the scope of the thesis and statement of the thesis problem.

1.1 Conducting polymer

Silicon and similar inorganic semiconductors have conquered the electronics world since the dawn of electronics. Silicon has become an inevitable part of our day-to-day life ranging from home appliances to electronic gadgets employed for entertainment and communication. Traditionally, polymers have been used as passive components, as insulators or in packaging. The concept of polymers as insulators faded away only after the ground-breaking discovery of high conductivity in polyacetylene, an organic conjugated polymer, in the year 1977 by A.J. Heeger, A.G. MacDiarmid and H. Shirakawa [1]. The conductivity of polyacetylene could be increased by more than seven orders of magnitude upon iodine doping. The three pioneers A.J. Heeger, A.G. MacDiarmid and H. Shirakawa were awarded the year 2000 Nobel Prize in Chemistry for the discovery and development of conducting polymers. This discovery opened up new areas of research in the field of organic conjugated polymers and the opportunity for organic polymers to serve as active material in electronics. Although, the initial emphasis was on the conducting properties of these

polymers, later many new materials were developed, which were designed and implemented in a range of applications. Conducting polymers are also known as 'synthetic metals' as they combine the electrical and optical properties of metals with the processing advantage of polymers. These polymers have now become a promising class of technologically important materials serving both fundamental and commercial purposes. The last four decades have witnessed fascinating progress in this field stimulated by the diverse technological applicability of these materials in areas such as molecular electronics [2], electrodes for redox supercapacitors [3, 4], electrochromic displays [5, 6], sensors [7, 8], actuators [9, 10], electromagnetic shielding [11, 12] and non-linear optics [13]. Some of the most significant conducting polymers are shown in Figure 1.1.

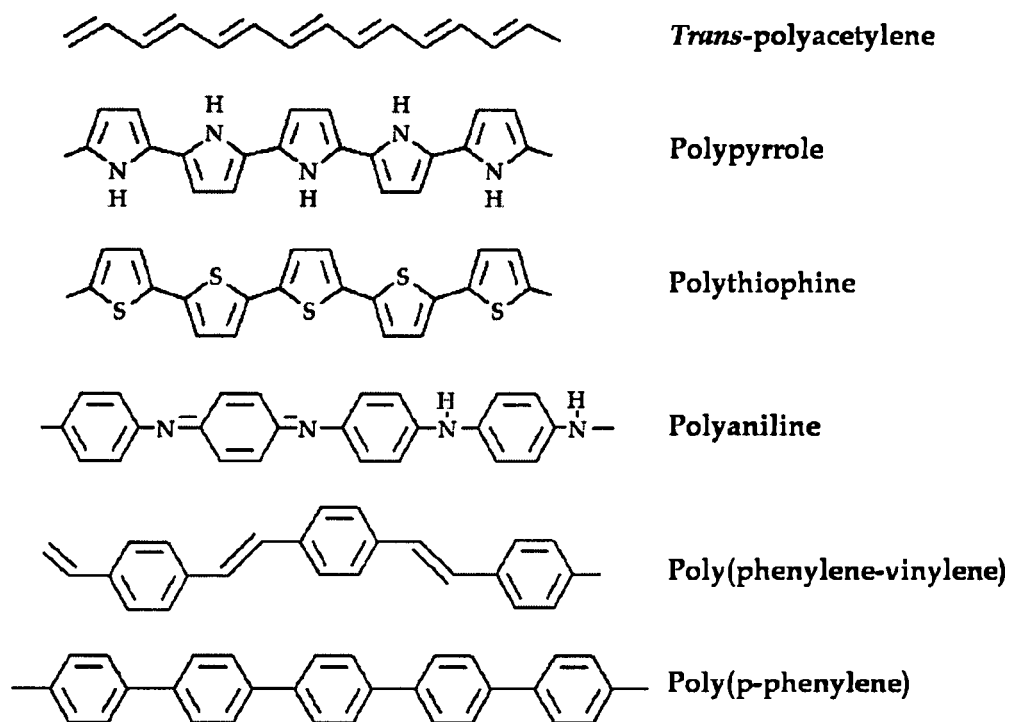


Figure 1.1: Chemical formulae of some important conducting polymers.

The key feature of a conducting polymer is the presence of conjugated bonds i.e., double bonds alternating with single bonds along the polymer chain.

This special conjugation in the chains enables the electrons to delocalize throughout the chain making it conductive.

The conjugated polymers can become conductive only on doping, which means removal or addition of electrons. Doping allows the loosely bound electrons to move across the polymer chains producing electric current. The conductivity of a material is determined by the number of charge carriers and mobility. In polymers, these parameters are determined by the chemical structure and doping. The relationship between chemical structure and conductivity, especially the concept of doping, charge carriers and their transport are discussed in the following sections.

1.1.1 Band structure

The ground state electronic configuration of the six electrons in a carbon atom is $1s^2 2s^2 2p^2$, which gives four valence electrons in the one $2s$ - and three $2p$ -orbitals. These orbitals exhibit different hybridization i.e., sp , sp^2 and sp^3 , each possessing a unique spatial character in different carbon materials. In conventional polymers i.e., 'plastics', the carbon atom is in sp^3 hybridization and all the valence electrons are paired; hence they do not conduct electricity. In conducting polymers, the carbon atom is in sp^2 hybridization which is a mixture of one s - and two p -orbitals. Three of the four valence electrons are in the three sp^2 -orbitals while the fourth electron is in the remaining unhybridized $2p$ -orbital i.e., the $2p_z$ -orbital. The sp^2 -orbitals from different carbon atoms lying on the molecular plane form strong covalent bonds called σ -bonds, which form the backbone of the polymer. The p_z -orbitals which are orthogonal to the molecular plane mix to give weak covalent bonds called π -bonds. The π -bonds form a delocalized electron density above and below the molecular plane which are responsible for the conductivity of the polymer, as the charge carriers move through these bonds. Figure 1.2 shows the σ - and π -bonds in a simple organic molecule ethylene (C_2H_4).

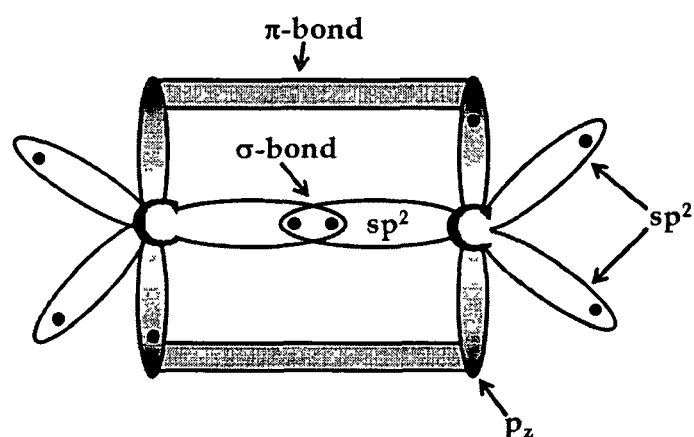


Figure 1.2: The σ - and π -bonds between carbon atoms exhibiting sp^2 hybridization [14].

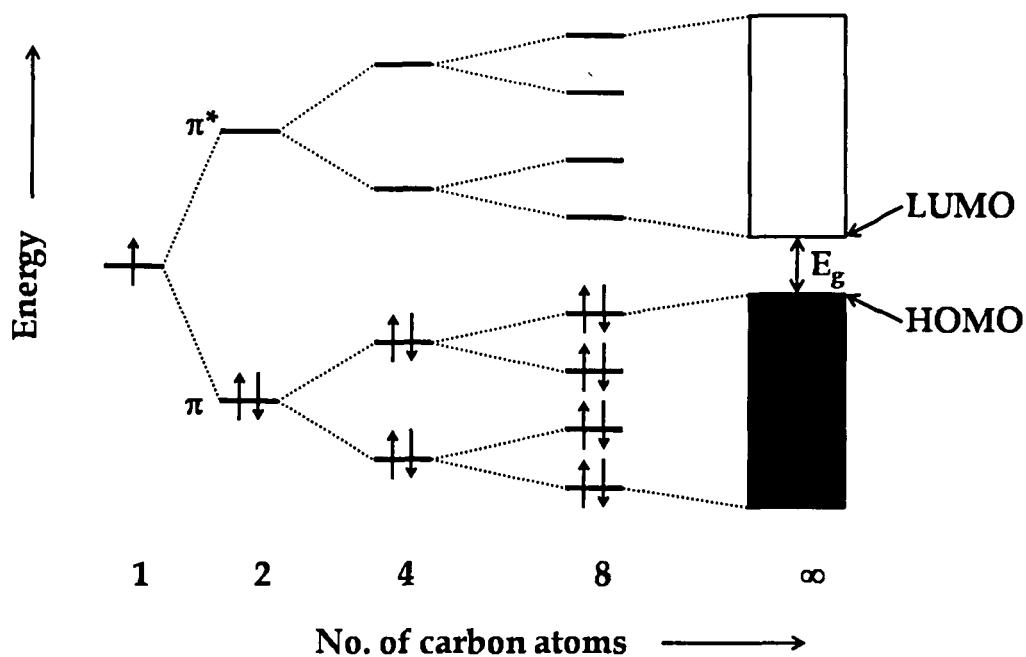


Figure 1.3: Schematic of the formation of energy bands, HOMO and LUMO in conducting polymers.

In a molecule with two sp^2 -hybridized carbon atoms, the interaction between the p_z -electrons results in the formation of two molecular orbitals depending on the sign of the wavefunction of the orbitals – bonding with lower energy (π) and antibonding with higher energy (π^*). Without an excitation, the

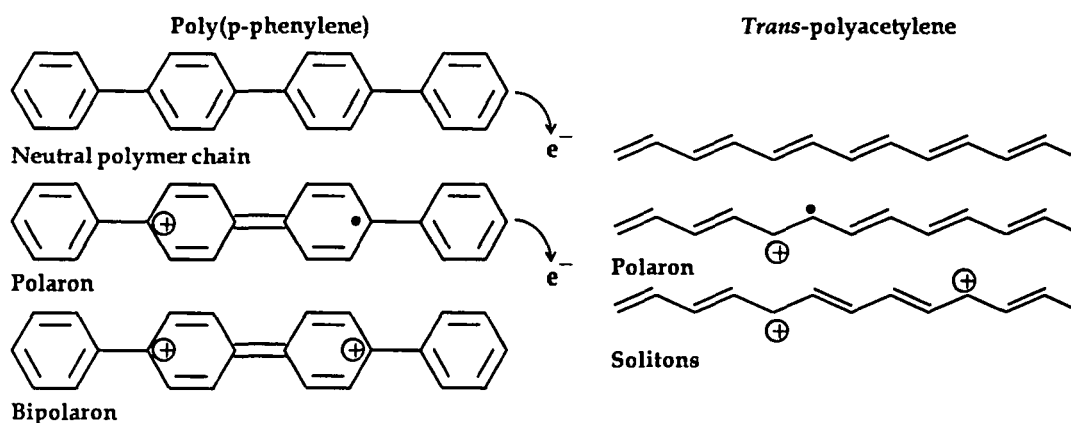
π -orbitals are occupied and the π^* -orbitals are unoccupied. Increasing the carbon atoms in a molecule increases the number of molecular orbitals. When multiple molecules are considered, the energy levels merge to form bands analogous to that of inorganic semiconductors, with the edge of the valence band corresponding to the Highest Occupied Molecular Orbital (HOMO), and the edge of the conduction band corresponds to the Lowest Unoccupied Molecular Orbital (LUMO). Infinite number of sp^2 -hybridized carbon atoms in a chain will lead to the overlapping of the infinite atomic orbitals brought together. Energy splitting results in the formation of molecular orbitals packed densely with infinitesimal energy difference. This would lead to the formation of bands of states without a band gap (energy difference between HOMO and LUMO) i.e., a one-dimensional metal. However, in reality this is not a stable state and undergoes Peierls distortion [15], forming a gap between the bonding and the antibonding states as that of semiconductors. The difference between the energy of HOMO and the energy of LUMO is the energy gap (E_g) of the polymer which is generally in the range of 1.5 - 4 eV. Figure 1.3 is a schematic depiction of the formation of HOMO and LUMO in conducting polymers.

1.1.2 Doping and charge carriers

Conducting polymers in its undoped or neutral state are semiconductors with the π -electrons bound to the π -orbitals creating an alternation of single and double bonds. Conductivity i.e., delocalization of charge along the polymer backbone is achieved by the introduction of charge carriers (addition or removal of electrons) by a process called 'doping'. Typically 'dopant' substances are neutral molecules, or inorganic and organic salts that can form ions. Introduction of the dopant species (in non-stoichiometric amount) significantly changes the structural, electronic, magnetic and optical properties of conducting polymers [16]. The conductivity of these polymers can be increased dramatically from the semiconducting range (10^{-10} - 10^{-5} S/cm) to that

in the metallic range ($1 - 10^4$ S/cm) by increasing the concentration of dopant. The doping process in conducting polymers is completely different from that of semiconductors because the dopants do not substitute the host atoms but remain in the interstitial positions between the chains. The dopants through a redox process can either oxidize to create a positive charge or reduce to create a negative charge on the chain. Conducting polymers can also undergo a non-redox doping – the protonic acid doping, where the number of electrons along the polymer backbone remain constant, but results in a redistribution of electronic energy levels.

Doping in conducting polymers may be achieved by two distinct processes – chemical and electrochemical doping. In chemical doping, the polymer is exposed to an oxidizing agent such as iodine vapors [17] or a reducing agent, viz., alkali metal vapors [18]. In electrochemical process, doping is achieved by applying oxidizing or reducing voltage to the neutral polymer in an electrochemical cell [19]. The most important feature of conducting polymers is that the doping process is reversible i.e., the polymer can be made neutral by a 'de-doping' process unlike that in case of semiconductors. The charge carriers introduced as a result of doping are stabilized by altering the conjugation over several monomers. The charge together with the distortion in the structure of the polymer constitutes a single charge carrier. Depending upon the structure of the polymer backbone, its degeneracy and level of doping, the carriers may be solitons, polarons and bipolarons which are nothing but charged defects [20]. The carriers can move along the polymer chain by rearrangement of double and single bonds in the conjugated system upon application of electric field. The different carriers have different spin orientations which can respond to an applied magnetic field [21]. The charge neutrality of the doped polymer chains is balanced by the dopant counterions. These counterions play a major role in the charge conduction mechanism. Figure 1.4 shows a schematic of the formation of different types of charge carriers in conducting polymers and the corresponding modifications in their band structure.

Formation of polarons and bipolarons in poly(p-phenylene) and solitons in *trans*-polyacetylene

Electronic band structure of conducting polymers (CPs) in the neutral and doped states

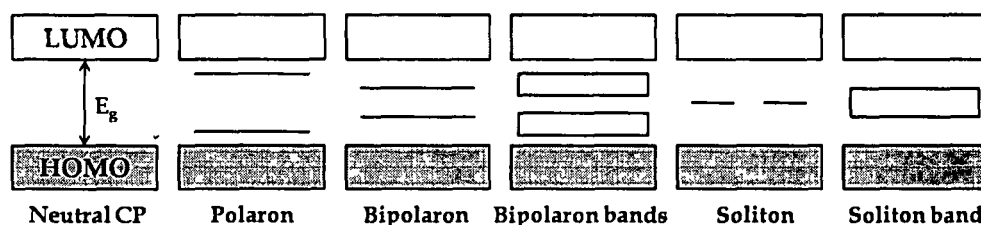


Figure 1.4: Molecular structures of conducting polymers illustrating the formation of charge carriers, viz., solitons, polarons and bipolarons. A schematic representation of the modifications in the band structure of conducting polymers as a result of the creation of charge carriers upon doping is also illustrated [25].

Removal of an electron via oxidation from a non-degenerate polymer [for example, poly(p-phenylene)] creates an unpaired electron with spin $\frac{1}{2}$ (free radical) and a spinless positive charge (cation). The radical and the cation are coupled to each other via a local bond deformation (rearrangement), creating a polaron which appears in the band structure as localized electronic state located symmetric to the band edges [21, 22]. The lower energy state is occupied by a single unpaired electron as depicted in Figure 1.4. On further oxidation, dications are created in the polymer. The second electron can be removed either from the polaron or from the remaining neutral portion of the polymer chain. In the former case, the free radical nature of the polaron is lost and a dication is created, which comprises of two positive charges coupled with lattice distortion. This dication together with the lattice distortion is termed as

bipolaron, which is a spinless defect [23, 24]. Removal of an additional electron from the neutral portion of the polymer chain would result in the formation of two polarons. However, the formation of a bipolaron is energetically favorable as it produces a larger decrease in ionization energy, as compared to that in the formation of two polarons. These new empty bipolaron states are also located in the band gap symmetric to the band edges. Additional localized bipolaron states are created with further doping, which eventually overlap to form continuous bipolaron bands at high enough doping levels (Figure 1.4). Thus the presence of these carriers creates new energy levels between HOMO and LUMO, hence narrowing the band gap in conducting polymers.

When *trans*-polyacetylene (*trans*-PA), a degenerate conducting polymer is oxidized, a polaron is formed (Figure 1.4). Further oxidation of PA leads to the formation of solitons. The ground state of *trans*-PA is two-fold degenerate i.e., the ground state has two equivalent ways of arranging the single and double bond alteration. Thus the bonding configurations on either side of the polaron differ only by a reversed orientation of the conjugated system and are energetically equivalent resonance forms. This in turn creates isolated, non-interacting charged defects that form domain walls separating two phases of opposite orientation but identical in energy. Such defects are called solitons, which results in the formation of new localized electronic states that appear midway in the energy gap. As the doping level increases, these states overlap to form soliton bands [26].

1.2 Charge transport in conducting polymers

1.2.1 Disorder in conducting polymers

Doping creates charge carriers which are delocalized along the polymer chain. These carriers can move upon the application of an electric field producing an electric current. However, the transport on a macroscopic length is quite complex and is controlled by a variety of phenomena. According to theoretical prediction, the π -electron system of a conjugated polymer makes it straight and

rigid. However, in reality, a polymer chain consists of a number of separated conjugated segments due to the presence of kinks, twists, or chemical defects which destroys the π -conjugation along the same chain. Conjugation length is defined as the mean length of the conjugated segments. As a result, the chains cannot be aligned throughout the whole length, and hence exhibit partial crystallinity [27]. The crystalline regions are interconnected by amorphous regions and the typical size of the crystalline regions varies in the range of 10 - 50 nm [28]. The different local arrangements and distribution of lengths of the conjugated segments modify their energy giving rise to locally varying polarizabilities and dipole interactions between the neighboring chains [29].

All these effects collectively tend to localize the charge carrier. Inhomogeneous distribution of the polymer chains, grain boundaries and morphology has also been found to affect the macroscopic transport. The factors which dictate the macroscopic transport are generally accounted for in the term 'disorder'. Disorder arises mainly due to simple and cheap processing methods commonly employed, inhomogeneous doping and partial crystallinity. Disorder can be energetic or structural (positional). As the local energy levels are determined by the local structure and the conjugation length, structural disorder often results in energetic disorder [30]. The energetic disorder is generally approximated by a Gaussian density-of-states (DOS), with the standard deviation of the Gaussian giving a characteristic energy width of $\sigma' \approx 0.1$ eV [30].

1.2.2 Role of disorder on charge transport

Due to π -electron delocalization along the chain, the conducting polymers were initially regarded as one-dimensional semiconductors. The dynamics of π -electrons along the one-dimensional chain were first studied by Su, Schrieffer and Heeger (SSH) [31]. The SSH model is a simple tight binding model developed for polyacetylene neglecting the Coulomb interactions and disorder effects. Although this model might be valid for single isolated chains or highly

ordered and stretch oriented polymer systems as supported by some experiments, the common conjugated polymer systems are highly disordered. It is therefore not possible to draw a one-dimensional semiconductor picture of these polymers.

Disorder inhibits the translational symmetry and causes the formation of localized states in the band gap [27]. Hence, the concept of band conduction by free carriers does not apply in these disordered polymers. For propagation of current, the carriers trapped in the localized states need to be released. The conduction involving localized states occurs by two processes: phonon-assisted hopping and direct tunneling. Tunneling occurs when the electronic wavefunctions of the two localized states adequately overlap, whereas the phonon-assisted hopping occurs when the charge carriers trapped in the localized states absorb a phonon and classically jump into the next available site. This usually leads to a very low carrier mobility typically in the range of 10^{-6} - 10^{-3} cm²/V.s. This mechanism of hopping was originally proposed by Mott [32] and Conwell [33] to explain the temperature dependence of dc conductivity in compensated semiconductors which was later applied to all disordered materials. The Mott's variable-range hopping (VRH) model is oversimplified as it ignores the electron-electron interactions or an energy dependent DOS. Various other models proposed to account for the observed conduction mechanism in disordered materials considering the electron-electron interaction effects [34], tunneling between conducting domains [35] and even superlocalization effects, where the electronic wavefunctions decay much faster than that in localized states [36, 37] are also applicable to conducting polymers. In fact, most of these models have severe limitations and are valid only in certain temperature regimes or systems.

Mott's hopping model i.e., VRH model is found to be valid in most of the conducting polymer systems. Hopping transport depends on the tunneling probability between two sites as well as on the probability of absorbing phonons that provide necessary energy for hopping [38]. Therefore, disorder in

position (structural disorder) and energy of hopping sites has a large influence on the mobility of the carriers and are thus crucial to hopping transport. Although, Mott's VRH model successfully explains the temperature dependence of dc conductivity, it fails to explain the field dependence of charge mobility which is more commonly known as the Poole-Frenkel (PF) mobility behavior [39]. The uncorrelated Gaussian disorder model (UGDM) [40] and the subsequent correlated Gaussian disorder model (CGDM) [41], which assumes a Gaussian DOS taking into consideration both the structural and energetic disorders, are the most used theoretical models to explain the observed PF mobility behavior.

1.2.3 Metal-insulator transition

The transport properties depend on various microscopic variables which may simultaneously be expressed in energy parameters, viz., electron-lattice interaction, electron-electron interaction (electron-hole interaction), bandwidth and the random disorder potential [42]. The relative strength of the bandwidth and the disorder potential gives rise to an interesting phenomenon in conducting polymers – the metal-insulator transition (MIT). If the disorder potential is large enough than the bandwidth potential, the states become localized. The system will then be a 'Fermi glass' insulator although there is no gap in the DOS [43]. However, this insulating behavior is due to the position of the Fermi level (E_F) in a region of localized states and the conductivity is zero at 0 K. When the disorder is sufficiently reduced, the localized and the extended states are separated by the mobility edge (E_c) and the MIT is defined by the position of E_F with respect to E_c i.e., the system becomes metal and insulator for E_F being situated in a region of extended states and localized states, respectively [44]. This transition is called the Anderson's disorder-induced MIT. A finite conductivity is expected when the Fermi level is at an energy such that the electronic states are extended.

Mott extended the Anderson transition for the case of interacting electrons which was a limitation in the case of Anderson's assumption of independent electrons. It enlightens a regime where the independent picture approximation, inherent to both Bloch and Anderson pictures, fails due to electron-electron interaction. According to Mott's consideration, a transition from extended to localized states occurs only when the correlation energy (on metallic side) exceeds a critical value compared to the bandwidth [45]. The main idea behind Mott's transition is that the correlation energy under particular conditions can force a solid to have an insulating ground state when the independent electron approximation picture wrongly classifies it as a metal [46]. However, in reality, MIT in disordered solids is neither a pure Anderson nor a pure Mott one. This type of complex phenomenon cannot occur from a single mechanism, but arises from a number of competing and complementary mechanisms involving a close interplay between two main mechanisms – electron-electron interaction and weak localization (disorder) [45]. The localization-interaction model [47] takes into account these two factors providing a framework to understand these effects in a better way.

1.3 Conducting polymer nanostructures

Nowadays, functionalized nanomaterials with the typical size in the range of 1 - 100 nm have been receiving immense attention due to their substantially improved properties and consequent enhanced performance in devices. Nanostructuring of conducting polymers has recently emerged as a new branch of nanotechnology directed to creation of new smart materials. Conducting polymer nanostructures are a special subclass which not only retain the unique characteristics of conducting polymers, such as π -conjugated polymeric chain, metal-like conductivity and reversible physical properties by a novel doping/de-doping process, but also possess the characteristics of nanomaterials i.e., large surface area, size- and quantum-effects. The nanoscale dimension of these polymers increases the merits in designing and developing efficient

devices and brings in the prospect of a range of enhancements which cannot be acquired by their bulk counterparts. Different nanostructures of conducting polymers such as nanofibers, nanowires, nanoparticles, nanotubes, nanosheets, nanoflowers and urchin-like structures have been synthesized using a number of techniques like micellar and reverse micellar polymerization, interfacial polymerization, rapid mixing polymerization, seeding polymerization, microemulsion polymerization, electro-spinning, and polymerization in the presence of soft- and hard-templates [48-55].

Of late, conducting polymer nanostructures have been successfully used as efficient sensors where the nanodimension offers large specific surface area and porosity increasing the response time of the sensor [56, 57]. These materials have also found applications in actuators [58, 59], as anticorrosion protective layers [60], field emission displays [61], memory devices [62] and flash welding [63].

1.4 Polyaniline (PANI)

Polyaniline (PANI), a heteroatomic non-degenerate conducting polymer is an extensively studied conducting polymer owing to its various favorable characteristics. The interest in this unique conducting polymer is rekindled due to its attractive doping and de-doping characteristics, environmental and thermal stability, and reasonably high electrical conductivity. These features are coupled with simple synthesis, inexpensive monomer and easily tunable morphologies (nanoparticles, nanofibers and nanotubes) that depend on the reaction conditions [64]. These are the key factors for choosing PANI as a material of study in the present thesis.

PANI is different from the family of π -conjugated polymers as it possesses some unique features. It can be regarded as an 'A-B' type copolymer with amine ($-\text{NH}-$) and imine ($=\text{N}-$) segments in the repeat unit [65]. Unlike other heteroatomic conducting polymers like polypyrrole (PPY) and polythiophene (PT), the heteroatom nitrogen occupies the primary sites in the

chain backbone. Therefore, it has asymmetric charge conjugation with benzene rings and nitrogen atoms in the conducting path [66]. The benzene rings either flip or rotate altering the electron-phonon interactions and consequently affect the charge transport. PANI exhibits three oxidation states ranging from fully oxidized to fully reduced forms. Figure 1.5 shows the different oxidation states of PANI which are: (a) leucoemeraldine base (LB)-fully reduced form, (b) emeraldine base (EB)-half oxidized and half reduced, and (c) pernigraniline base (PB)-fully oxidized form.

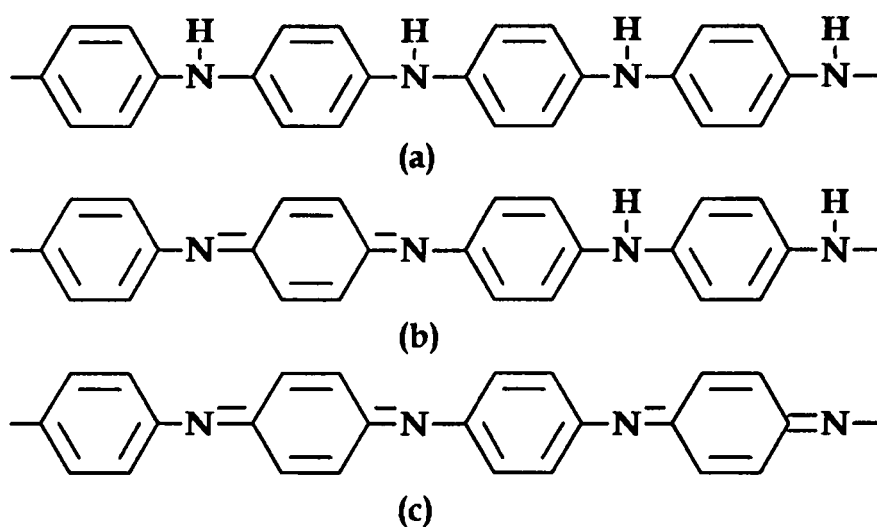


Figure 1.5: The different oxidation states of PANI, (a) leucoemeraldine base - fully reduced, (b) emeraldine base - half oxidized and half reduced, and (c) pernigraniline base - fully oxidized [45].

Although all the oxidation forms are insulating, the EB form can be made electrically conducting by doping with protonic acid of $\text{pH} < 3$. The protonic acid doping makes PANI unique among the conducting polymer family, since the transition from an insulator to a conductor is done without the addition or the removal of charge carriers, but only with a rearrangement of the electronic energy levels after protonation. Through protonic acid doping, the emeraldine base form of PANI is transformed to emeraldine salt (ES) form increasing the conductivity of the material by 9 - 10 orders of magnitude, which makes PANI ideal for the study of the insulator-metal transition [67]. Variations of the

doping level can induce considerable differences in the transport properties of the deduced PANI salts, providing us with a variety of systems on both sides of MIT for investigation. Protonation (or proton doping) can be achieved directly during synthesis or by exposing the already formed polymer to either gas or solution or even powdered acids. Maximum doping is achieved when half of the nitrogen sites on the chain are protonated. Proton doping is a non-redox doping which is significantly different from redox doping that involves partial addition (reduction) or removal (oxidation) of electrons to or from the polymer backbone [68]. The EB form of PANI can be recovered by treating the ES form by aqueous alkali causing de-protonation (de-doping).

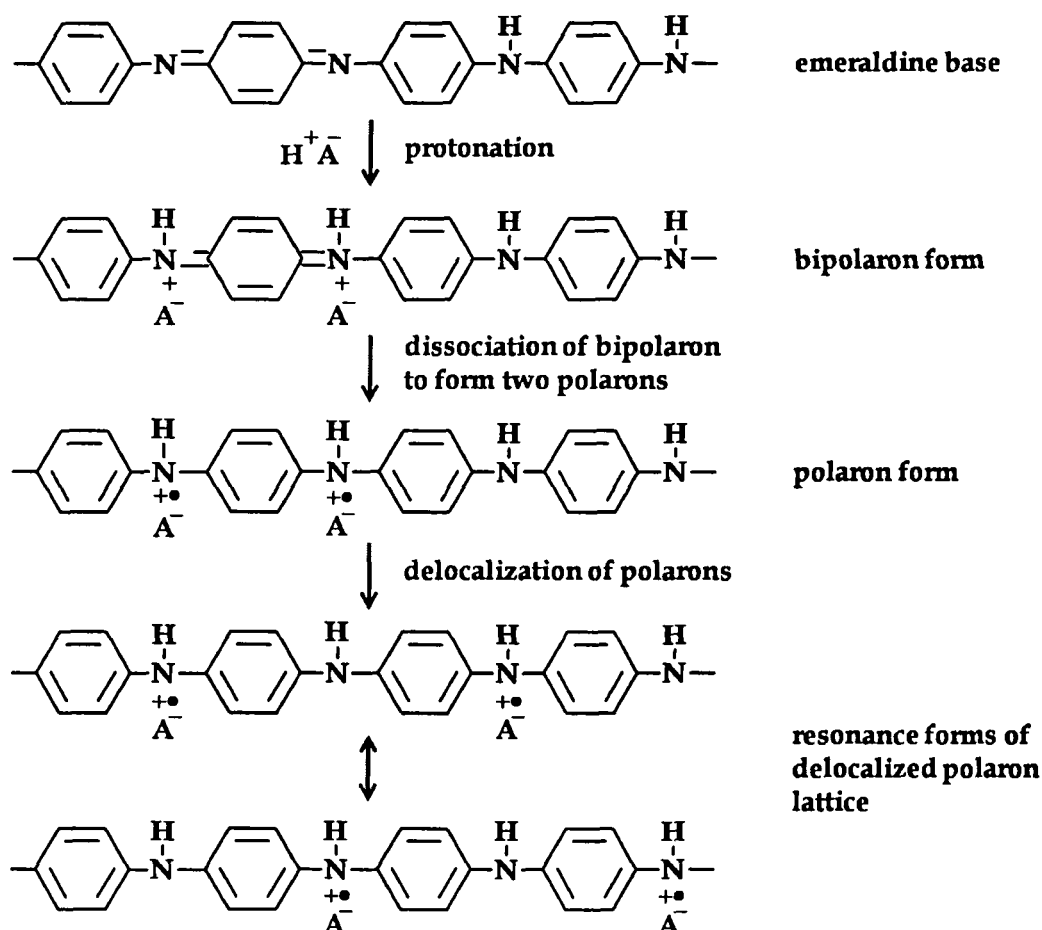


Figure 1.6: Schematic representation of doping in PANI. The EB form of PANI is doped with protonic acid to form the conducting state [67].

The EB form of PANI consists of amine ($-NH-$) and imine ($=N-$) sites in equal proportions. Protonation occurs at the imine nitrogen sites ($=N-$) in preference [69] which gives the bipolaron (dication) form. Figure 1.6 shows the protonation of EB form of PANI. Thus complete doping would mean the formation of a bipolaron (dication salt) lattice i.e., one bipolaron per repeat unit contained in the quinoid structure. This bipolaron is unstable and undergoes dissociation and proportionation to form two polarons which is a polysemiquinone radical cation. Although theoretical studies have predicted that a bipolaron lattice is energetically favorable over a polaron lattice [70], it is widely accepted that polarons are the charge carriers and that they are responsible for high conductivity in PANI [71, 72]. It has been proposed that the Coulombic interactions and dielectric screening together with the local disorder act to stabilize the delocalized polaron lattice in PANI [73]. However, it is also accepted that bipolarons do exist in PANI but are small in number and are not associated with the conducting regions [73].

1.5 Scope of the thesis and statement of the thesis problem

As the nature of transport in conducting polymers is determined by a variety of factors such as inter-chain interaction, electron-phonon interaction, Coulomb interaction, screening, lattice stiffness, extent of disorder and extent of conjugation length; theoretical modeling becomes even more complicated. The application of conducting polymers in various solid state devices such as solar cells [74], field-effect transistors [75], organic light emitting diodes [76], Schottky junctions [77], electromagnetic interference shielding [78], electrodes for redox supercapacitors [79], sensors [80] and molecular electronics [2], have also led the scientific community to investigate the transport mechanisms in much detail. The revelation of the nature of charge carrier and transport processes in conducting polymers is a widely open research problem both from the fundamental and application viewpoint. Many familiar concepts related to

conventional conductors such as the MIT in disordered materials, hopping and/or tunneling conduction, appear to be applicable for these polymers [81]. However, no single unanimous model is so far available that can completely describe the prevailing conduction processes occurring through the presence of non-linear excitations like solitons, polarons and bipolarons formed as a result of doping. The reason is that these polymers have one-dimensional polymer chains which make the conduction highly anisotropic, and the maximum attainable conductivities are limited by the small size of the crystalline regions over which the chains are aligned [82].

In recent times, conducting polymer nanostructures have attracted increasing attention because of their distinctive optical, electronic and mechanical properties, resulting in promising applications in electronic and optoelectronic nanodevices [83-85]. Although, the last decade has witnessed fascinating developments in the field of conducting polymer nanostructures, both in terms of basic science and technological standpoint [86-89], the transport mechanism in these nanostructures still remains poorly understood. A thorough understanding of the charge transport mechanism of the conducting polymer nanostructures is very much important for successful fabrication of sophisticated nanodevices. It is well recognized that nanostructures of conducting material dictate their physical properties. When a large proportion of the constituent atoms are present on the surface of a nanoparticle, then unique electronic and optical properties result. It is known that conducting polymers contain nanodomain components of much higher conductivity than that of the bulk [90], suggesting that nanodimensional control of structures will improve the conductivity of these polymers [91]. As the synthesis of these nanostructures is controlled at the nanoscale, the level of order is improved in the conducting polymer nanostructures [92]. More recently, it has also become apparent that both disorder and nanocrystalline structures are critical to the charge transport properties of conducting polymers [93-95]. Besides charge transport, thermal or heat transport is also an important

property of conducting polymers which has not been explored so far. Thermal transport of conducting polymers is very much important both from the fundamental and application point of view. It gives information regarding thermal management for use of these materials as efficient devices. The nature and mechanism of heat transport in conducting polymers even in the bulk form has not been studied in detail, with only a few reports on the experimental determination of thermal conductivity of polyacetylene [96], polypyrrole [97] and polyaniline [98].

Considering the above mentioned facts, we consider polyaniline (PANI) among the family of conducting polymers as the material of interest in the present thesis as it has many versatile properties (discussed in section 1.4), which makes it one of the most promising candidates for research as well as for application purposes. Moreover, stable nanostructures of PANI, namely, nanoparticles, nanofibers and nanotubes can be synthesized using the chemical oxidative polymerization method. The prime objectives of the present thesis are the study of electrical and thermal transport along with the magnetic measurements of different nanostructures of PANI varying the level of doping, dopant type and temperature, with a view to gain deeper understanding into the mechanism and nature of carriers involved in charge and heat transfer in these PANI nanostructures. In order to achieve the objectives, the following methodology was employed:

1. Different PANI nanostructures, viz., nanofibers, nanoparticles and nanotubes have been synthesized by interfacial polymerization and self-assembly methods.
2. High resolution transmission electron microscopy studies have been carried out to study the morphology, shape and size of the nanostructures.
3. X-ray diffraction studies have been conducted to investigate the structure and degree of crystallinity.

4. Fourier transform infrared spectroscopy and Raman spectroscopy have been recorded to investigate the conformational variations, chemical interactions and vibrational assignments.
5. Electrical transport measurements, viz., dc conductivity, magnetoresistance and current-voltage characteristics have been performed to understand the charge conduction mechanism.
6. Magnetic property measurements, viz., magnetic susceptibility and field dependence of magnetization have been done to understand the magnetic behavior of the charge carrying species.
7. Thermal transport property i.e., thermal conductivity measurements and thermodynamic property i.e., specific heat measurements have been made to understand the nature of heat carrying modes and heat transfer mechanism.

CHAPTER 2

Theoretical Aspects

This chapter deals with the various theoretical models and mechanisms invoked to elucidate the charge conduction in disordered organic semiconductors. The theories and mechanisms employed to explain the different experimental results involved in the present thesis have also been discussed. A brief discussion on different models proposed to explicate the heat transport in amorphous metallic glasses has been included.

2.1 Charge conduction mechanism in disordered organic semiconductors

A crystal has a three-dimensional translational symmetry which is constituted by infinite repetition of identical structural units. The structure of a crystal is described as a lattice which is characterized by long-range order and strongly coupled atoms [100]. For inorganic semiconductors such as silicon or germanium, the strong coupling between the atoms leads to the formation of long-range delocalized energy bands which is separated by a forbidden energy gap [100]. Charge carriers in the semiconductor can move in these energy bands with a relatively large mean-free path, and their transport is explained by the band theory of solids. In contrast, conducting polymers lack a well-ordered structural configuration as in inorganic crystals. The conjugation of the polymer backbone is disturbed by the presence of chemical or structural defects, such as chain kinks or twists. Over the past decades, intensive research has been carried out by the scientific community to explain the transport of charge carriers in

these materials; the charge transport of which is strongly influenced by disorder. Several transport models have also been proposed which show good agreement with the electrical measurements for several systems; however no complete explanation has been attained due to the diversity and complexity of these systems [101]. The following subsections include a concise discussion on several models proposed to explain the different electrical characterizations, namely, temperature dependence of conductivity, current-voltage characteristics and magnetoresistance, which have been carried out in the present study to understand the nature of charge transport in these polymers.

2.1.1 Temperature dependence of conductivity

Conducting polymers do not exactly behave as metals, although they are regarded as synthetic metals. The conductivity generally decreases as the temperature is decreased, despite the relatively high conductivity at room temperature. However, there are exceptions when these materials undergo a transition from metallic to insulating behavior. The temperature dependence of conductivity provides valuable information regarding the microscopic charge transport, since direct measurement at the molecular level is not possible. Various models put forward to explain the conductivity behavior of disordered solids usually accounts for the charge transport in conducting polymers. In the following sections, the primary features of some of the theoretical models have been highlighted.

2.1.1.1 Hopping models

For a variety of disordered semiconductors including conducting polymers, the temperature dependence of conductivity is best described by the Mott's variable-range hopping model (VRH) [38]. Disorder results in the formation of localized electronic states in the band gap and conduction occurs by hopping i.e., phonon-assisted tunneling between localized states randomly located within the energy gap. The Mott hopping transport occurs in a constant

density-of-states (DOS), where he proposes that the hopping over long distances and hopping to high energies are equally important. The term ‘variable-range’ refers to the change in the average hopping distance of the moving electron with temperature. As the temperature decreases, the thermal energy $k_B T$ decreases which in turn decreases the number of nearby states with accessible energies, and the electron hops to long range hopping sites. This increases the mean range of hopping. With increasing temperature, $k_B T$ increases and hence the hopping range decreases. Figure 2.1 represents the schematic of VRH process in the low temperature regime.

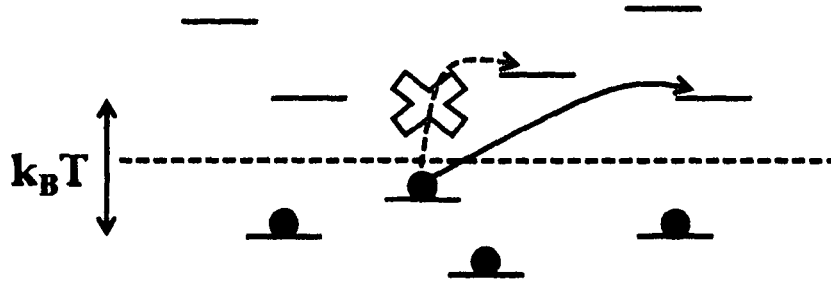


Figure 2.1: Schematic illustration of variable-range hopping behavior in the low temperature regime [102].

Let us consider two localized states with an energy separation ΔE at a distance r apart. An electron can hop from one site to the other by the absorption of a phonon of energy ΔE . The hopping probability depends upon two factors: (i) the tunneling decay factor $\exp(-r/L_c)$, here r signifies the distance between two hopping sites and will be denoted as R_{hop} in the later chapters, and L_c is the localization length, and (ii) the Boltzmann factor $\exp(-\Delta E/k_B T)$, k_B is the Boltzmann constant. The overall conductivity is determined by optimizing the competition between $\exp(-r/L_c)$ and $\exp(-\Delta E/k_B T)$, which can be written as:

$$\sigma(T) = \sigma_0 \exp \left[- \left(\frac{T_0}{T} \right)^n \right] \quad (2.1)$$

$n = 1/4, 1/3$ and $1/2$ for three-, two- and one-dimensional hopping of the electrons. The constant T_0 is given approximately by $k_B T_0 = 16/[N(E_F)L_c^3]$, where $N(E_F)$ is the density of localized states at the Fermi level.

However, in the VRH model proposed by Mott, the effect of electron-electron interactions was not considered. Efros and Shklovskii pointed out that the Coulomb interaction between localized electrons creates a soft gap known as the 'Coulomb gap' in the DOS near the vicinity of the Fermi level [103]. This assumption leads to a situation where the conductivity is found to be proportional to $T^{-1/2}$ regardless of the dimensionality of the hopping process. The expression for conductivity is given as follows:

$$\sigma(T) \propto \exp\left[-\left(\frac{T_{ES}}{T}\right)^{1/2}\right] \quad (2.2)$$

where T_{ES} is the characteristic Efros–Shklovskii temperature.

Deutscher and his co-workers [104] presented a new mechanism where the parameter n equals to $3/7$ for a VRH among superlocalized states without Coulomb interactions in fractal structures. The wavefunctions in a fractal structure varies with distance r as $\psi(r) \propto \exp\left[-(r/L_c)^\xi\right]$ [36], where $\xi > 1$, is the superlocalization exponent which is unity in case of Anderson (disorder-induced) localization. The conductivity relation for charge transport by VRH among superlocalized states is given as [104]:

$$\sigma(T) \approx \exp\left[-\left(\frac{T_0}{T}\right)^{\frac{\xi}{d_f+\xi}}\right] \quad (2.3)$$

where $n = \xi/(\xi+d_f) \approx 3/7$ and d_f is the fractal dimensionality.

Later on, Van der Putten et al. [37] generalized the VRH theory among superlocalized states including Coulomb interaction and obtained a value of $n = \xi/(\xi+1) \approx 0.66$.

2.1.1.2 Tunneling models

As opposed to hopping models where the charge carriers hop between the localized states, the tunneling model proposed by Sheng and Klafter [105] and Sheng [35] assume that electrical conduction is mediated by tunneling between conducting regions. In general, disordered materials are characterized by large conducting regions (or long conducting pathways) which are separated by narrow insulating barriers. This model considers charging of some of these conducting regions that occurs through random thermal motion of charge carriers from neighboring neutral regimes. However, this process requires an energy which depends both on the separation and size of the conducting regimes (inversely proportional to size of the conducting regimes), as well as on the applied voltage. When the size of the conducting regions, for example, is very small like 20 nm or less, a considerable amount of energy is required to remove an electron from an electrically neutral island. If the voltage between adjacent metallic islands is small, the carriers are generated by thermal activation causing the temperature dependence of conductivity. The expression of conductivity is given by:

$$\sigma(T) = \sigma_0 \exp \left[- \left(\frac{T_0}{T} \right)^{1/2} \right] \quad (2.4)$$

where T_0 and σ_0 are material constants. Eq. (2.4) is similar to that of one-dimensional VRH.

When the applied voltage is high i.e., when the voltage drop between neighboring grains is much larger than $k_B T/e$, charge carriers are mostly generated by field-induced tunneling between neutral regimes. In this case, the conductivity varies exponentially with field as:

$$\sigma = \sigma_0 \exp \left[- \left(\frac{F_0}{F} \right) \right] \quad (2.5)$$

where F_0 is a material constant related to the size of the conducting metallic islands and F is the applied field.

On the other hand, when the size of the metallic islands is about $1 \mu\text{m}$ or more, conduction happens through fluctuation-induced tunneling between conducting islands. The random thermal motion of the charge carriers within the conducting islands induces a randomly alternating voltage across the gap between the neighboring islands. The temperature dependent conductivity is given as:

$$\sigma(T) = \sigma_t \exp\left[-\frac{T_t}{T + T_s}\right] \quad (2.6)$$

where the parameter T_t represents the temperature at which the thermal voltage fluctuations become large enough to raise the energy of electronic states to the top of the barrier, and the ratio T_t/T_s determines the tunneling in the absence of fluctuations.

2.1.1.3 Heterogeneous model

Polymers exhibit only partial crystallinity with the polymer chains aligned only in some crystalline regions of typical dimension $10 - 50 \text{ nm}$ [28, 106]. These small crystalline regions are termed as crystallites. Some polymer chains may extend through a number of crystallites or may fold back on themselves within the crystallites. In both the cases, the ordered crystallites are interconnected by disordered amorphous regions. This heterogeneous nature of the polymer chains plays a significant role in conduction. When the conductivity of the ordered crystalline regions is high, the total resistance is dominated by the disordered regions, through which the current must pass [83]. For a fibrillar polymer, the expression for resistivity in a heterogeneous model with high and low conductivity sections in series is given by Kaiser [107] as:

$$\sigma(T)^{-1} = \rho(T) = \sum_i f_i \rho_i(T) \quad (2.7)$$

where f_i are geometric factors defined as $f_i = \frac{L_i A_i}{LA}$. Here L and A signifies the effective total length and cross-sectional area of the sample, L_i is the length of the path consisting of material i with intrinsic resistivity ρ_i and A_i is the effective cross-sectional area for conduction in each type of material. For a fibrillar polymer where the fibers have similar properties and the nature of the electronic states does not change with temperature, the temperature dependence of the geometric factors will be small [107].

For non-fibrillar polymers, a more complex series heterogeneous model is proposed where the effect of separating thin barriers is taken into account. When the metallic regions are extended, separated by thin barriers, the overall conductivity is given by a combination of quasi one-dimensional metallic conduction and fluctuation-induced tunneling [108]:

$$\sigma(T)^{-1} = \rho(T) = f_1 \rho_m \exp\left(-\frac{T_m}{T}\right) + f_2 \rho_t \exp\left(\frac{T_t}{T + T_s}\right) \quad (2.8)$$

As the tunneling conductivity increases with temperature and the metallic conductivity decreases, Eq. (2.8) gives rise to a peak in the conductivity at a crossover temperature, when the temperature coefficient of conductivity changes sign from non-metallic to metallic.

For smaller metallic regions, the fluctuation-induced tunneling is replaced by the expression for tunneling between mesoscopic islands limited by their charging energies [109]:

$$\sigma(T)^{-1} = \rho(T) = f_1 \rho_m \exp\left(-\frac{T_m}{T}\right) + f_2 \rho_0 \exp\left[\left(\frac{T_0}{T}\right)^{1/2}\right] \quad (2.9)$$

Eq. (2.9) is also applicable when the conduction through the barrier is by quasi one-dimensional VRH [108].

2.1.1.4 Metal-insulator transition and localization-interaction model

High degree of structural disorder prevented the conducting polymers of first generation to exhibit metallic features. Considerable progress achieved in recent years in synthesis and improvement of the structure, reduced the degree of disorder making it possible to identify and study the mechanisms of charge carrier transport in doped conducting polymers, including those on the metal side of the metal-insulator transition (MIT) [110, 111]. The degree of disorder significantly affects the conductivity $\sigma(T)$ at low temperatures [47, 112].

Ioffe and Regel [113] argued that in a disordered metallic system, the metallic behavior is limited by the extent of disorder present. When the mean-free path becomes less than the inter-atomic spacing, coherent metallic transport is not possible. The Ioffe-Regel criterion is defined as $k_F l_m \sim 1$, where k_F is the Fermi wave vector and l_m is the mean-free path. The metallic regime corresponds to $k_F l_m \gg 1$. Considering the Ioffe-Regel criterion, Mott [38, 112] anticipated that a MIT must occur when the disorder is sufficiently large such that $k_F l < 1$. This MIT is called the 'Anderson's transition' (disorder-induced transition) [43]. In the limit when $k_F l \ll 1$ i.e., when the strength of the random disorder potential is large compared to the bandwidth, all the electronic states become localized and the conductor becomes a 'Fermi glass' [114]. Although there is no gap in a Fermi glass, it still behaves as an insulator because the states at the Fermi level are spatially localized.

According to Mott, the states in the band tails are more susceptible to localization and hence there exists a critical energy separating the localized from the delocalized states which is called the mobility edge (E_c) [38, 112]. A transition from a metal to a Fermi glass insulator occurs when the Fermi energy falls in the region of localized states. The scaling theory of localization established that the disorder-induced MIT is a true phase transition with a well defined critical point [115]. MacMillan [116], and later Larkin and Khmel'nitskii

[117] showed that near the critical regime of Anderson localization, a power-law temperature dependence of conductivity is expected.

The metallic and insulating regimes can be discriminated only by the zero temperature limit of conductivity (σ) [118]. The basic property of the metallic behavior is the existence of a finite conductivity when $T \rightarrow 0$ K. This indicates the presence of delocalized states at the Fermi level. On the other hand, if $\sigma \rightarrow 0$ as $T \rightarrow 0$ K, the sample is an insulator. This simple definition cannot be put to practical use for the determination of metallic and insulating samples, since absolute zero is not attainable. Besides, the positive temperature coefficient of resistivity (TCR) shown by metals is also difficult to observe in a disordered metal, although a positive TCR over a specific temperature range can be considered as an indication of metallic transport. However, detailed studies of disordered metals have shown that systems with weak negative TCR can also be metallic [119]. Zabrodskii and Zeninova [120] have shown that the temperature dependence of conductivity is better understood by using the reduced activation energy (W) which is defined as:

$$W = \frac{d(\ln\sigma)}{d(\ln T)} = \frac{T}{\sigma} \frac{d\sigma}{dT} \quad (2.10)$$

According to Eq. (2.10), $W(T)$ vanishes as $T \rightarrow 0$ for a metallic sample. The reduced activation energy W is more sensitive than conductivity [121]; hence it is used to analyze the temperature dependence of conductivity showing a weak negative TCR. The characteristic transport regimes near a MIT can be identified by different temperature dependences of $W(T)$ in the following way [119]:

1. If $W(T)$ has a positive temperature coefficient at low temperatures, then the system is on the metallic side of the MIT.
2. If $W(T)$ is temperature independent for a wide range of temperatures, then the system is on the critical regime of the MIT.
3. If $W(T)$ has a negative temperature coefficient at low temperatures, the system is on the insulating side of the MIT.

In the insulating regime, the conductivity is well described by the Mott's VRH model as given by the Eq. (2.1). The conductivity in the critical regime follows a power-law dependence of the form [116, 117]:

$$\sigma(T) = \left(\frac{h^2}{4\pi^2 e^2 p_F} \right) \left(\frac{k_B T}{E_F} \right)^{1/\eta} = AT^\delta \quad (2.11)$$

where the predicted range of validity for δ is $0.3 < \delta < 1$. p_F is the Fermi momentum, h is Planck's constant, and e is the electronic charge. A value of $\delta \approx 1/3$ indicates that the system is just on the metallic side of MIT. It has to be emphasized that besides disorder-induced MIT, Coulomb correlation in an ordered system may also lead to similar metal-insulator transition [122]. The conductivity on the metallic side of MIT at low temperatures is thus described by the localization-interaction model, which is based on weak localization (disorder) and electron-electron interactions. The conductivity relationship is given as [47]:

$$\sigma(T) = \sigma(0) + mT^{1/2} + BT^{p/2} \quad (2.12)$$

where the second term is determined by the influence of the electron-electron interactions and the third term is determined by the corrections to zero temperature conductivity due to weak localization effects. The value of p is determined by the temperature dependence of the scattering rate, $\tau_m = T^{-p}$ of the dominant dephasing mechanism. For electron-phonon scattering, $p = 2.5-3$; for inelastic electron-electron scattering, $p = 2$ and 1.5 in the clean and dirty limits, respectively [123]. However, Belitz and Wysokinski [124] have shown that very near the MIT, electron-electron scattering also leads to $p = 1$. According to this model, the electron-electron interaction affects the transport at low temperatures, whereas the weak localization effects are dominant at higher temperatures.

2.1.2 Current-voltage characteristics

Some macroscopic models for current flow as a function of applied voltage are discussed in the following sections. In general, these models can be combined together to completely describe the measured current-voltage curve and to determine the material parameters.

2.1.2.1 Ohmic conduction

In organic semiconductors, Ohmic conduction is observed when the density of injected charges is lower than the density of thermally excited charges. In this case current density (J) varies linearly with applied voltage (V) and is described as:

$$J = \frac{e\mu n_c V}{d} \quad (2.13)$$

where e is the charge of the carrier, n_c is the density of carriers, μ is the mobility of carriers and d is the thickness of the sample.

2.1.2.2 Space-charge-limited conduction

When carriers injected through an Ohmic contact exceed the concentration of intrinsic carriers, the current is limited by space-charge. Space-charge means a region where there is a large concentration of charges in the form of electrons, holes or ions (the charges depend upon the material). These charges may be mobile or localized, but constitute a localized non-uniform electric field. The transport of charges under the influence of this non-uniform field is called space-charge-limited conduction (SCLC), and is widely observed in organic semiconductors. SCLC methods provide useful information regarding the charge carrier mobility, concentration and energy distribution of localized defects or charge trapping states [125].

The basic requirement to achieve SCLC regime is bulk-limited transport which is acquired by using an injecting Ohmic contact. When charge carriers

are injected by applying an electric field, the injected space-charge decreases the electric field at the injecting surface and gives rise to a space-charge-limited current.

Mott and Gurney [126, 127] proposed an approximate theory of SCLC in a trap-free solid. In this case, current varies as square of the applied voltage and is expressed as:

$$J = \frac{9}{8} \epsilon_0 \epsilon_r \mu \frac{V^2}{d^3} \quad (2.14)$$

where ϵ_0 is the permittivity of free space and ϵ_r is the relative permittivity.

This equation is known as the Mott-Gurney law which describes the nature of current in a trap-free material. This behavior can be observed either in trap-free materials, or when all available traps are filled with charges. This is also observed when the concentration of traps is less than the free carrier concentration [128, 129].

Trapping sites, especially in disordered organic semiconductors are expected to be distributed in energy starting from the HOMO or the LUMO level. These traps can arise from disorder, dangling bonds or impurities. Mark and Helfrich [125] studied the SCLC in the presence of exponentially distributed trap states. They assumed that the free carrier concentration is much less than the trapped carrier concentration, and that the traps are exponentially distributed in the band gap. If the trap energies are continuously distributed with an exponential function, the density of trap states as a function of the energy level (E) above the HOMO level (E_{HOMO}) can be expressed as:

$$N(E) = \frac{N_t}{lk_B T} \exp\left(-\frac{E}{lk_B T}\right) \quad (2.15)$$

The integration from $E = 0$ to ∞ then gives the total trap density N_t [130]. When $E = lk_B T$, the exponential term has the value $1/e$; therefore, $lk_B T$ is regarded as

the 'characteristic width' of the exponential distribution. This relation leads to the following power-law dependence of J on V ,

$$J = e^{l-1} \mu N_{HOMO} \left(\frac{2l+1}{l+1} \right)^{l+1} \left(\frac{l}{l+1} \frac{\epsilon \epsilon_0}{N_t} \right)^l \frac{V^{l+1}}{d^{2l+1}} \quad (2.16)$$

where l is an energy parameter given by $l = T_c/T$, T_c is the characteristic temperature of traps, N_{HOMO} is the effective DOS of the HOMO level.

2.1.2.3 Poole-Frenkel mobility

Poole-Frenkel (PF) mobility was first predicted by Frenkel [131] to explain the increase in conductivity of insulators and semiconductors when high electric field is applied. It is defined as:

$$\mu = \mu_0 \exp(\gamma \sqrt{F}) \quad (2.17)$$

where μ_0 is the zero-field mobility, γ is the field activation parameter and F is the applied electric field. μ_0 and γ depend on the considered system. In conventional semiconductors, charges trapped at a charged defect can be detrapped by applying an electric field, which lowers the barrier for the carrier to thermally escape the Coulombic potential. This gives rise to a PF field dependence of mobility. The physical effect of an electric field is then to effectively reduce the hopping barrier. Assuming a Coulomb potential for hopping barrier, the mobility will have an electric field dependence of the PF type as given in Eq. (2.17) with the zero-field mobility μ_0 given by [132]:

$$\mu_0 = \mu_i \exp\left(-\frac{E_b}{k_B T}\right) \quad (2.18)$$

where μ_i is the intrinsic mobility at zero hopping barrier and E_b is the zero-field hopping barrier, also known as low-field activation energy. Eq. (2.17) can be rewritten as:

$$\mu = \mu_i \exp\left(\frac{\gamma\sqrt{F} - E_b}{k_B T}\right) \quad (2.19)$$

Eq. (2.19) has been modified by Gill [39] to increase agreement with experimental data by substituting T with an effective temperature T_{eff} , such that

$$\frac{1}{T_{eff}} = \frac{1}{T} - \frac{1}{T_0} \quad (2.20)$$

where T_0 is the characteristic temperature of the material.

The empirical form of charge carrier mobility then becomes:

$$\mu = \mu_i \exp\left(-\frac{E_b}{k_B T}\right) \exp\left[\frac{\gamma}{k_B} \left(\frac{1}{T} - \frac{1}{T_0}\right) \sqrt{F}\right] \quad (2.21)$$

2.1.2.4 Gaussian disorder model

A semiconducting polymer is not a perfect conjugated system. The twisted and kinked chains, and chemical defects in a semiconducting polymer chain cause conjugation breaks. The variation in the conjugation length and interaction energies causes the semiconductor to have an energetic spread of charge transport sites approximated by a Gaussian DOS, instead of having two delocalized energy bands separated by an energy gap. Therefore, the charge carriers are transported via hopping between sites with randomly varying energy levels and inter-site distances as depicted in Figure 2.2.

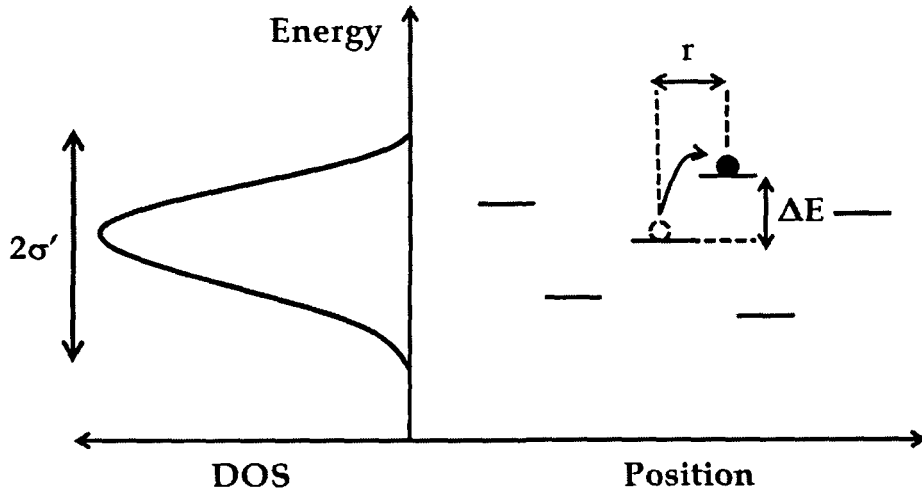


Figure 2.2: Charge hopping process between localized states in a Gaussian DOS of width σ' . A charge hops between two localized sites with an energy difference ΔE separated by a distance r [133].

Bässler and co-workers [40, 134] proposed a charge transport model for disordered organic semiconductors to explain the field and temperature dependence of mobility of carriers. They assumed a Gaussian DOS with a width σ' . In this model, the carrier transport is described as a biased random walk among the hopping sites with Gaussian-distributed random site-energies. In this way, both positional disorder (fluctuation in inter-site distance) and energetic disorder (fluctuation in site-energy) are introduced. Based on this assumption and performing Monte-Carlo simulations, they were able to reproduce Eq. (2.21) for temperatures around room temperature, but only for a very narrow field range, and at relatively high electric fields ($> 10^6$ V/cm) as compared to the experimental regime. The temperature and field dependence of mobility according to the Gaussian disorder model (GDM) is given as:

$$\mu_{UGDM} = \mu_{\infty} \exp \left[- \left(\frac{2\sigma'}{3k_B T} \right)^2 + C' \left\{ \left(\frac{\sigma'}{k_B T} \right)^2 - \Sigma^2 \right\} \sqrt{F} \right] \text{ for } \Sigma \geq 1.5 \quad (2.22)$$

$$= \mu_{\infty} \exp \left[- \left(\frac{2\sigma'}{3k_B T} \right)^2 + C' \left\{ \left(\frac{\sigma'}{k_B T} \right)^2 - 2.5 \right\} \sqrt{F} \right] \text{ for } \Sigma \leq 1.5 \quad (2.23)$$

where μ_{∞} is the mobility in the limit $T \rightarrow \infty$, C' is a constant that depends on the site spacing and Σ is the degree of positional disorder. A consequence of hopping in a Gaussian DOS is the non-Arrhenius behavior of the mobility in contrast to that observed in Eqs. (2.19) and (2.21). The Gaussian disorder model is also known as the uncorrelated Gaussian disorder model (UGDM) as it does not take into account the correlation between site-energies as discussed below.

To improve the validity regime of the field dependence of mobility, Gartstein and Conwell [135] took into account spatial correlations between the energies of neighboring sites, which successfully extended the PF behavior to lower electric fields in accordance with the experimentally observed results. A spatially correlated site-energy means that the energies are correlated over a greater length than the distance between hopping sites. Due to the correlation of energies of adjacent sites, the field dependence of the mobility extends to lower electric fields. The spatial correlations in site-energy arise from the long-range charge-dipole interactions in the material, where the disorder is determined by the random orientations of dipole moments of nearby molecules. According to this correlated Gaussian disorder model (CGDM), the empirical expression for mobility is given by [41, 136]:

$$\mu_{CGDM} = \mu_{\infty} \exp \left[- \left(\frac{3\sigma'}{5k_B T} \right)^2 + C_0 \left\{ \left(\frac{\sigma'}{k_B T} \right)^{3/2} - \Gamma \right\} \sqrt{\frac{eFa}{\sigma'}} \right] \quad (2.24)$$

where $C_0=0.78$, a is the inter-site separation and $\Gamma=2$ for organic materials. The main difference between CGDM and UGDM is the predicted temperature dependence of field activation parameter γ .

2.1.3 Magnetoresistance

Conducting polymers generally exhibit a transition from positive to negative magnetoresistance (*MR*) with increase in temperature, and is explained using different theories [137, 138] which are discussed in the following sections. The bipolaron model used to explain the observed *MR* behavior in the present study is also elaborated.

2.1.3.1 Positive magnetoresistance

A positive *MR* is generally expected for strongly localized carriers exhibiting VRH under the application of a magnetic field. When a magnetic field is applied, there is shrinkage in the overlap of the localized state wavefunctions leading to a decrease in the tunneling probability and a corresponding increase of the average hopping length [34, 38, 139]. This leads to a large positive *MR* at sufficiently low temperatures. The VRH resistivity is strongly dependent on temperature and magnetic field. The weak-field *MR* can be expressed as [34, 139]:

$$\ln(\rho(H)/\rho(0)) = t_1 \cdot (L_c/L_H)^4 \cdot (T_0/T)^y \propto H^2 \cdot T^{-y} \quad (2.25)$$

where t_1 is a constant, $L_H = (\hbar/eH)^{1/2}$ is the magnetic length, L_c is the localization length, $\hbar (= h/2\pi)$ is the Planck's constant. For three-dimensional Mott VRH, $t = 5/2016$ and $y = 3/4$; for one-dimensional VRH, $t = 0.0015$ and $y = 3/2$. In case of strong magnetic field, there is a deviation from H^2 dependence with lowering temperature. According to VRH theory, the high-field *MR* can be written as [34, 139]:

$$\ln(\rho(H)/\rho(0)) = t_2 \cdot (L_c/L_H)^{2/3} \cdot (T_0/T)^{1/3} \propto H^{1/3} \cdot T^{-1/3} \quad (2.26)$$

where t_2 is a constant. When the applied field is sufficiently high, a transition from the H^2 dependence to $H^{1/3}$ dependence of $\ln(\rho(H)/\rho(0))$ occurs at the characteristic field H_c , which decreases with lowering temperature.

2.1.3.2 Negative magnetoresistance

The negative MR in the hopping regime is caused by the dephasing effect of magnetic field on the quantum interference of many possible hopping paths. The orbital magnetoresistance in the VRH regime was studied by Nyugen et al. [140, 141] and Sivan et al. [142]. Nyugen et al. considered the effect of magnetic field on the hopping probability between two sites separated by a distance r (r is the hopping length), where the hopping probability is determined by the interference of many possible paths connecting the two sites. On averaging the logarithm of conductivity over many random impurity realizations in a macroscopic sample, they obtained a net decrease in resistivity with field i.e., negative MR [143-145]. On the other hand, Sivan et al. applied critical path analysis and obtained the same results but the field dependence of MR was found to be quadratic at small fields. The field dependence of resistivity in both the models is determined by the flux threading an area over which phase coherence is maintained, and the area of such a coherent loop is that of an ellipse of length r and area $(ra_m)^{1/2}$ (a_m is microscopic length). The MR is expected to approach a constant negative value at high magnetic fields when the flux ϕ_M threading a coherent loop becomes comparable to or greater than one quantum flux ϕ_0 . According to Sivan et al. [142, 146], at small magnetic fields (such that $\phi_M \ll \phi_0$), the MR is proportional to the square of the flux threading the loop. A common form of equation combining both the models can be written as:

$$MR = (\rho(H) - \rho(0)) / \rho(0) \propto -H^x \cdot T^{-y} \quad (2.27)$$

where $x = 1$ [140] or 2 [142] and $y = 3/4$ for three-dimensional VRH and $y = 3/2$ for one-dimensional VRH.

2.1.3.3 Bipolaron model

Bipolaron model [147, 148] was proposed to explain the organic magnetoresistance (OMAR) in disordered organic semiconductors. OMAR is a large low-field symmetric magnetoresistance (MR) present in completely non-magnetic organic devices at room temperature. This model considers that bipolarons are formed out of two polarons as an intermediate state in the charge transport process. The charge transport in organic semiconductors takes place via a limited number of percolation paths [149]. On such paths, some low energy sites with quasi-trapped charges in form of polarons might block the passage of other charges. As the common mode of charge conduction in conducting polymers occurs through a hopping of polarons, therefore when these mobile polarons jump on the sites already occupied by other polarons, they form an intermediate bipolaron, before it can move further through the materials. However, intermediate bipolaron state cannot be formed if the spin configuration of polarons are parallel i.e., a triplet configuration; hence the charge cannot pass the site. This phenomenon is called 'spin blocking' and causes a decrease in the mobility resulting in a decrease in current.

Figure 2.3 illustrates the formation of bipolaron and spin blocking. Hyperfine field induced spin mixing [Figure 2.3(c)] eliminates spin blocking by changing the initial triplet configuration of polaron pairs into singlet configuration and thereby, allowing a larger current to pass. On the application of a large external magnetic field, the spins will precess around the sum of the external field and the local hyperfine field [Figure 2.3(d)]. The hyperfine field being almost negligible, the spins experience approximately the same field. As a result, two parallel spins will remain parallel and no mixing occurs. Applying an external magnetic field thus favors spin blocking resulting in a positive MR . A negative MR can also result when the long-range Coulomb repulsion is taken into account. The long-range Coulomb repulsion is expected to enhance the bipolaron formation [147]. When more bipolarons are formed, there are less free

carriers to carry current. By applying an external magnetic field, the number of bipolarons is decreased which gives a negative MR.

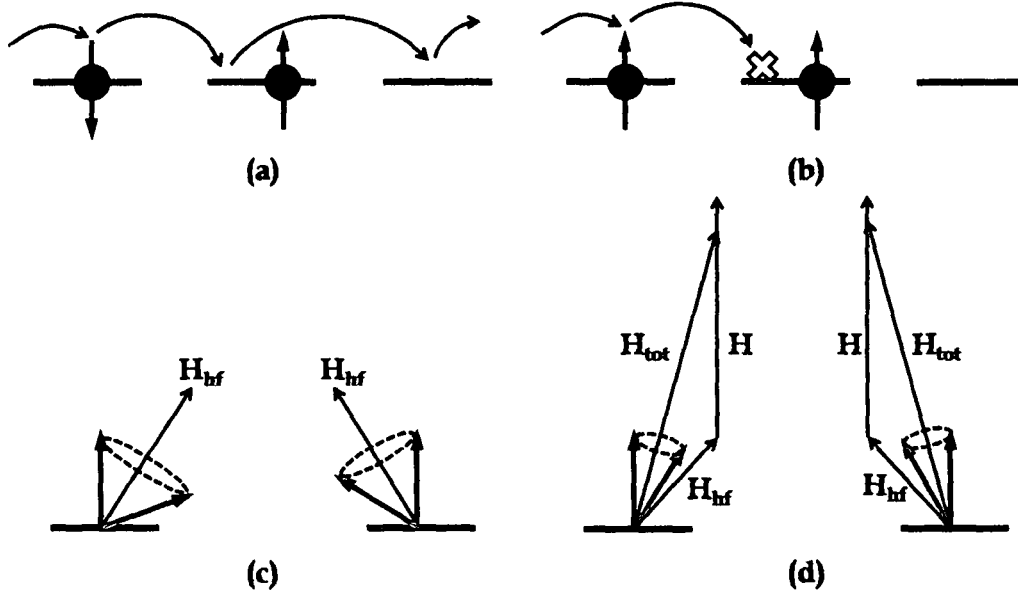


Figure 2.3: Schematic illustration of (a) bipolaron formation when the polarons are in singlet configuration, (b) spin blocking when the polarons are in triplet configuration, (c) hyperfine precession of the carriers and (d) precession of the carriers under total magnetic field H_{tot} , where H_{tot} is the sum of hyperfine field H_{hf} and applied external field H [150].

The bipolaron model has been investigated using a Monte Carlo approach [147], considering a large grid of lattice sites, and also an analytical approach [148], considering two sites and the environment. The Monte Carlo based simulation shows that bipolaron formation is best facilitated when $U \approx \sigma$, where U is the bipolaron formation energy and σ is the width of Gaussian DOS. OMAR exhibits two characteristic $MR(H)$ line shapes. A Lorentzian,

$$MR(H) = MR_{\infty} \frac{H^2}{H^2 + H_0^2} \quad (2.28)$$

and a more slowly saturating empirical non-Lorentzian,

$$MR(H) = MR_{\infty} \frac{H^2}{(|H| + H_0)^2} \quad (2.29)$$

where MR_{∞} is the MR value at $H = \infty$ and H_0 is the characteristic magnetic field width. H_0 is the half-width at half-maximum in the case of Lorentzian and the half-width at quarter-maximum in the case of non-Lorentzian line shape. The bipolaron model proposes that H_0 is dependent on the branching ratio b . This ratio is defined as $b = r_{\alpha \rightarrow \beta} / r_{\alpha \rightarrow e}$, where $r_{\alpha \rightarrow \beta}$ is the rate at which a carrier from a singly occupied site α hops into a neighboring singly occupied site β to form a bipolaron and $r_{\alpha \rightarrow e}$ is the rate at which a carrier from α bypasses β , by hopping over β into unoccupied sites in the environment. Both the Monte-Carlo simulations [147] and the analytical calculations of a two-site model [148] have shown that increasing b results in increasing H_0 . Therefore, the more a carrier is forced to hop into another occupied site and form a bipolaron, larger is the width of the MR feature. This can explain the temperature induced transition from positive to negative MR . At low temperatures, carriers have less energy to hop into sites further away in the environment and hence are more likely to form bipolarons. Therefore, the carriers have to hop into neighboring singly occupied sites creating bipolarons and resulting in the increase of both b and H_0 . The models predict that upon increasing temperature or decreasing b , the linewidth saturates below a certain value, and the empirical non-Lorentzian line shape converges into a Lorentzian one with a width of approximately equal to the hydrogen hyperfine field ($H_{hf} \approx 1$ mT [151]), the relevant field scale in the bipolaron model.

2.2 Heat transport mechanism in amorphous materials

The nature of heat transport in disordered organic semiconductors is not understood and hence no model has yet been proposed to elucidate the mechanism of heat transfer. In this thesis, the models proposed to explain the heat transport in amorphous materials have been borrowed for qualitative

description of the observed results. The following subsections include a brief discussion on the different theories proposed to explain the thermal conductivity of amorphous solids.

2.2.1 Thermal conductivity

The thermal conductivity κ of amorphous solids shows, in general, three regions of different behavior: (i) at very low temperatures (< 1 K), it behaves approximately as $\kappa \propto T^2$; (ii) for $T \approx 10$ K there is a plateau independent of temperature; and (iii) at higher temperatures κ increases often linearly with T and mostly reaches a saturated value.

The behavior at and below the plateau can be explained by the widely accepted soft-potential model [152]. However, the behavior of κ above the plateau in the high temperature regime is quite intriguing. Some widely differing scenarios have been proposed by different researchers to explain such monotonic increase in κ with T . A completely harmonic model was proposed that assumes heat transport by diffusive motion of delocalized, but non-propagating vibrational modes [153]. The model based on fracton hopping requires anharmonicity to make energy transport possible [154, 155]. In the fracton hopping model, it is considered that localized fracton states are anharmonically coupled to long-wavelength phonons and the dependence, $\kappa \propto T$ above the plateau is due to phonon-assisted fracton hopping. Böttger et al. [156] studied the heat transport in a simple model system of Anderson localized optical carrier phonons which perform thermally activated hopping due to anharmonic interaction with delocalized acoustic phonons. The hopping contribution to thermal conductivity exhibits a linear increase with temperature at lower temperatures and finally reaches a saturated value at higher temperatures.

2.2.2 Thermally activated hopping model

Thermally activated hopping (TAH) model [157] is an extension of the fracton hopping model initially developed by Alexander and co-workers [154, 158, 159] to explain the $\kappa(T)$ behavior of amorphous metallic glasses. The TAH model is different from the fracton hopping model as it does not consider the phonons to be fractons, since the mesoscale structure of the metallic glasses is not known. There are two basic features of the TAH model. The first is a phonon spectrum containing both low-frequency extended phonons and localized phonons above a minimum frequency ω_c , the phonon mobility edge. Phonons with frequency $\omega < \omega_c$ are extended while that for $\omega > \omega_c$ are localized. The second criterion is the presence of significant anharmonic forces to provide thermal activation to the localized phonons.

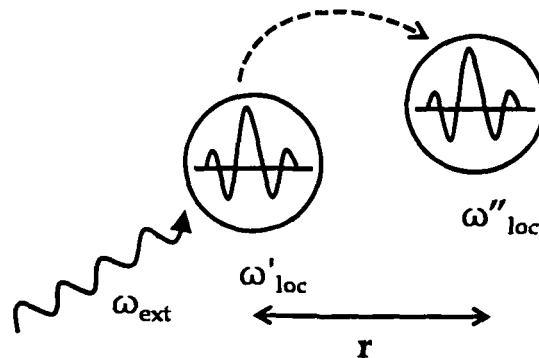


Figure 2.4: Schematic representation of hopping of localized phonons. A localized phonon with frequency ω'_{loc} hops to another site with frequency ω''_{loc} separated by a distance r . This hopping process is facilitated by an extended phonon ω_{ext} [160].

A similar hopping model extending the assumptions of TAH, and analogous to Mott VRH for localized electronic states was proposed to explain the heat transport arising from localized vibrational hopping [160]. This model predicts the existence of three types of excitations instead of two in the acoustic band of glasses: extended (or weakly localized), strongly localized (SL) and mesoscopically localized. The model [160], however considers coupling between the extended modes and the SL modes, but not between the SL and the

mesoscopically localized modes. The vibrational hopping of the SL modes depends on the anharmonic coupling between two localized (SL) states at different spatial positions, and a long-wavelength extended mode to make up the energy mismatch between the two localized states [161]. Figure 2.4 presents a schematic of hopping of the localized modes. The thermal conductivity arising from hopping of SL modes is given by [160, 161]:

$$\kappa_{hop}(T) = \frac{192 C_{eff}^2 k_B^2 G}{\pi^3 v_s^5 \rho_d^3 \xi_M^3 l_{ph}^2} T \quad (2.30)$$

where C_{eff} is the third-order anharmonic coupling constant, G is a constant of order unity, ρ_d is the mass density, v_s is the velocity of sound, l_{ph} is the localization length of a phonon and ξ_M^3 is the volume of finding a SL mode. The relation in Eq. (2.30) has been derived replacing the fractons by SL modes in the expression derived by Alexander et al. [158, 159] and applying Mott's [162] argument of variable-range localized electronic hopping to localized vibrational hopping.

CHAPTER 3

Experimental details

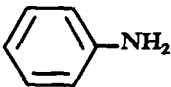
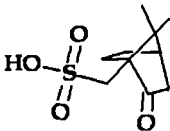

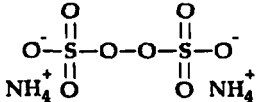
This chapter deals with the materials and methods used for the synthesis of different polyaniline nanostructures. Block diagrams and schematics of sample preparation processes and specification of the analytical techniques used for the characterization of the nanostructures, viz., high resolution transmission electron microscopy, X-ray diffraction, Fourier transform infrared spectroscopy and Raman spectroscopy have been mentioned. The techniques employed for the measurement of different transport properties, namely, dc conductivity, magnetoresistance, current-voltage characteristics, thermal conductivity as well as the thermodynamic property specific heat have been discussed briefly. The details of the measurement of magnetic properties have also been highlighted.

3.1 Materials

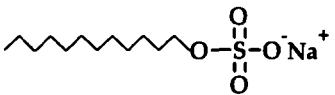
Aniline monomer was purchased from Merck for the synthesis of polyaniline (PANI) nanostructures. Hydrochloric acid (HCl; Merck), camphor sulfonic acid (CSA; Aldrich) and dodecyl benzene sulfonic acid (DBSA; Aldrich) were used as doping agents. Both CSA and DBSA were used as functional dopants i.e., these dopants control the morphology of the nanostructure as well as dope the polymer. Sodium dodecyl sulfate (SDS; Merck) was used as surfactant to form spherical micelles for the synthesis of nanoparticles. Ammonium persulfate (APS; Merck) was used as oxidant to initiate the polymerization. Carbon tetrachloride (CCl₄; Merck) and deionized water were used as solvents in the interfacial polymerization technique to synthesize nanofibers. Methanol (Merck) and acetone (Merck) were used to wash the obtained nanostructures.

Aniline was distilled under reduced pressure and stored in dark prior to use. All other chemicals and solvents were of analytical grade and used as received without further purification. The physicochemical properties of the materials used for the synthesis of PANI nanostructures in the present study are presented in Table 3.1.

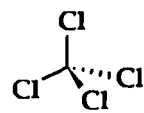
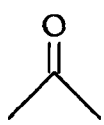
Table 3.1: Some physicochemical properties of the materials used for synthesis

Physicochemical properties of the monomer aniline						
Molecular formula	Molecular structure	Molar mass (g/mol)	Density at 25 °C (g/ml)	Melting point (°C)	Boiling point (°C)	Oxidation potential (V)
C ₆ H ₅ NH ₂		93.13	1.02	-6	184	0.9
Physicochemical properties of the dopants						
Dopant	Molecular formula	Molecular structure	Molar mass (g/mol)	Density at 25 °C (g/ml)	Melting point (°C)	Boiling point (°C)
Hydrochloric acid	HCl	H—Cl	36.46	1.2	-33	66
Camphor sulfonic acid	C ₁₀ H ₁₆ O ₄ S		232.30	1.3	200	N/A
Dodecyl benzene sulfonic acid	C ₁₈ H ₃₀ O ₃ S		326.49	1.06	10	82
Physicochemical properties of oxidant ammonium persulfate (APS)						
Molecular formula	Molecular structure	Molar mass (g/mol)	Density at 25 °C (g/cm ³)	Melting point (°C)	Boiling point (°C)	
(NH ₄) ₂ S ₂ O ₈		228.2	1.98	120	N/A	

Physicochemical properties of the surfactant sodium dodecyl sulfate (SDS)

Molecular formula	Molecular structure	Molar mass (g/mol)	Density at 25 °C (g/cm ³)	Melting point (°C)	Boiling point (°C)
NaC ₁₂ H ₂₅ SO ₄		288.372	1.01	206	N/A

Physicochemical properties of solvents

Solvents	Molecular formula	Molecular structure	Molar mass (g/mol)	Density at 25 °C (g/ml)	Melting point (°C)	Boiling point (°C)
Carbon tetrachloride	CCl ₄		153.8	1.58	-22.9	76.7
Acetone	C ₃ H ₆ O		58.08	0.791	-95	56
Methanol	CH ₃ OH	—OH	32.04	0.7918	-97.6	64.7

3.2 Synthesis of PANI nanostructures

3.2.1 Synthesis of PANI nanofibers

PANI nanofibers can be synthesized using several techniques both chemically and electrochemically. Different methods employed to fabricate nanofibers include hard-template method [163, 164], soft-template method [165], electrospinning [55], dilute polymerization [166], interfacial polymerization [56], seeding polymerization [167] and ultrasonic irradiation [168]. Of all the methods, interfacial polymerization is the most preferred because this technique is very simple, cost effective and yields a large quantity of nanofibers without the use of templates or functional dopants.

Nanofibers with diameter of tens of nanometer form in the early stage of chemical oxidative polymerization of aniline without the use of any template. It

was discovered that nanofibers are the fundamental morphological unit in conventional polymerization [50]. However, renucleation on the surface of already formed nanofibers leads to the formation of irregular shaped particles and finally granular aggregates [169]. In interfacial polymerization technique, the secondary growth on the nanofibers is restricted and a good quality of smaller diameter nanofibers is obtained. In this technique, the polymerization occurs at the interface of a heterogeneous organic-aqueous biphasic system. PANI formed at the interface is in hydrophilic emeraldine salt form and therefore diffuses quickly into the aqueous phase away from the reactive interface. Thus, the interface reactive sites become available for further polymerization avoiding the secondary growth on the already formed nanofibers. In this way, the nanofibers are collected from the aqueous part without any secondary overgrowth. Figure 3.1 depicts the schematic of the formation of PANI nanofibers by interfacial polymerization technique.

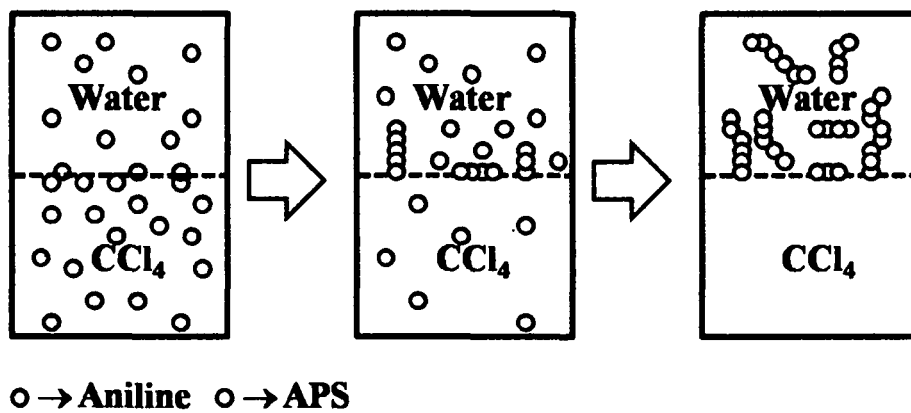


Figure 3.1: Schematic representation of the formation of nanofibers in the interfacial polymerization of PANI.

In the present study, interfacial polymerization technique has been used to synthesize PANI nanofibers doped with HCl. The block diagram of the synthesis route is shown in Figure 3.2. In this synthesis process, 0.04 M aniline was dissolved in 40 ml CCl_4 , which forms an organic solution. On the other hand, 0.02 M APS was dissolved in HCl mixed 40 ml deionized water. This

forms an aqueous solution which was carefully transferred over the organic solution forming an interface between the two layers. After 2 - 3 mins, green PANI forms at the interface and quickly diffuses into the aqueous phase owing to its hydrophilicity. After 24 h, the entire aqueous phase is completely filled with dark green PANI and the organic phase is red orange. PANI nanofibers were collected and washed several times with deionized water, methanol and acetone, and finally dried under vacuum at room temperature for 72 h. Three different samples of nanofibers were synthesized with 0.02 M (NF 1), 0.04 M (NF 2) and 0.06 M (NF 3) concentrations of HCl.

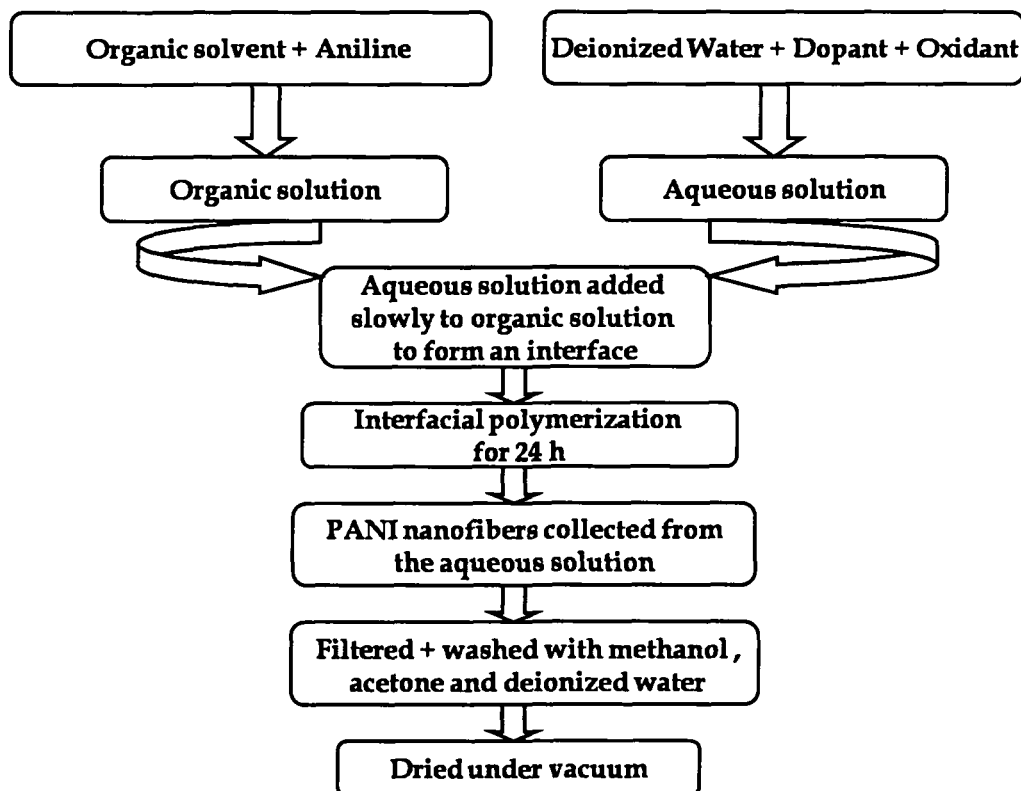


Figure 3.2: Block diagram of the synthesis route of PANI nanofibers by interfacial polymerization technique.

3.2.2 Synthesis of PANI nanoparticles

PANI nanoparticles can be synthesized using various techniques, such as emulsion polymerization [170], dispersion polymerization [171], interfacial

polymerization [172], and also by using micellar solutions of surfactants that act as soft-templates [48, 173]. Among all the techniques, the micellar soft-template method has gained attention due to the good quality uniformly shaped particles. In this method, the micelles formed by the surfactant determine the shape and size of the particles. Different types of surfactant such as anionic (e.g., sodium dodecyl sulfate, dodecyl benzene sulfonic acid), cationic (e.g., dodecyl trimethyl ammonium bromide) or non-ionic (e.g., Triton™ X-405) can be used as soft-templates for the formation of PANI nanoparticles [174]. The block diagram of the synthesis route of PANI nanoparticles using surfactant micelles as template is shown in Figure 3.3.

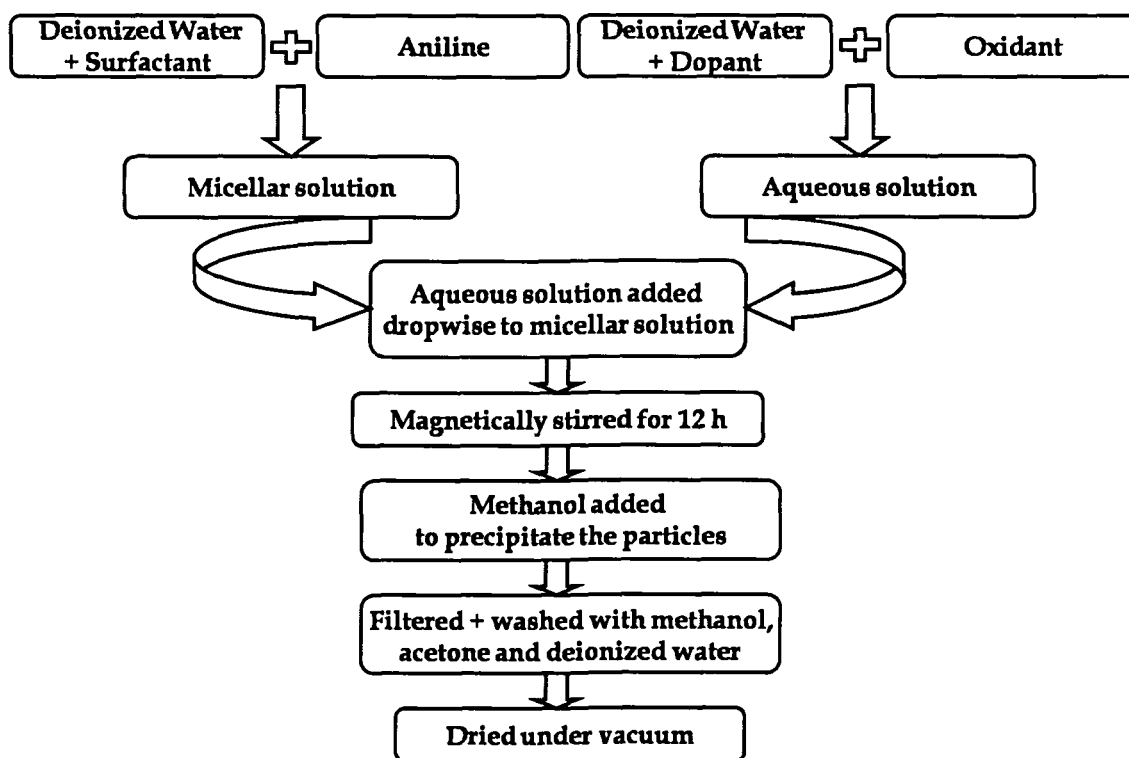


Figure 3.3: Block diagram of the synthesis of PANI nanoparticles via soft-template technique.

Surfactants are organic compounds that are amphiphilic i.e., they have both hydrophobic (tail) and hydrophilic (head) groups. The hydrophobic part usually consists of a hydrocarbon chain with an equivalent of 8 to 12 carbon

atoms, and can be aliphatic, aromatic or a mixture of both. The hydrophilic parts can be anionic, cationic or non-ionic which gives the primary classification of surfactants. In aqueous phase, surfactants form micelles where the hydrophobic tail forms the core of the micelle and the hydrophilic head is in contact with the surrounding liquid. The shape of the micelle depends on the chemical structure of the surfactant i.e., on the balance of the sizes of the hydrophobic tail and hydrophilic head. In the present study, sodium dodecyl sulfate (SDS) and dodecyl benzene sulfonic acid (DBSA) have been used as surfactants which form spherical micelles in water. Since DBSA is a functional dopant, it forms the micelle and also dopes the resultant PANI. In the synthesis process (Figure 3.3), DBSA is mixed in deionized water and then aniline is added which forms the micellar solution. On the other hand, in the oxidant solution, the dopant is not added as DBSA itself acts as the doping agent. The surfactant in aqueous medium forms micelles where the hydrophobic tail forms the core and the hydrophilic heads are in contact with the surrounding liquid. Aniline in water may exist in the form of anilinium cations or free aniline [175]. Anilinium cations are adsorbed on the micellar surface by electrostatic attraction with anionic surfactant molecules. Free aniline diffuses into the micelles. On addition of oxidant, the polymerization of aniline and anilinium molecules take place in the micelle-water interface, as hydrated oxidant molecules cannot penetrate inside the micelle surface [176]. As the polymerization proceeds, the micelles become bigger spheres through accretion depending on the local environment [48]. A schematic of the formation of PANI nanoparticles is depicted in Figure 3.4.

PANI nanoparticles doped with HCl and DBSA were synthesized using the micellar soft-template method as described above. Two different sets of nanoparticles were synthesized using surfactants SDS and DBSA. Aqueous micellar dispersion was prepared by dissolving 0.004 M of SDS in 40 ml deionized water with slow stirring. 0.04 M aniline was then added to the SDS solution. Subsequently, 0.02 M APS was dissolved in HCl solution which was

prepared by dissolving HCl in deionized water to form the aqueous phase. The aqueous solution was then added dropwise to the micellar solution and allowed to polymerize in a magnetic stirrer for about 15 h. The green precipitate formed was filtered and washed with deionized water, methanol and acetone several times to remove the unreacted chemicals, aniline monomer and SDS. The precipitate was finally dried in a vacuum for 72 h. Three different samples of PANI nanoparticles were prepared using 0.02 M (NPa 1), 0.04 M (NPa 2) and 0.06 M (NPa 3) HCl concentration.

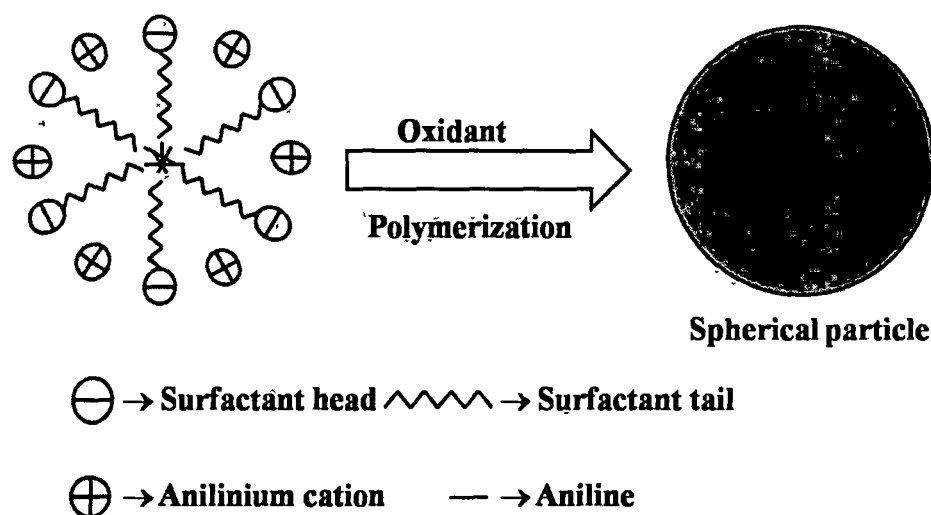


Figure 3.4: Schematic of the formation of a nanoparticle in the micellar solution of surfactant.

DBSA being a functional dopant, the above procedure was repeated for the synthesis of DBSA doped nanoparticles using 0.02 M (NPb 1), 0.04 M (NPb 2) and 0.06 M (NPb 3) concentrations of DBSA. In this case, aqueous micellar solution was prepared by dissolving DBSA in deionized water. 0.04 M aniline was added to the DBSA solution. On the other hand 0.02 M APS was added to 40 ml water which was poured dropwise to the micellar solution. DBSA acts a dual role of a surfactant as well as of a dopant. So, neither it was required to remove the DBSA micelles, nor the addition of a separate doping agent.

3.2.3 Synthesis of PANI nanotubes

PANI nanotubes can be synthesized both electrochemically and chemically using hard-templates or soft-templates. Hard-templates include porous membranes of polycarbonate (PC) [177], alumina (Al_2O_3) [178] and particle track etched membrane (PTM) [179]. Some other forms of hard-templates used are methyl orange/ FeCl_3 nanofibers [180], halloysite nanotubes [181] and silica nanotubes [182]. Soft-template method, also known as the self-assembly method includes the use of structure-directing agents such as surfactants and functional organic acid dopants. Surfactants such as cetyl methyl ammonium bromide (CTAB) [183] and sodium dodecyl benzene sulfonate (SDBS) [175] are used for the synthesis of PANI nanotubes. Of all these template methods, synthesis of nanotubes using organic sulfonic acids such as β -naphthalene sulfonic acid (β -NSA) [184], azo benzene sulfonic acid (ABSA) [185], camphor sulfonic acid (CSA) [186] and PAMAM4.0 [naphthyl(SO_3H) $_2$] $_{24}$ or $\text{C}_{60}(\text{OSO}_3\text{H})_6$ [187] is the most sought after synthesis route, since these acids control the morphology as well as dope the resulting polymer. For the present study, the nanotubes were synthesized using CSA, which is a functional dopant.

The block diagram of the synthesis route of PANI nanotubes is shown in Figure 3.5. In a typical synthesis procedure, CSA is dissolved in deionized water and then aniline is added forming aniline-CSA salt complexes. This salt can assemble into micelles in aqueous solution because CSA has a characteristic amphiphilic structure with hydrophilic $-\text{SO}_3\text{H}$ group and lipophilic $\text{C}_{10}\text{H}_{15}\text{O}-$ group. The micelles composed of CSA anion and anilinium cations coexist forming a double electronic layer [188]. These micelles act as templates in the formation of PANI-CSA nanotubes. When the oxidant is added, polymerization occurs and takes place only at the micelle-water interface, because the oxidant is water-soluble. With the polymerization proceeding, the micelles become bigger tubes by elongation [189]. Since, CSA also dopes the resulting polymer; it is not required to remove CSA after

synthesis. Figure 3.6 represents the schematic of the formation of PANI-CSA nanotubes.

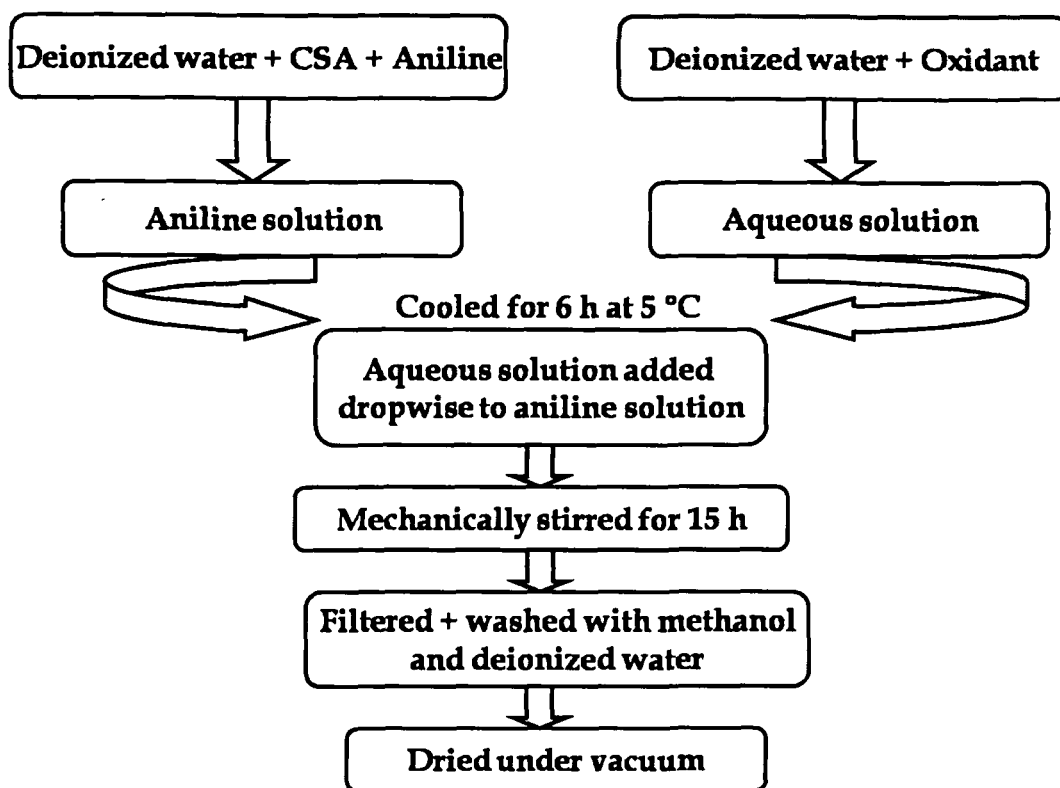


Figure 3.5: Block diagram of the synthesis of PANI nanotubes via soft-template technique using CSA.

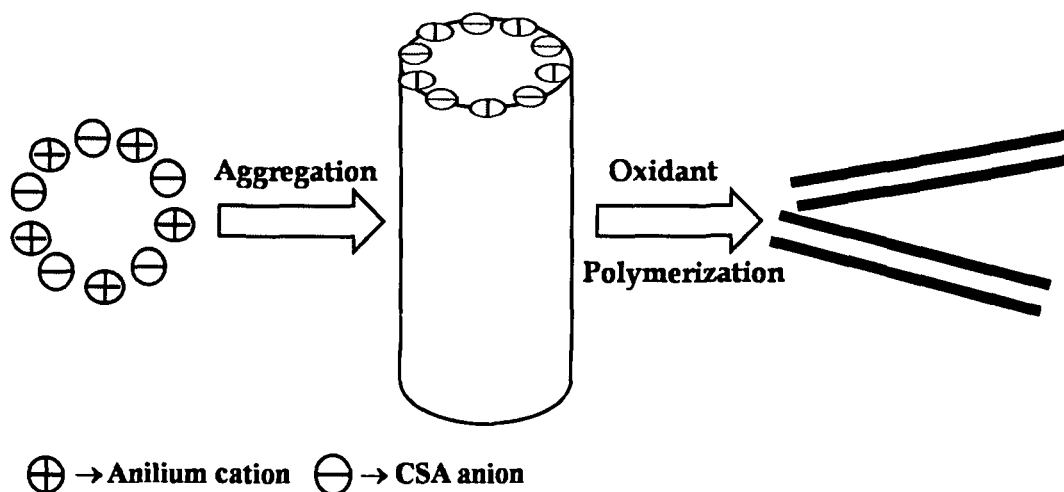


Figure 3.6: Schematic of the formation of PANI nanotubes in the micellar solution of CSA.

In the present work, CSA was dissolved in 40 ml deionized water upon magnetic stirring whereupon 0.04 M aniline monomer was added. On the other hand, 0.02 M APS was also dissolved in 40 ml water and both the solutions were cooled to about 5 °C. Subsequently, the APS solution was added slowly into the aniline-CSA salt solution. Once all APS was added, the mixture was magnetically stirred for 15 h. The precipitate was then washed with deionized water, methanol and acetone several times, and finally dried at room temperature in a dynamic vacuum for 72 h. Four different samples of nanotubes were synthesized with 0.002 M (NT 1), 0.01 M (NT 2), 0.02 M (NT 3) and 0.04 M (NT 4) concentrations of CSA.

3.3 Characterization techniques

3.3.1 High resolution transmission electron microscopy

High resolution transmission electron microscopy (HRTEM) was carried out to gain the morphological information of shape and size of the nanostructures. HRTEM has become a powerful tool to study the nanoscale properties of materials in nanoscience and nanotechnology due to its high resolution [190]. The HRTEM micrographs were recorded using a JEOL JEM-2100 transmission electron microscope. The micrographs have been taken at 200 kV accelerating voltage at different magnifications according to need. The samples were prepared by depositing a drop of well diluted PANI suspension onto a carbon coated copper grid and dried in an oven at 50 °C for 1 h.

3.3.2 X-ray diffraction

X-ray diffraction (XRD) studies were performed to determine the crystalline phases of PANI. Undoped PANI is generally amorphous while doped samples show semi-crystalline nature. Their crystallinity arises due to chain folding or due to the formation of single or double helices, for at least part of their chain length [191]. The local range-of-order in polymer chains is referred to as the

domain length (L) and is in the range of angstroms (\AA). The X-ray diffraction patterns of the present PANI nanostructures were recorded using a Rigaku Miniflex diffractometer with Cu K_{α} radiation ($\lambda = 1.5406 \text{\AA}$). The angular range spread over the region between 2° and 50° in 2θ , in steps of 0.05° .

3.3.3 Fourier transform infrared spectroscopy

Fourier transform infrared spectroscopy (FTIR) provides specific information regarding the vibration and rotation of chemical bonds and molecular structure, making it useful for characterization and identification of organic molecules, functional groups and molecular structure of organic compounds. An infrared spectrum represents a fingerprint of a sample with absorption peaks corresponding to the frequencies of vibrations between the bonds of atoms constituting the material. Each material is a unique combination of atoms; hence no two compounds can produce the same infrared spectrum. FTIR can thus result in qualitative identification of a material. Besides, the size of the peaks in the spectrum is a direct indication of the amount of the material present. The FTIR studies in the present PANI nanostructures were carried out to understand the molecular structure, and the effect of dopant and doping level on the vibration of the bonds in PANI. FTIR spectra in the mid IR region of $400 - 4000 \text{ cm}^{-1}$ were recorded with a Perkin Elmer spectrum 100 FTIR spectrometer with a resolution of 1 cm^{-1} using the standard potassium bromide (KBr) pressed pellet technique. Powder PANI samples were mixed with KBr and pressed using a hydraulic press to form pellets. The spectra were baseline corrected for better visibility.

3.3.4 Raman spectroscopy

Raman spectroscopy helps to identify the molecular structure of material since the vibrational information is specific to chemical bonds and symmetry of molecules. It also provides a molecular fingerprint similar to that of FTIR. Raman spectroscopy was used as a complement technique to infrared

spectroscopy for identification of the characteristic vibrational peaks of PANI. Raman spectroscopy of PANI can give information regarding both the crystalline arrangement i.e., structure as well as the oxidation and protonation state. The Raman spectroscopy measurements in the range of 100 - 1800 cm^{-1} were carried out at room temperature (25 °C) on pressed pellets of the powdered PANI samples using a HORIBA Jobin Yvon HR800 Raman spectrometer equipped with Ar 488 nm laser and charge coupled device (CCD) detector.

3.4 Transport property measurement techniques

3.4.1 *DC conductivity and Magnetoresistance*

DC conductivity and magnetoresistance measurements were performed using the standard four probe technique. The measurements were carried out on rectangular shape of samples with typical dimension $\sim 3.2 \times 2.5 \times 2.1 \text{ mm}^3$ cut from disk shaped pellets. The samples were glued to the sample holder using GE Varnish. Electrical contacts were made using highly conducting silver paste and copper wires. The dc conductivity measurements were performed in the temperature range of 5 - 300 K, where the low temperature was achieved using liquid helium. The isothermal magnetoresistance measurements were done at various temperatures such as, 30, 50, 100, 200 and 300 K in the magnetic field range of 0 - 8 T. The magnetic field was acquired using a superconducting solenoid magnet made by Oxford Instruments, UK, and the field was applied parallel to the sample. The measurement was done using a home build probe. Lakeshore temperature controller 340, Keithley source meter 2400 and Keithley digital voltmeter 180 were used for the measurements. Figures 3.7 (a & b) depict the setup used for measuring dc conductivity and magnetoresistance, and a schematic for four probe measurement, respectively.

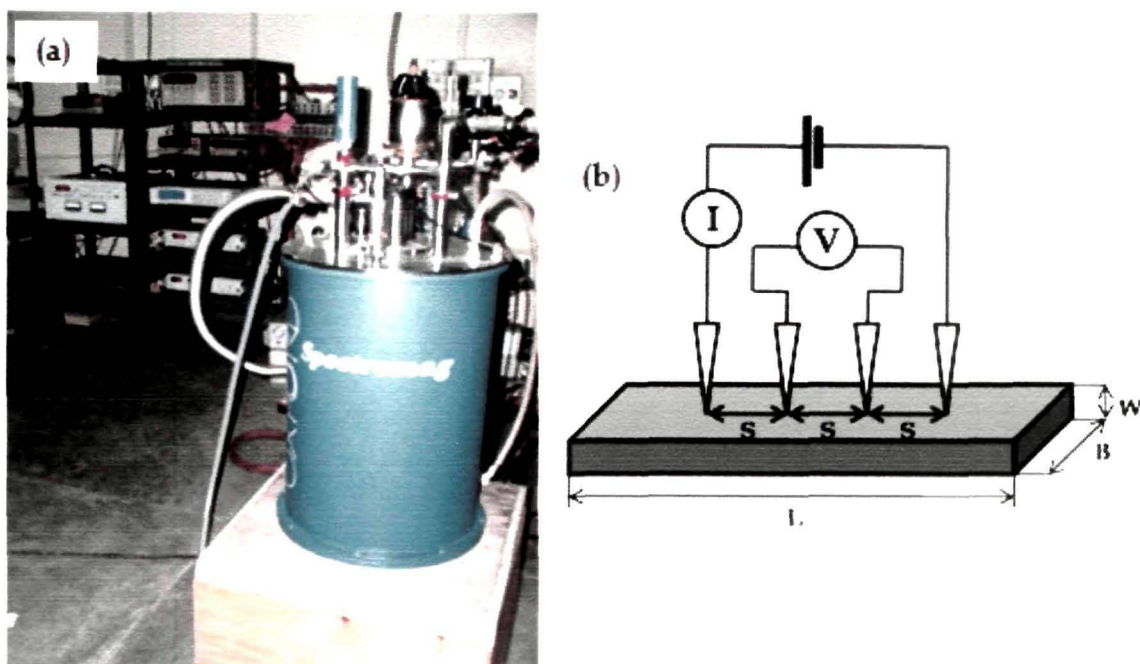


Figure 3.7: (a) The setup used for measuring dc conductivity with variation of temperature and magnetic field, and (b) schematic of four probe measurement.

3.4.2 Current-voltage characteristics

Steady state current (I) - voltage (V) measurements were performed on compressed pellets of the PANI nanostructures. The pellets were about 0.2 mm thick with diameter about 10 mm. The pellets were coated with silver (Ag) on both sides to make Ag/PANI/Ag sandwich structures. Work function of silver being 4.7 eV, it makes Ohmic contacts with PANI, since its work function is 4.3 eV. The isothermal I - V characteristics were carried out in the temperature range of 80 - 300 K using a Lakeshore 340 temperature controller and a Keithley 2612A system source meter. The curves were obtained by scanning the voltage from -5 to 5 V with a step of 0.2 V. Liquid nitrogen was used to acquire the low temperature. The typical setup used for I - V measurements has been shown in Figure 3.8.

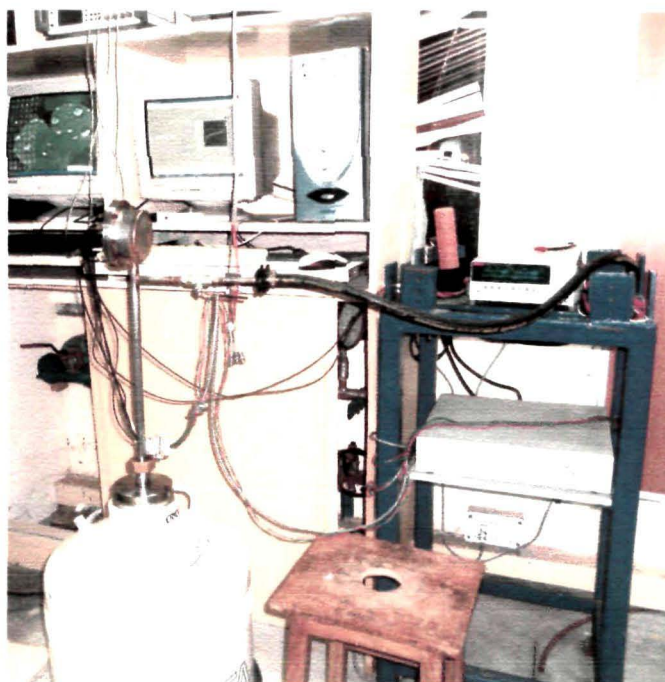


Figure 3.8: The setup used for measuring current-voltage characteristics.

3.4.3 Thermal conductivity

The thermal conductivity measurements were carried out in a closed-cycle refrigerator in the temperature range of 10 – 300 K, using a direct heat-pulse technique. The pelletized samples were cut into rectangular parallelepiped shape with one end of the sample glued (with thermal epoxy) to a copper block that served as a heat sink, while a calibrated chip resistor as a heat source glued to the other end. The temperature difference was measured by using an E-type differential thermocouple with junctions thermally attached to two well-separated positions along the sample. The stray thermal emfs were eliminated by applying long current pulses (~ 100 seconds) to the chip resistor, where the pulses appear in an off-on-off sequence. The temperature difference was controlled to be less than 1 K to minimize the heat loss through radiation, and the sample space was maintained in a good vacuum (approximately 10^{-4} torr) during measurements. All experiments were performed while warming with a rate slower than 20 K/h. The schematic of the setup used for measuring thermal conductivity is shown in Figure 3.9.

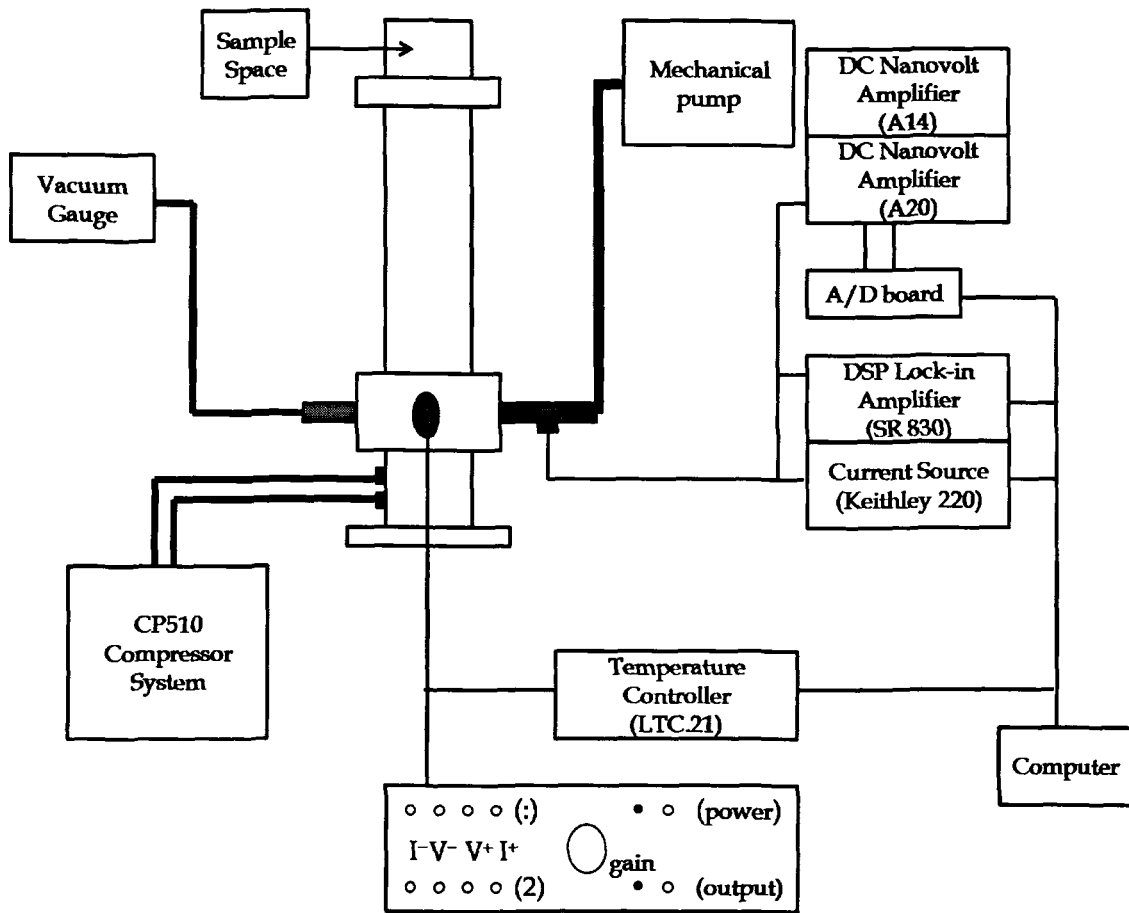


Figure 3.9: Schematic of the setup used for measuring thermal conductivity.

3.4.4 Specific heat

The specific heat was measured using a commercial differential scanning calorimeter, DSC (Model: SETARAM, DSC-131) with a precision better than 10%. A DSC measures the heat of a sample relative to a reference with a linear temperature ramp. Endothermic heat flows into the sample and exothermic heat flows out of the sample. A schematic of the working principle of a DSC has been shown in Figure 3.10(a). The calorimeter consists of a sample holder and reference holder as shown in the figure. A resistance heater and a temperature sensor are attached under each holder. Currents are applied to each heater to increase the temperature at specific rate, and the difference in the power of the two holders to maintain the same temperature is used to

calculate the specific heat. The image of the DSC instrument (SETARAM Instrumentation) used for measuring specific heat has been shown in Figure 3.10(b). Powder sample of about 100 mg was used for the measurements. Measurements were performed over the temperature range of 158 - 300 K. Samples were hermetically sealed in a standard alumina pan in the nitrogen-filled glove box environment. Data were collected using a two run method (sample and blank runs), with a heating rate of 10 °C/min.

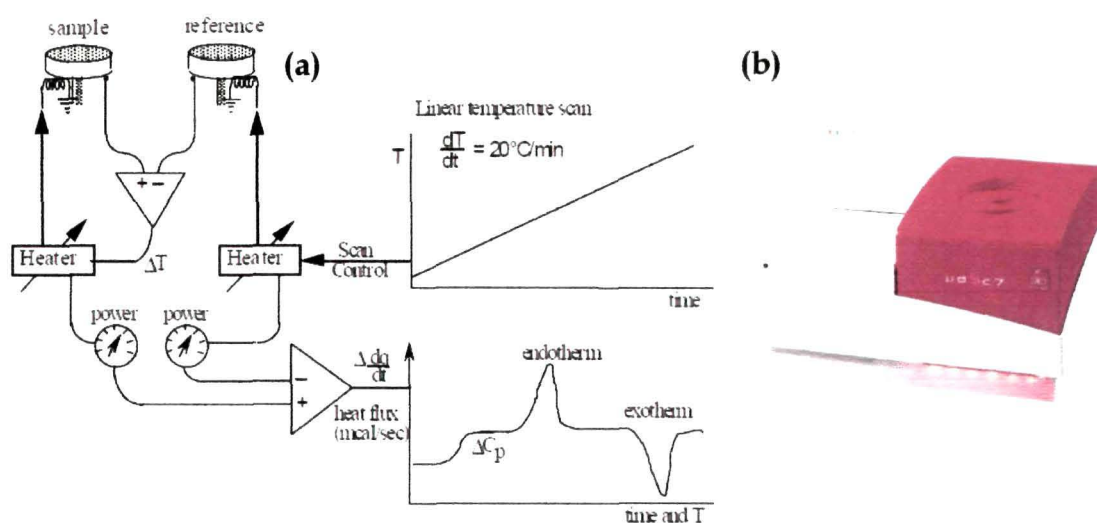


Figure 3.10: (a) Schematic of working principle of a DSC (Courtesy: <http://www.colby.edu/chemistry>) and (b) DSC instrument (SETARAM Instrumentation: DSC-131) used for specific heat measurements.

3.5 Magnetic property measurement technique

Magnetization (M), as a function of temperature (T) and magnetic field (H) has been measured using a superconducting quantum interference device (SQUID) magnetometer (MPMS XL-7, Quantum Design). The samples used for measurements (weight about 60 mg and rectangular shapes) were cut from disk shaped pellets prepared by pressing the polymer powder. The samples were then wrapped in Teflon tape and mounted into a non-magnetic polyethylene straw and placed into the magnetometer. The data for $M(T)$ were collected at

each temperature by fixing the temperature and scanning the sample through the superconducting coil multiple times and averaging the data. In case of $M(H)$ measurements, similar scanning process was followed to obtain the data at each stabilized magnetic field. The $M(T)$ measurements were done in 10 kOe magnetic field in the temperature range of 2 - 300 K, while the $M(H)$ measurements were carried out at 10 K in the field range upto 70 kOe. Figures 3.11 (a & b) show the image of the SQUID magnetometer used for magnetization measurements and the schematic of superconducting coil through which a sample is scanned, respectively.



Figure 3.11: (a) SQUID magnetometer (Quantum Design: MPMS XL-7) used for magnetic property measurements and (b) schematic of superconducting coil through which sample is scanned.

CHAPTER 4

Structural and vibrational spectroscopic studies of polyaniline nanostructures

This chapter focuses on the structural and vibrational spectroscopic characterizations of polyaniline nanostructures. The morphological studies were carried out using high resolution transmission electron microscope. X-ray diffraction measurements were done to study the ordering of PANI chains in the nanostructures. The vibrational properties were studied using Fourier transmission infrared spectroscopy and Raman spectroscopy.

4.1 Introduction

Nanotechnology has emerged as one of the most powerful and unique interdisciplinary research area which has given rise to several innovations advancing the present world technology. One of its most attractive areas is the polymer nanotechnology owing to the small size of the polymer chains. The development and progress in nanotechnology tools has provided an excellent opportunity to investigate the individual chains of conducting polymers which can serve as molecular wires. Besides that, conducting polymer being a member of soft-matter family, have amazing flexibility for the preparation of various nanostructures for use in nanodevices [93]. In recent years polyaniline (PANI) nanostructures among the family of conducting polymer nanostructures have

attracted attention due to their considerable increase in dispersibility and processability, and subsequently enhanced performance in devices in comparison to its bulk form i.e., the agglomerated granular form [50, 192-194]. Of late, the interest in developing zero-dimensional (nanoparticles), one-dimensional (nanofiber, nanowires, nanorods, nanotubes, needle-like nanostructures), two-dimensional (nanosheets, nanoflakes, nanodisks) and three-dimensional PANI nanostructures (dendritic, brain-like, flower-like, urchin-like nanostructures) have increased tremendously. The major focus of research in this field has been the preparation, characterization, processing of the nanostructures, and subsequent application in devices.

Four different nanostructure systems of PANI, viz., hydrochloric acid (HCl) doped nanofibers (NF) and nanoparticles (NP_a), dodecyl benzene sulfonic acid (DBSA) doped nanoparticles (NP_b) and camphor sulfonic acid (CSA) doped nanotubes (NT) have been synthesized. The HCl doped PANI nanofibers were synthesized in an aqueous-organic interface by interfacial polymerization technique, while the other nanostructure systems were prepared by self-assembly method using surfactants and amphiphilic acids. Different samples of each nanostructure were prepared by varying the concentration of dopant. The samples were numbered in ascending order of the doping level. The details of the synthesis processes are included in section 3.2 of Chapter 3.

This chapter includes the detailed studies of structural and vibrational spectroscopic characterizations of the nanostructures. These characterizations are required for complete understanding of the transport and magnetic properties of PANI nanostructures. High resolution transmission electron microscopy (HRTEM) has been used to determine the shape, size and size distribution of the nanostructures. The crystallinity of the nanostructures has been determined using X-ray diffraction (XRD) studies. Fourier transform infrared spectroscopy (FTIR) and Raman spectroscopy revealed the effect of doping level on the vibration of the bonds.

4.2 Structural characterizations

4.2.1 High resolution transmission electron microscopy

Figures 4.1 (a & b) show the HRTEM images of PANI nanofibers doped with 0.02 M (NF 1) and 0.06 M (NF 3) HCl, respectively which were synthesized by interfacial polymerization technique. The images depict randomly oriented nanofibers with diameter in the range of 10 - 30 nm, while the length varies from a few nanometers to hundreds of nanometer.

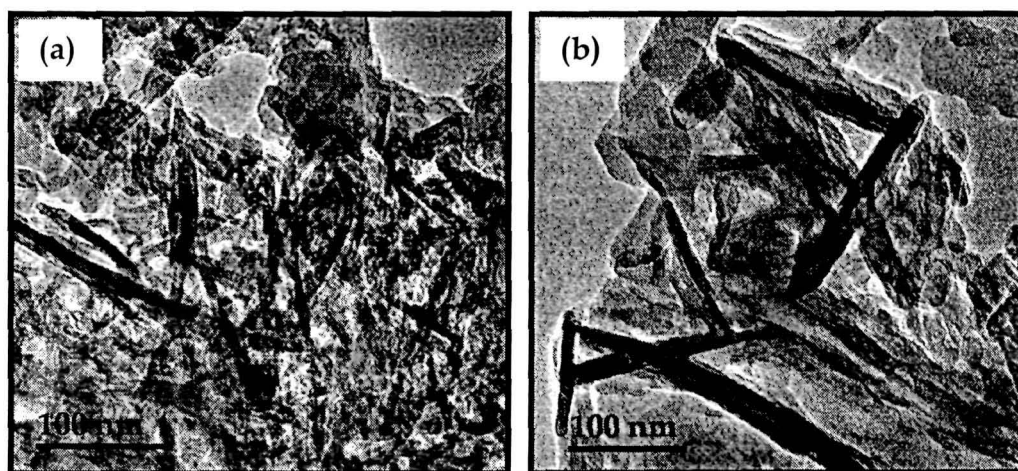


Figure 4.1: HRTEM images of PANI nanofibers doped with (a) 0.02 M (NF 1) and (b) 0.06 M (NF 3) HCl.

The distribution of fiber diameters of NF 1 and NF 3 samples are shown as histograms in Figures 4.2 (a & b), respectively. The bars represent the number of fibers with the corresponding diameter shown on the abscissa. The diameter of the nanofibers has been determined from the HRTEM images using Image J software. As can be seen from the figure, the diameters vary from 5 - 35 nm for both the samples. The average diameter of the distribution is found by fitting with Gaussian distribution function using OriginPro 8.5 software. The average diameter of NF 1 is 12.64 nm and that of NF 3 is 11.54 nm. It is thus observed that the concentration of dopant does not affect the fiber diameter of PANI synthesized by interfacial polymerization method.

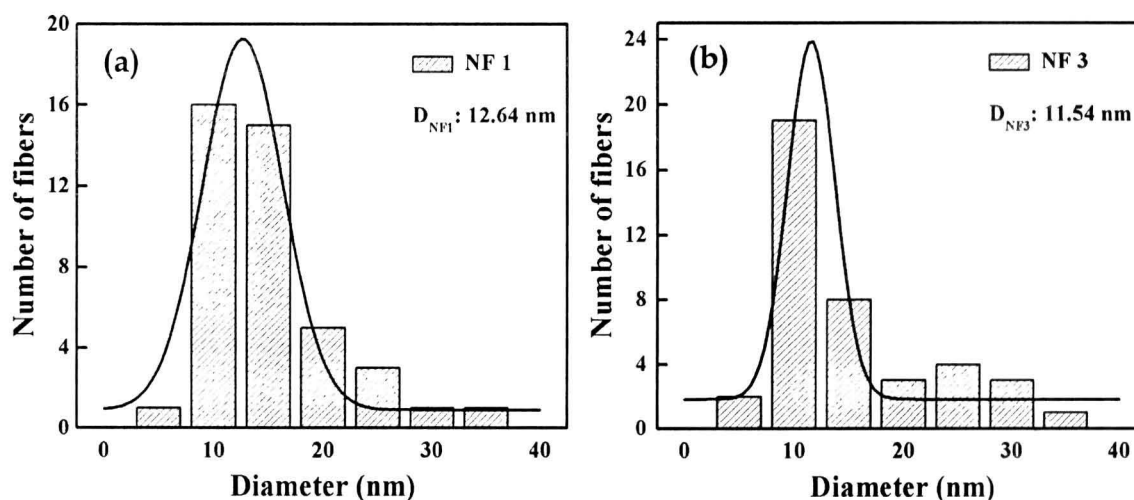


Figure 4.2: Diameter distributions of PANI nanofibers doped with (a) 0.02 M (NF 1) and (b) 0.06 M (NF 3) HCl.

Figures 4.3 (a & b) represent the respective HRTEM images of 0.02 M (NPa 1) and 0.06 M (NPa 3) HCl doped PANI nanoparticles synthesized by self-assembly method, using sodium dodecyl sulfate (SDS) as the structure-directing agent. A distribution of well separated spherical particles with size in the range of 2 - 10 nm is observed from the images.

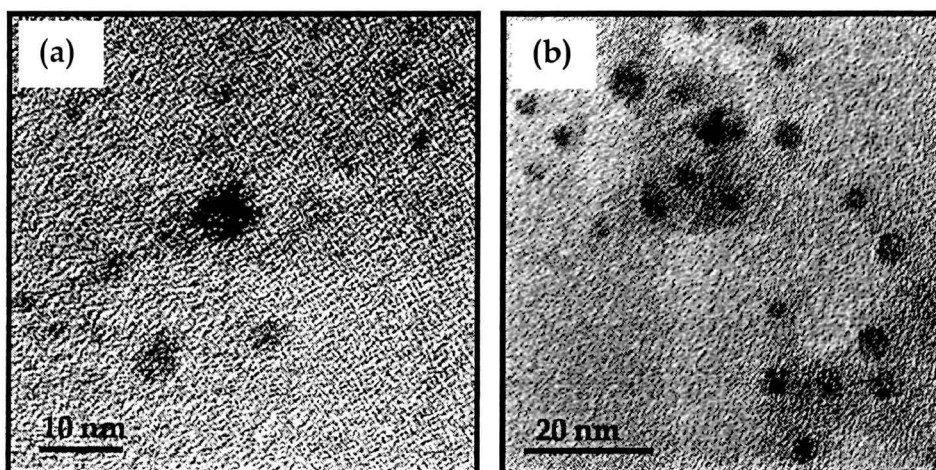


Figure 4.3: HRTEM images of PANI nanoparticles doped with (a) 0.02 M (NP a 1) and (b) 0.06 M (NP a 3) HCl.

The histogram of the diameter distribution of NPa 1 and NPa 3 obtained from the HRTEM images are shown in Figures 4.4 (a & b). From the Gaussian fitting of the distribution, the average diameter has been found to be 2.41 nm for NPa 1 and 3.71 nm for NPa 3. The diameter of the particles does not vary with dopant (HCl) concentration and depends only on the size of SDS micelles. SDS concentration was kept constant during synthesis, and hence the micellar size remains constant for both the cases.

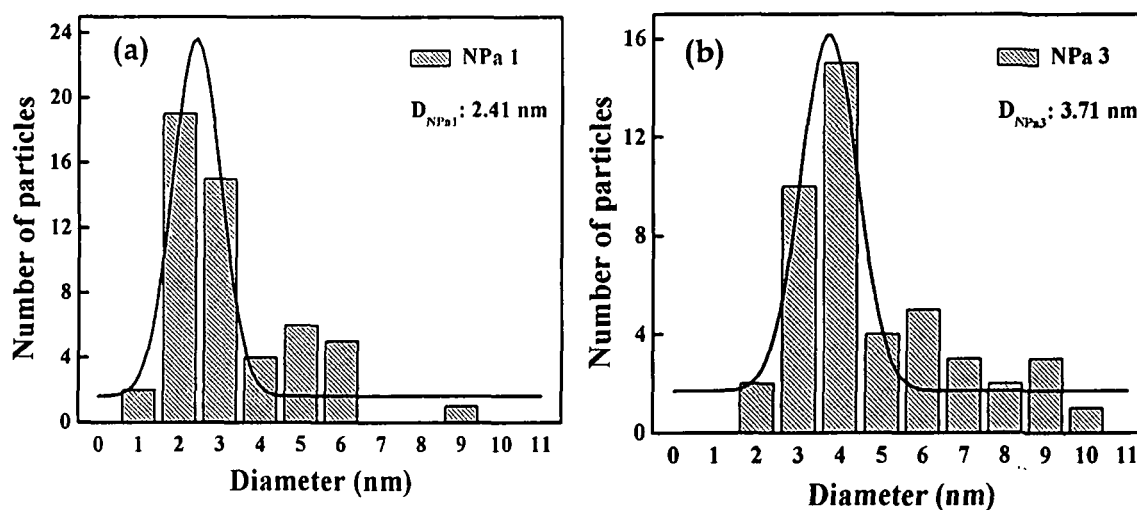


Figure 4.4: Diameter distributions of PANI nanoparticles doped with (a) 0.02 M (NPa 1) and (b) 0.06 M (NPa 3) HCl.

The HRTEM images of 0.02 M (NPb 1) and 0.06 M (NPb 3) DBSA doped nanoparticles synthesized by self-assembly method are depicted in Figures 4.5 (a & b). It is observed from the Figure 4.5 (a), that the particles of sample NPb 1 are spherical and well separated with diameters in the range of 3 - 12 nm. However, from the Figure 4.5 (b) of sample NPb 3, it can be seen that the particles are larger in size with diameter in the range of 25 - 60 nm and are agglomerated in the form of randomly oriented necklace. The distributions of particle diameter for both the samples are shown in Figures 4.6 (a & b). The Gaussian fit of the distributions yields the average diameter of the particles. The average diameter of the particles of sample NPb 1 is 5.96 nm while that in case of NPb 3 is 35.44 nm. The larger size of NPb 3 particles can be attributed to the

larger micellar size formed due to more DBSA concentration. Since DBSA acts as a functional dopant, increasing the doping level i.e., increasing the DBSA content leads to bigger micelles due to larger number of DBSA molecules in solution.

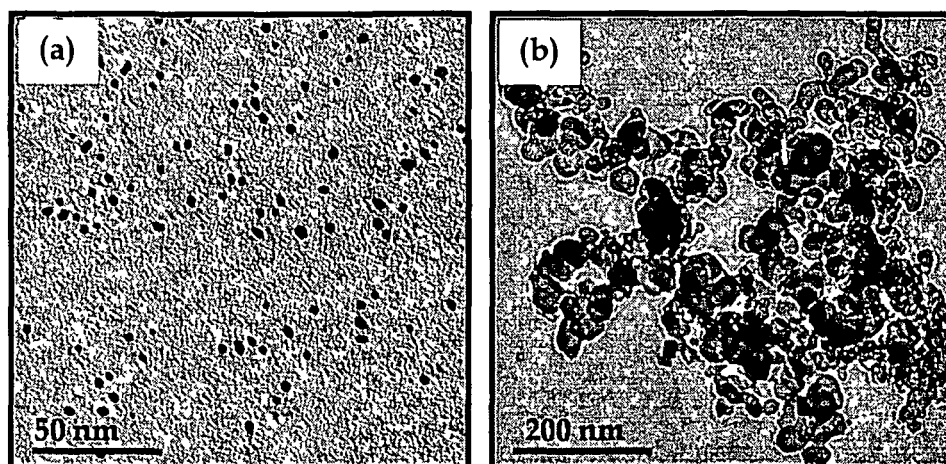


Figure 4.5: HRTEM images of PANI nanoparticles doped with (a) 0.02 M (NPb 1) and (b) 0.06 M (NPb 3) DBSA.

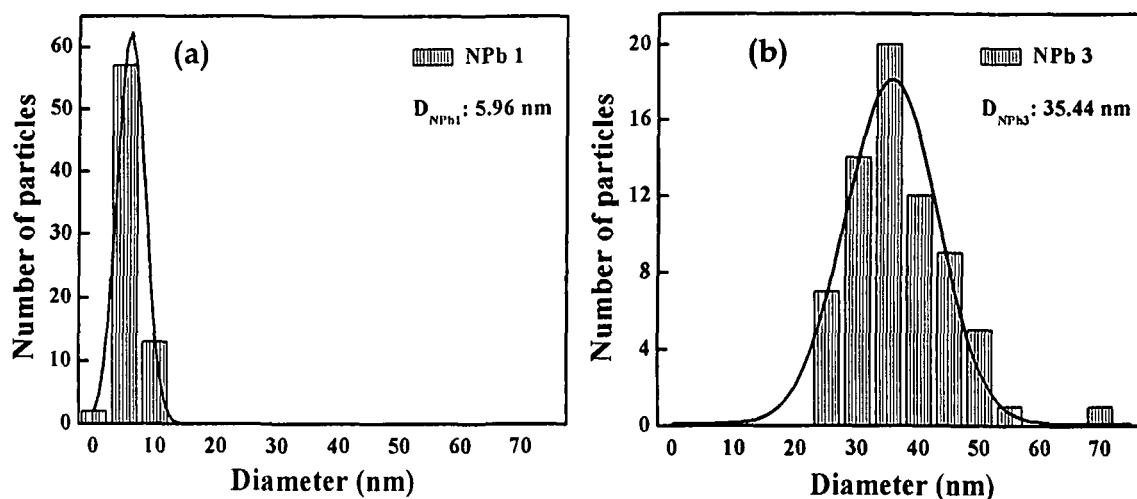


Figure 4.6: Distributions of diameter of PANI nanoparticles doped with (a) 0.02 M (NPb 1) and (b) 0.06 M (NPb 3) DBSA.

Figures 4.7 (a & b) show the HRTEM images of 0.002 M (NT 1) and 0.04 M (NT 4) CSA doped PANI nanotubes synthesized by self-assembly method. Hollow entangled nanotubes with rough inner and outer surface are observed

from Figure 4.7 (a) of NT 1. The inset of Figure 4.7 (a) shows the two walls of a nanotube. The walls look like the two banks of a river with crests and troughs. Figure 4.7 (b) shows the HRTEM image of a single nanotube of NT 4 sample. It is observed from both the images that the diameter is not constant for the same nanotube.

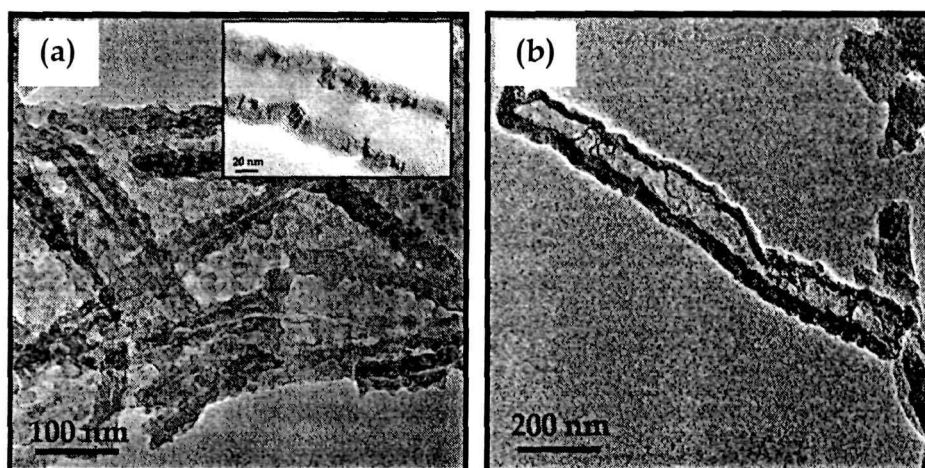


Figure 4.7: HRTEM images of PANI nanotubes doped with (a) 0.002 M (NT 1) and (b) 0.04 M (NT 4) CSA. Inset (a) shows the two walls of a nanotube.

The histograms of the distribution of inner and outer diameter of NT 1 sample are shown in Figures 4.8 (a & b), and that of NT 4 are shown in Figures 4.9 (a & b). Since the nanotubes are not uniform, different observations from a single nanotube are also taken into consideration. The inner diameter (ID) of the nanotubes in NT 1 sample varies from 30 to 70 nm while that for NT 4, it varies from 50 to 110 nm. Similarly, the outer diameter (OD) of NT 1 varies from 70 to 110 nm whereas that for NT 4, the OD is in the range of 80 - 160 nm. The Gaussian distribution fitting of the histogram of the diameter distributions gives the average ID and OD for each sample. The average ID for NT 1 is found to be 38.22 nm and that for NT 4 is 91.34 nm. Average OD is found to be 99.23 nm for NT 1 and 142.16 nm for NT 4. The increasing diameter with increasing concentration of dopant may be explained similarly as in case of DBSA doped nanoparticles. CSA being a functional dopant, increasing its concentration increases the micellar size and hence the diameter of the tubes increases.

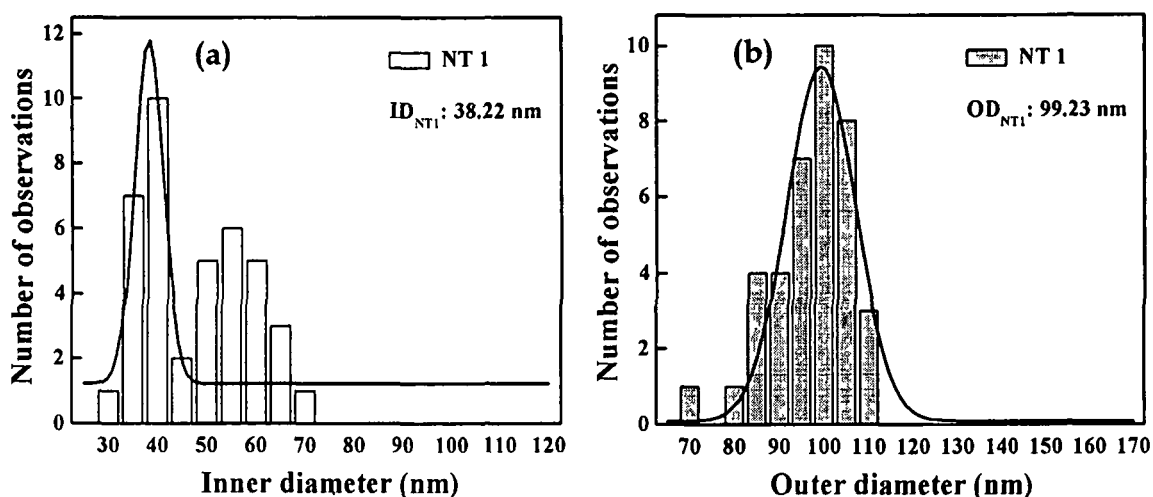


Figure 4.8: Distributions of (a) inner and (b) outer diameter of PANI nanotubes doped with 0.002 M CSA (NT 1).

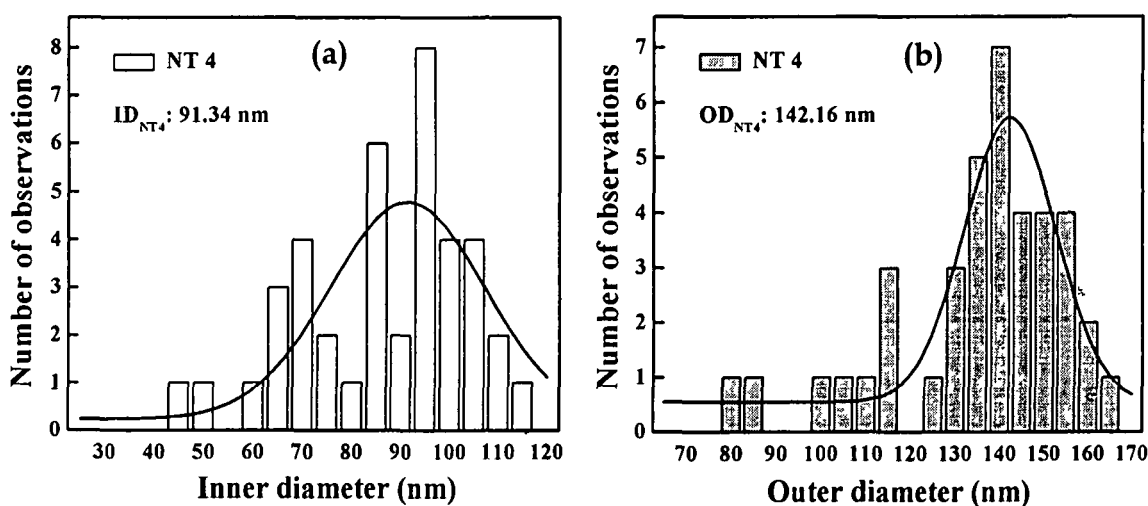


Figure 4.9: Distributions of (a) inner and (b) outer diameter of PANI nanotubes doped with 0.04 M CSA (NT 4).

4.2.2 X-ray diffraction studies

Figures 4.10 (a & b) display the XRD patterns of HCl doped PANI nanofibers and nanoparticles, respectively over the 2θ range from 10° to 45° . As can be seen from the figure, two broad peaks centered at 20° and 25° appear for all the nanofiber and nanoparticle samples. PANI exists in two different crystalline forms depending upon the method of preparation, namely, Emeraldine salt I

(ES-I) and Emeraldine salt II (ES-II). PANI synthesized directly in the emeraldine salt form has the ES-I structure with a pseudo-orthorhombic unit cell of lattice parameters $a = 4.5 \text{ \AA}$, $b = 5.9 \text{ \AA}$, $c = 9.6 \text{ \AA}$ and $V = 245 \text{ \AA}^3$ [195]. The $2\theta = 20^\circ$ peak corresponds to (100) reflections along the chain (parallel periodicity) and $2\theta = 25^\circ$ peak corresponds to (110) reflections in perpendicular direction (perpendicular periodicity). The d-spacing of 3.5 \AA ($2\theta = 25^\circ$) signifies the inter-chain periodicity, implying a close contact distance between two adjacent PANI chains with phenyl rings nearly located in the plane of nitrogen atoms [196].

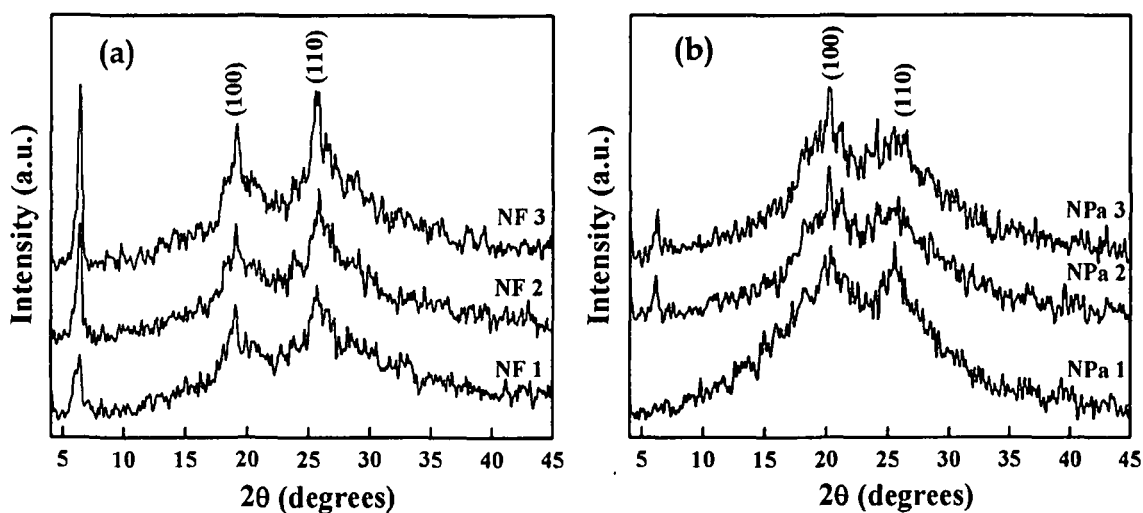


Figure 4.10: X-ray diffraction patterns of HCl doped PANI (a) nanofibers and (b) nanoparticles.

It is observed that the (110) peak in case of HCl doped nanofibers is intense than the (100) peak, whereas the opposite trend is observed for HCl doped nanoparticles indicating greater periodicity in that direction. A peak centered at $2\theta = 6.4^\circ$ is observed which arises from the reflection to periodic distance of dopant counterion and N atom of adjacent main chains [197]. The intensity of this peak is found to increase with doping level and is not observed for the lowest doped nanoparticles. It is observed that this peak is very much intense in case of the nanofibers than that of the nanoparticles. This indicates that the ordering takes place along the length of the nanofibers, as the lateral

diameter of the nanofibers and diameter of the nanoparticles are almost of the same order.

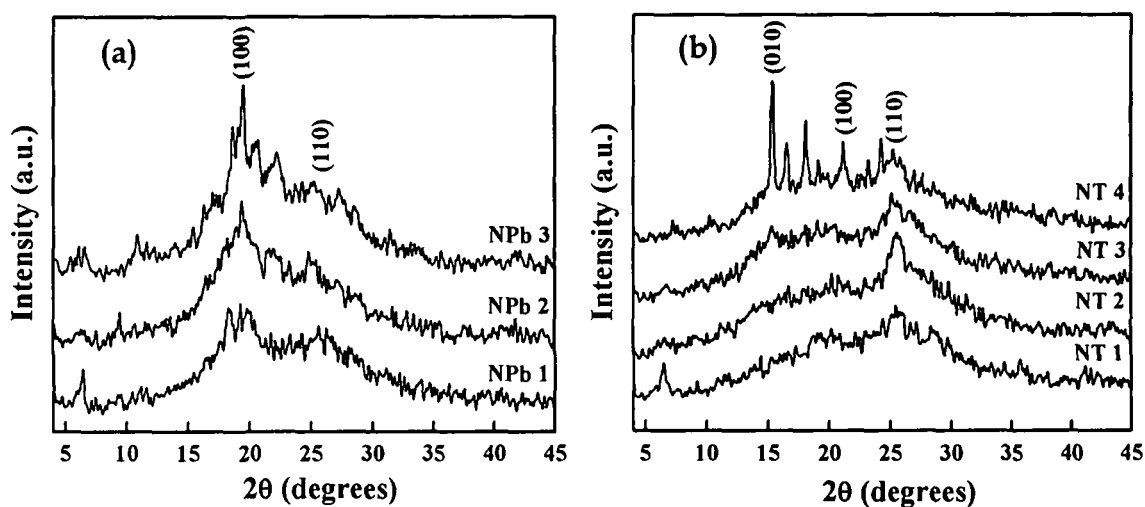


Figure 4.11: X-ray diffraction patterns of (a) DBSA doped PANI nanoparticles and (b) CSA doped PANI nanotubes.

Figures 4.11 (a & b) show the XRD patterns of DBSA doped nanoparticles and CSA doped nanotubes of PANI, respectively. The characteristic peaks of ES-I structure at $2\theta = 20^\circ$ and $2\theta = 25^\circ$ are observed with the CSA doped nanotubes showing the highest crystallinity as compared to all other dopants. Sharp crystalline peaks are observed for the highest doped CSA nanotubes. CSA counterion has C=O group which forms hydrogen bonding with N-H group of PANI leading to ordering of the PANI chains [198]. It is observed in case of the nanotubes, that the periodicity along (110) is greater than that along (100) direction unlike that of the nanofibers, where the periodicity is significant in both the directions. The peak arising due to the periodicity of dopant counterion and N atom is suppressed in the higher doped nanotubes. The bulky size of CSA counterion between the chains restricts the ordering of the counterion and N atom as the number of dopant counterion increases. It is also interesting to note from the Figures 4.10 (b) and 4.11 (a), that for both the HCl doped and DBSA doped nanoparticles, the (100) periodicity is greater than that along (110) direction.

4.3 Vibrational spectroscopic studies

4.3.1 Fourier transform infrared spectroscopy

Figures 4.12 (a & b) represent the FTIR spectra of HCl doped PANI nanofibers and nanoparticles, respectively. In the spectrum of PANI nanofibers, the bands at 1575 and 1494 cm^{-1} are assigned to the C=C stretching vibrations of quinoid ring and benzenoid ring, respectively [199]. The band at 1290 cm^{-1} corresponds to the C-N stretching vibrations of the secondary aromatic amines or displacement of π -electrons induced by doping [200]. The band at 1671 cm^{-1} corresponds to N-H bending vibrations [201]. The band characteristic of protonated form of PANI is observed at 1234 cm^{-1} . This band is attributed to the stretching of C-N⁺ delocalized polaronic structures formed as a result of protonation [202].

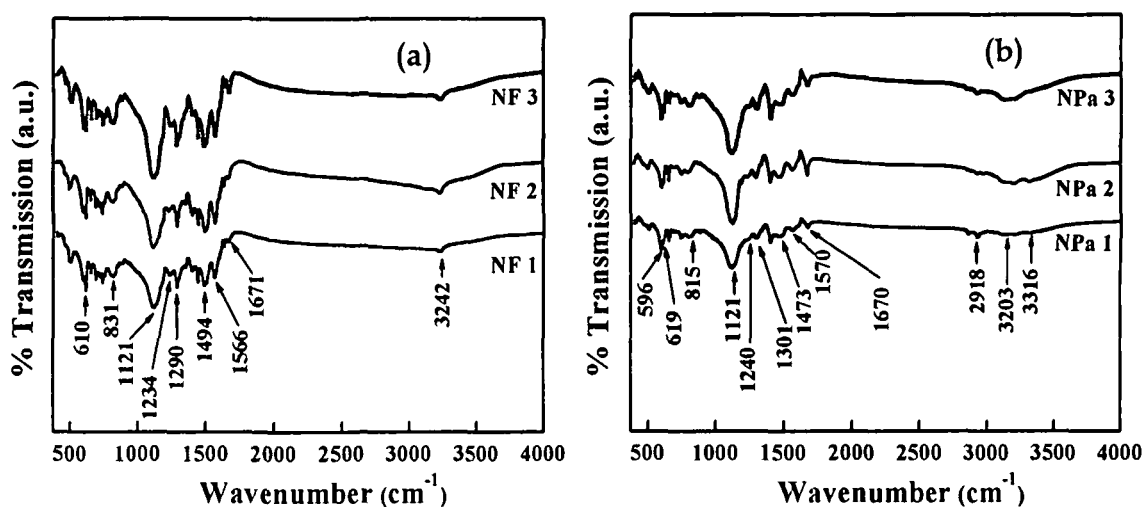


Figure 4.12: FTIR spectra of HCl doped PANI (a) nanofibers and (b) nanoparticles.

Among the peaks, the most intense one is at 1121 cm^{-1} which is attributed to the in-plane bending vibrations of aromatic C-H (mode of N=Q=N, Q=N⁺H-B and B-N⁺H-B; Q=quinoid, B=benzenoid), that occurs during protonation [176]. The intensity of this peak is found to increase with doping level. The weak peak at 831 cm^{-1} is due to the out-of-plane bending modes of

aromatic C–H stretching [203]. The broad band at 3242 cm^{-1} is due to the N–H stretching vibrations [191]. The sharp and strong band at 610 cm^{-1} is attributed to the aromatic ring deformations [191]. In the FTIR spectrum of PANI nanoparticles, in addition to the bands observed in case of nanofibers, an additional band is observed at 2918 cm^{-1} which is ascribed to aliphatic C–H stretching of the SDS molecule. The peak at 596 cm^{-1} due to SO_3^- group [204] of SDS gets merged with the 619 cm^{-1} signature peak of aromatic ring deformation. The C–Cl stretching peak arises in the region $590\text{--}700\text{ cm}^{-1}$ [205]. In both the cases, the intensity of 1234 cm^{-1} peak increases with doping indicating an increase in polarons.

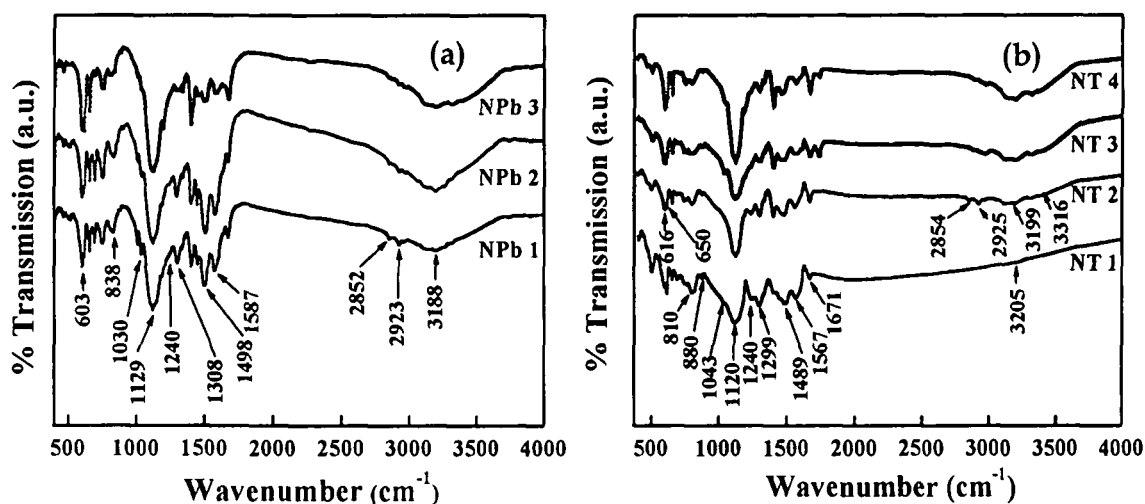


Figure 4.13: FTIR spectra of (a) DBSA doped PANI nanoparticles and (b) CSA doped PANI nanotubes.

Figures 4.13 (a & b) depict the FTIR spectra of DBSA doped nanoparticles and CSA doped nanotubes of PANI, respectively. In addition to characteristic peaks of protonated PANI as discussed above, the peaks corresponding to DBSA and CSA dopant counterions are also observed. The peaks at 2852 cm^{-1} and 2923 cm^{-1} in Figure 4.12 (a) are assigned to the aliphatic C–H stretching mode which depends on the long alkyl chain (tail) of DBSA. The small band at 1030 cm^{-1} corresponds to the S=O stretching mode of SO_3^-

group of DBSA. In Figure 4.13(b), the peaks at 1043 ($\text{NH}^+ \dots \text{SO}_3^-$ interactions), 880 (S–O asymmetric stretching) and 616 cm^{-1} (C–S stretching vibration) reveal the presence of CSA as dopant [206]. The small band at 1240 cm^{-1} corresponding to C–N⁺ stretching increases with doping level for both the DBSA and CSA doped nanostructures. The vibrational frequencies of the major IR bands and their assignments are summarized in Table 4.1.

Table 4.1: Characteristic IR bands of doped PANI and their assignments.

IR bands	Assignments
596 cm^{-1}	SO_3^- bending (SDS) [204]
610 cm^{-1}	Aromatic ring deformations [191]
616 cm^{-1}	C–S stretching (CSA) [206]
831 cm^{-1}	Out-of-plane deformation of C–H in (1,4-disubstituted ring) [203]
880 cm^{-1}	S–O asymmetric stretching (CSA) [206]
$1030 \text{ cm}^{-1}, 1043 \text{ cm}^{-1}$	S=O stretching (DBSA, CSA) [206]
1121 cm^{-1}	Aromatic in-plane C–H bending [176]
1234 cm^{-1}	Delocalized C–N ⁺ stretching [202]
1301 cm^{-1}	C–N stretching of secondary amine of PANI backbone [200]
1494 cm^{-1}	C=C stretching of benzenoid ring [199]
1570 cm^{-1}	C=C stretching of quinoid ring [199]
1671 cm^{-1}	N–H bending [201]
$2852 \text{ cm}^{-1}, 2923 \text{ cm}^{-1}$	Aliphatic C–H stretching [204]
$3199 \text{ cm}^{-1}, 3316 \text{ cm}^{-1}$	N–H stretching [191]

4.3.2 Raman spectroscopy

Raman spectroscopy is an important tool to understand the vibrational modes, which provides information about the structural as well as the protonation state of PANI. Generally, the lower wavenumbers ($100 - 1000 \text{ cm}^{-1}$) is sensitive to the crystalline arrangement and the higher wavenumbers (above 1000 cm^{-1}) is responsible for its protonation and oxidation state [207]. For better analysis, the Raman spectra have been split into two parts – lower wavenumbers ($100 - 1000 \text{ cm}^{-1}$) and higher wavenumbers ($1100 - 1700 \text{ cm}^{-1}$). Figures 4.14 (a & b) represent the Raman spectra of HCl doped PANI nanofibers at lower and higher wavenumbers, respectively. The bands at 115 and 183 cm^{-1} correspond to the ES-I type crystalline arrangement of PANI. These Raman modes are assigned to $C_{\text{ring}}-N-C_{\text{ring}}$ deformations and lattice modes [208]. The intensity of these bands increases with doping which indicates an increasing oxidation of the polymer chains. The modes at about $200 - 500 \text{ cm}^{-1}$ are mainly sensible to the conformational changes of PANI [209]. The peak at 447 cm^{-1} is assigned to the $C_{\text{ring}}-N-C_{\text{ring}}$ torsion angle and its increase with doping indicates a reduction in the torsion angle. The reduction in torsion angle leads to an increase of π -stacking among the PANI chains which favors charge conduction.

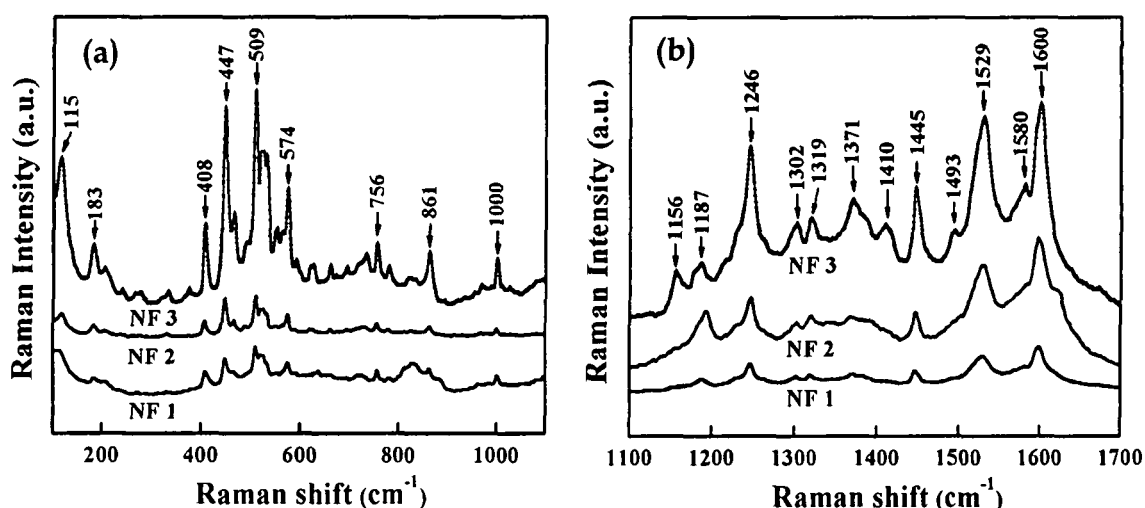


Figure 4.14: Raman spectra of HCl doped PANI nanofibers at (a) low wavenumbers ($100-1000 \text{ cm}^{-1}$) and (b) high wavenumbers ($1100-1700 \text{ cm}^{-1}$).

In the higher wavenumber region, the bands at 1319 and 1370 cm^{-1} are attributed to C–N⁺ vibration of delocalized polaronic structures and vibration of delocalized polarons in the extended polymeric conformation, respectively. Increase in intensity of these two bands with doping signifies an increase of delocalized polarons in the extended PANI chains. The peaks at 1494 cm^{-1} and 1246 cm^{-1} are assigned to C=N stretching vibrations of the quinoid units and C–N stretching vibrations of the benzenoid units, respectively. The increased intensity of the C–N peak than that of the C=N peak is indicative of the fact that the quinoid units are oxidized into benzenoid units during protonation (i.e., doping) and that the carriers are polarons in the present PANI systems. The Raman bands and their assignments obtained in our study are listed in Table 4.2.

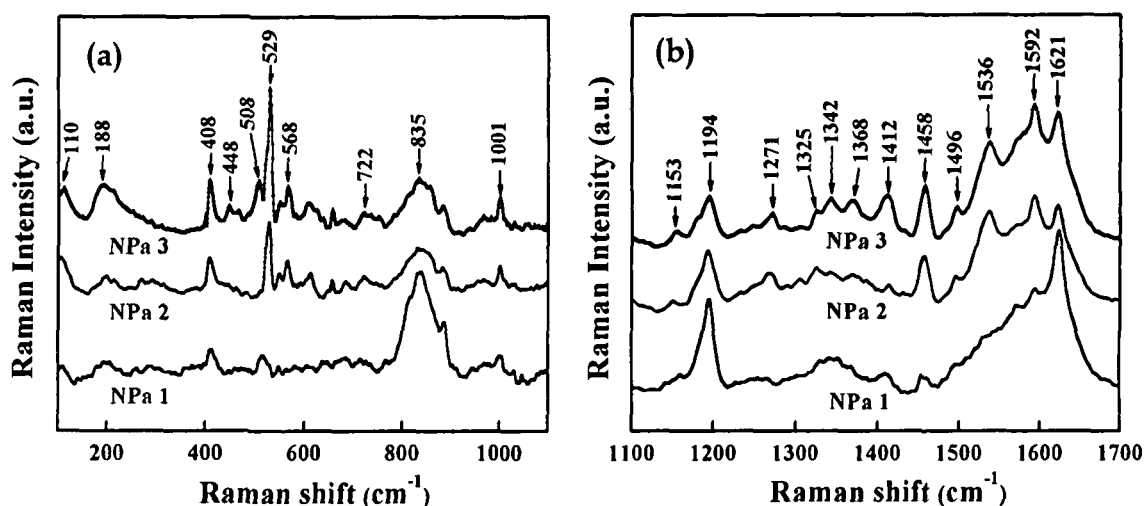


Figure 4.15: Raman spectra of HCl doped PANI nanoparticles at (a) low wavenumbers (100-1000 cm^{-1}) and (b) high wavenumbers (1100-1700 cm^{-1}).

Figures 4.15 (a & b) depict the Raman spectra of HCl doped PANI nanoparticles at lower and higher wavenumbers, respectively. The slight shift in the band positions at lower wavenumbers 110, 188, 448, 529, 568, 722, 835 and 1001 cm^{-1} from that of HCl doped nanofibers indicate differences in structural arrangement of HCl doped PANI nanoparticles. There is a shift in the higher wavenumber side of the characteristic bands corresponding to N–H bending vibrations at 1536 cm^{-1} , C=C stretching vibrations at 1592 cm^{-1} and C–C

stretching vibrations at 1621 cm^{-1} indicating significant conformational changes in the nanoparticles.

Table 4.2: Characteristic Raman bands of doped PANI and their assignments.

Raman bands	Assignments
110-115 cm^{-1} , 183-203 cm^{-1}	$\text{C}_{\text{ring}}\text{-N-C}_{\text{ring}}$ def. and lattice modes [208]
408 cm^{-1} , 447 cm^{-1}	$\text{C}_{\text{ring}}\text{-N-C}_{\text{ring}}$ torsion (o.p.) [209]
509 cm^{-1}	Amine def. (i.p.) [209]
564-574 cm^{-1}	Benzene ring def. (i.p.) [209]
655-756 cm^{-1}	Imine def. (o.p.) [210]
832-861 cm^{-1}	Quinoid ring def. (i.p.) [209]
1000-1001 cm^{-1}	Benzene ring def. (i.p.) [209]
1152-1156 cm^{-1}	C-H bending vibrations of quinoid rings (i.p.) [209]
1187-1194 cm^{-1}	C-H bending vibrations of benzenoid rings (i.p.) [209]
1246-1271 cm^{-1}	C-N stretching vibrations of benzenoid rings (i.p.) [210]
1302 cm^{-1}	Benzene ring def. (i.p.) [209]
1319-1335 cm^{-1}	C-N ⁺ vibration of delocalized polaronic structures [209]
1368-1385 cm^{-1}	Delocalized polarons in extended PANI conformation [209]
1410-1413 cm^{-1}	C-N vibration of tertiary amine on cyclic structures produced by crosslinking of PANI [211]
1445-1458 cm^{-1}	C-C stretching vibrations of quinoid rings (i.p.) [209]
1493-1496 cm^{-1}	C=N stretching vibrations of quinoid rings (i.p.) [209]

1529-1536 cm ⁻¹	N–H bending vibrations of semi quinoid rings (i.p.) [212]
1570-1595 cm ⁻¹	C=C stretching vibrations of quinoid rings (i.p.) [213]
1600-1621 cm ⁻¹	C–C stretching vibrations of benzene rings (i.p.) [212]

The Raman spectra of DBSA doped PANI nanoparticles is shown in Figures 4.16 (a & b) at lower and higher wavenumbers, respectively. The spectra are quite similar to that of HCl doped PANI nanoparticles with a shifting of the band at 1385 cm⁻¹ from 1368 cm⁻¹ which corresponds to the vibration of delocalized polarons on extended PANI chains.

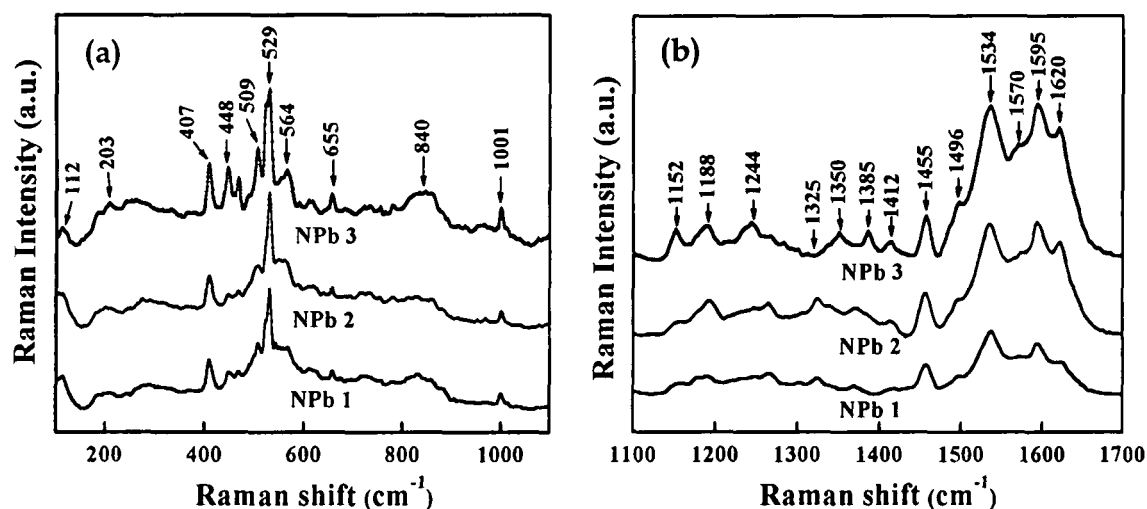


Figure 4.16: Raman spectra of DBSA doped PANI nanoparticles at (a) low wavenumbers (100-1000 cm⁻¹) and (b) high wavenumbers (1100-1700 cm⁻¹).

Figures 4.17 (a & b) represent the Raman spectra of CSA doped PANI nanotubes at lower and higher wavenumbers, respectively. All the characteristic bands of doped PANI are present in the nanotubes. The bands at 1193 and 1621 cm⁻¹ corresponding to C–H bending vibrations and C–C stretching vibrations of benzenoid rings are very intense surpassing the other

bands. It is observed from the spectra of all the nanostructures that the present PANI systems are in the ES-I form and the charge carriers are polarons. The intensity of the band at 1368 and 1319 cm^{-1} corresponding to the delocalized polarons and C-N⁺ vibration, respectively is found to increase with doping for all the nanostructures.

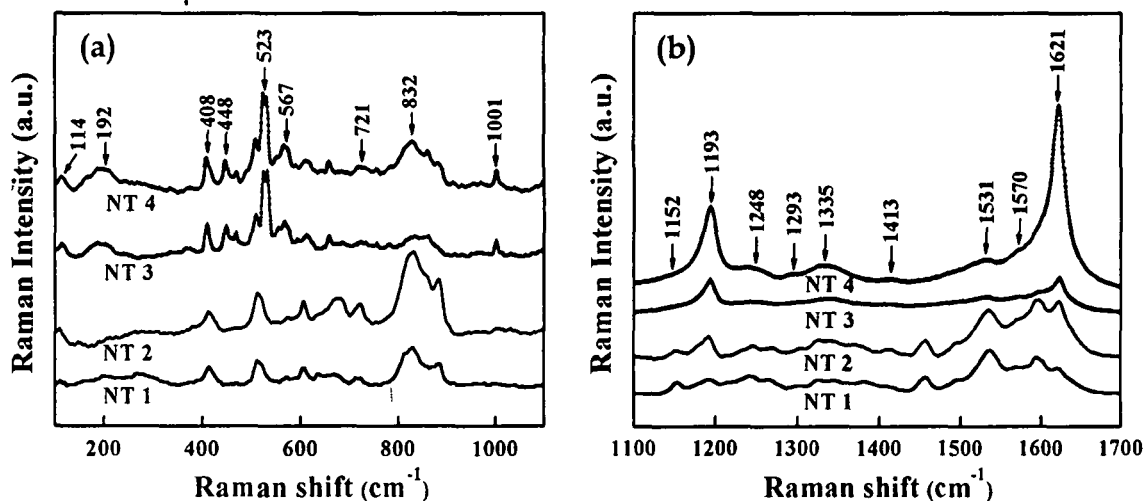


Figure 4.17: Raman spectra of CSA doped PANI nanotubes at (a) low wavenumbers ($100\text{-}1000\text{ cm}^{-1}$) and (b) high wavenumbers ($1100\text{-}1700\text{ cm}^{-1}$).

4.4 Summary

In summary, different nanostructures of PANI, namely, HCl doped nanofibers and nanoparticles, DBSA doped nanoparticles and CSA doped nanotubes have been synthesized by interfacial polymerization and self-assembly methods. High resolution transmission electron micrographs revealed the diameters of the nanostructures. The average diameter of the HCl doped nanofibers and nanoparticles for two different doping levels are found to be 11.5 nm and 3 nm, respectively. The length of the fibers varied from a few nanometers to several micrometers. The diameter of the nanoparticles is determined by the size of surfactant micelle which did not change with doping, as the concentration of the surfactant used for controlling the morphology was kept constant. In

interfacial polymerization, the diameter of the fibers depends on the type of dopant acid used and not on its concentration; hence the diameter of the fibers did not vary. The average size of DBSA doped nanoparticles increases with doping from 6 to 35 nm. The average inner and outer diameters of the CSA doped nanotubes also increase with doping. The inner diameter increases from 38 to 91 nm while the outer diameter increases from 99 to 142 nm with doping. DBSA and CSA being functional dopants i.e., they act both as dopants and structure-directing agents, increasing their concentration leads to the increase in micellar size and hence the increase in diameter.

X-ray diffraction studies indicated the presence of the characteristic peaks of PANI at $2\theta = 20^\circ$ and 25° attributed to the parallel and perpendicular periodicity of the chains, respectively for all the nanostructures. The periodicity is found to increase with doping for the nanostructures. The peak corresponding to dopant counterion at $2\theta = 6.4^\circ$ is found to be much intense in case of the nanofibers indicating that the ordering takes place along the length of the fibers. The absence of this peak in higher doped CSA nanotubes is attributed to the larger size of the counterions that disturbs the ordering. CSA doped nanotubes shows the highest crystallinity which is attributed to the ordering of chains due to the hydrogen bonding between C=O group of CSA and N-H group of PANI chains. The room temperature Fourier transform infrared spectroscopy and Raman spectroscopy reveal polaron as the major charge carrier in the present PANI nanostructures, and an increase in the peak with doping corresponding to delocalized polaronic structures. In Raman spectra, the peak due to $C_{\text{ring}}-N-C_{\text{ring}}$ torsion angle increases with doping indicating a decrease in torsion angle, thereby an increase in π -stacking of the PANI chains. The Raman spectra confirm the formation of ES-I crystalline structure of PANI. With doping, the peak corresponding to C-C stretching increases while that of C=C decreases indicating that the quinoid segments are transformed to benzenoid segments upon protonation and the concentration of benzenoid rings increases with doping.

CHAPTER 5

Electrical transport in polyaniline nanostructures

This chapter deals with the electrical charge transport behavior of different polyaniline nanostructures. The dc conductivity and magnetoresistance studies have been carried out to investigate the charge conduction mechanism in the nanostructures. The mobility of the charge carriers has been determined by the temperature dependent current-voltage characteristics. The temperature and field dependence of mobility have been investigated and analyzed by uncorrelated and correlated Gaussian disorder models. The influence of charge trapping centers in the form of both positional and energetic disorders on the charge transport has been studied in detail.

5.1 Introduction

During the last few decades, there have been extensive investigations to understand the nature of charge transport in π -electron conjugate conducting polymers; however the subject remains far from fully understood and continues to draw attention of the scientific community [214]. The most important characteristic of these materials is that the conductivity can be tuned by several orders of magnitude encompassing the whole range of insulators, semiconductors and metals. Usually, the charge transport mechanism in conducting polymers is very complex and cannot be explained using the concepts of band theory of solids. While the rigorous experiments and fascinating theoretical modeling have been done to gain an insight into the

charge transport phenomena, it is commonly believed that disorder-induced localization governs the charge conduction in this class of materials [215, 216]. The common factors of disorder are partial crystallinity, inhomogeneous doping and synthesis processes. Increasing doping reduces the disorder in conducting polymers, thereby increasing the conductivity which may lead to metal-insulator transition (MIT). The nature of disorder, homogeneous or inhomogeneous, is the determining factor of the charge transport mechanism. The homogeneous disorder induced MIT can be explained by the three-dimensional localization-interaction model for transport in disordered metals on the metallic side of the MIT [110, 47]. On the insulating side of MIT, the charge transport can be understood in terms of variable-range hopping among randomly localized states [38]. In case of inhomogeneous disorder, however, the polymer consists of small crystalline domains surrounded by amorphous domains and the MIT is better described in terms of percolation between metallic islands (i.e., crystalline domains)[82, 217]. In recent years, the progress in processing of conducting polymers has substantially improved the material quality by reducing the extent of disorder with a corresponding increase in electrical conductivity. The extent of disorder is reduced in such a way that the correlation length (on the metallic side) or the localization length (on the insulating side), which characterizes the extent of electronic wavefunctions, becomes greater than the crystalline coherence length. In such a case, the disorder can be regarded as homogeneous, since there is considerable overlapping of wavefunctions of the delocalized states [16].

Externally applied magnetic field has profound effect on the charge transport of conducting polymers. For instance, in metallic region near the MIT; the application of field can shift the mobility edge separating the localized and extended states, inducing a crossover to insulating state [137]. On the other hand, in the insulating regime, application of isothermal magnetic field can either lead to an increase in resistance (positive magnetoresistance) or a decrease in resistance (negative magnetoresistance) [138]. In disordered

hopping systems, the positive magnetoresistance is generally ascribed to shrinkage in the overlap of wavefunctions [34] and the negative magnetoresistance is attributed to quantum interference effect of hopping paths [140, 142].

Conducting polymers are widely used in many electronic and optoelectronic devices such as organic light emitting diodes (OLEDs) [218], organic solar cells [219] and field-effect transistors (FETs) [220]. Since, the charge transport in these devices occurs through variable-range hopping mechanism among localized electronic states, the charge mobility and its trapping play a crucial role in controlling the performance of these polymer devices. In these conjugated polymer systems, both the energetic and the positional disorder can act as charge trapping centers; hence their presence naturally leads to a decrease in mobility of the carriers. Therefore, it is very important to understand the nature of disorder as well as its effect on the charge transport in these highly disordered polymer materials. Several techniques have been employed to determine the carrier mobility such as time-of-flight (ToF) [221], dark injection transient current method [222] and temperature dependent current (I) - voltage (V) measurements [223]. Among these, temperature dependent I - V measurement technique is the most commonly used method to investigate the charge mobility because of its apparent experimental and theoretical simplicity.

It is also an established fact that the conduction in organic devices depends greatly on the metal-polymer barrier height which plays a vital role in the overall transport of carriers. There are mainly two limiting regimes of conduction, namely, the injection-limited conduction (ILC) and space-charge-limited conduction (SCLC), where the latter is mostly controlled by the bulk properties of the material [224]. When the barrier height is large, charge carriers can either jump over or tunnel through the barrier to the localized states under the application of voltage leading to injection-limited current. However, in case of small barrier height (usually < 0.3 eV), the carriers can

easily cross the barrier, hence creating a space-charge region leading to SCLC. In this scenario, the SCLC method is commonly employed for the determination of mobility and several other physical parameters like disorder parameters, inter-site distance and localization length that describes the polymer.

In this chapter, an attempt has been done to understand the charge transport behavior of different polyaniline (PANI) nanostructures, namely, hydrochloric acid (HCl) doped nanofibers (NF) and nanoparticles (NPa), dodecyl benzene sulfonic acid (DBSA) doped nanoparticles (NPb) and camphor sulfonic acid (CSA) doped nanotubes (NT) with varying temperature as well as magnetic field. The samples were prepared with increasing doping level. The details of sample preparation and description have been discussed in section 3.2 of Chapter 3. The samples are numbered accordingly in ascending order of doping level. We consider PANI among the family of conducting polymers owing to its various advantageous properties and consequent promising technological applications (discussed in section 1.4 of Chapter 1). The temperature dependent I - V characteristics were also measured to determine the mobility and to study the influence of charge trapping centers on charge conduction. The nanostructured polymers are much more complex systems compared to their bulk counterparts and the charge transport in these materials are very much affected by the quantum size-effects. Although there are several reports on electrical conductivity and the effect of magnetic field in PANI nanotubes [88, 225], extensive investigation of temperature and magnetic field dependence of charge conduction of different PANI nanostructures doped with different dopants have not been made earlier. Besides, the nature of charge trapping centers i.e., disorder and its effect on the mobility of the carriers in nanostructured devices is not well understood with only a few reports on bulk PANI materials [226-228].

In this chapter, a sincere effort is made for a better understanding of the nature of charge transport and effect of traps on mobility in the PANI nanostructures, which extensively depend on the dopant counterions and

morphology of the nanostructures. DC conductivity studies in the temperature range of 5 - 300 K have been performed on all the nanostructures. The nanostructures exhibit a metal-insulator transition at about ~ 20 K as the temperature is increased. We find that the metallic behavior arises due to electron-electron interaction effects, while in the insulating regime the conduction mechanism is found to be different for all the nanostructures which depends on the dopant type and morphology. Isothermal magnetoresistance at five different temperatures in the magnetic field range of 0 - 8 T shows a transition above around 100 K from positive to negative magnetoresistance as the temperature is increased, which is qualitatively explained with the bipolaron model. The I - V characteristics of all the nanostructures have been studied in a wide temperature range of 80 - 300 K, in order to study the effect of large concentration of traps present in the bulk of the material on the charge transport, and hence on the mobility of the carriers. Our results display space-charge-limited conduction for all the doped nanostructures. The field and temperature dependence of mobility exhibit the universal Poole-Frenkel behavior. Moreover, analysis of our data with the Gaussian disorder model in the uncorrelated and correlated limit enables us to estimate various disorder parameters and inter-site distance, which are quite interesting.

5.2 DC conductivity studies

The temperature (T) dependence of dc conductivity (σ) of HCl doped PANI nanofibers and nanoparticles at different doping levels are plotted in Figures 5.1 (a & b), respectively in log-log scale. It is observed for both the nanostructures, that the conductivity increases with doping level. For the nanofiber samples, the conductivity increases by an order with doping from 0.09 to 0.15 S/cm at 300 K and 4.71×10^{-7} to 3.35×10^{-6} S/cm at 15 K. However, for the nanoparticles, the conductivity in the highest doped sample increases by about an order of magnitude from 0.07 to 0.4 S/cm at 300 K and by about two orders from 2×10^{-6} to 4×10^{-4} S/cm at 15 K. It is also to be noted that the

conductivity of the nanoparticles is slightly greater than that of the nanofibers. The increase in conductivity of the nanoparticles in spite of using the same amount of HCl dopant makes it clear that sodium dodecyl sulfate (SDS) used as surfactant might also dope the polymer contributing to the conductivity, as reported by Arenas et al. [229], where HCl-SDS binary dopant was used to dope PANI nanofibers. We do not consider the bulk effect of SDS as it was washed away during the purification process, and some remains can only dope the chains affecting the conduction minimally. Besides, SDS is not an efficient dopant [230].

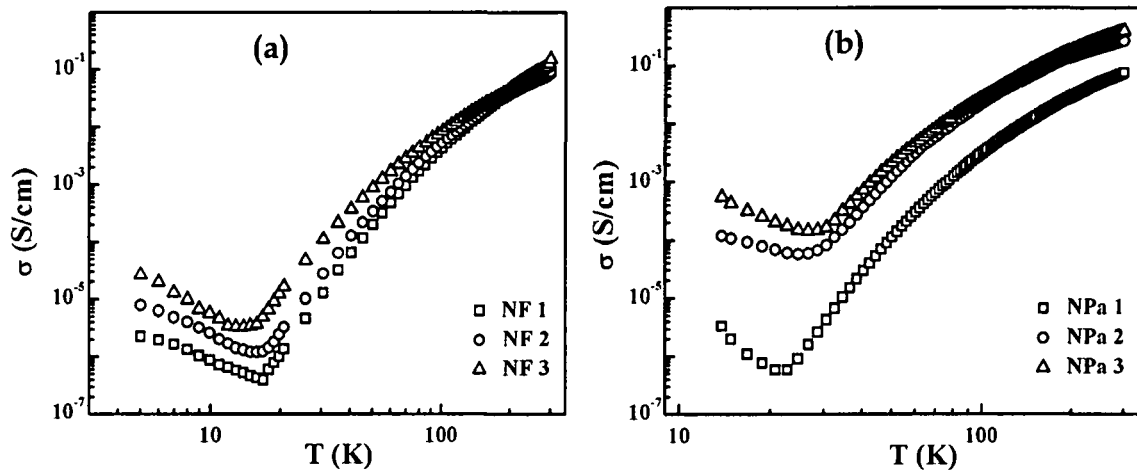


Figure 5.1: Temperature dependence of conductivity for HCl doped PANI (a) nanofibers and (b) nanoparticles.

Figures 5.2 (a & b) represent the log-log plots of T -dependence of conductivity of DBSA doped PANI nanoparticles and CSA doped PANI nanotubes, respectively. The data for the DBSA doped samples could not be collected at lower temperatures due to the high resistance of the samples. The conductivity of the nanoparticles increases by an order with doping from 4.52×10^{-2} to 1.28×10^{-3} S/cm at 300 K. For the CSA doped nanotubes, the increase in conductivity is by about 4 orders of magnitude from 5×10^{-4} to 2.5 S/cm at 300 K. The low-temperature data for the lowest doped nanotube sample could not be collected because of high resistance of the sample. In the low- T side at

~ 20 K, a dip in the conductivity curve is observed for all the nanostructures (except the DBSA doped nanoparticles, data are lacking) i.e., a transition from metallic to insulating (MIT) behavior occurs as the temperature is increased. This metallic behavior at sufficiently low temperatures is due to electron-electron interaction effects explained later in this section.

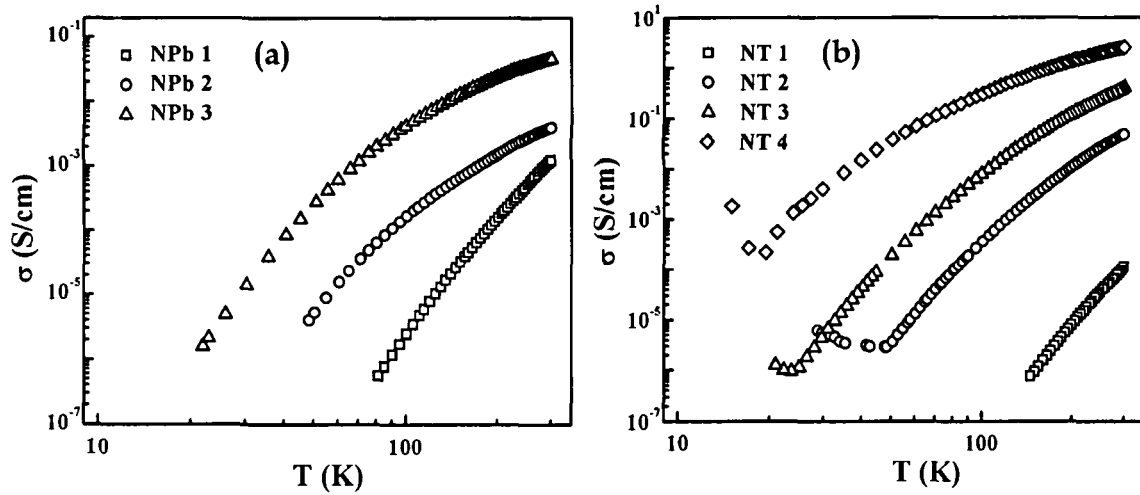


Figure 5.2: Temperature variation of conductivity for (a) DBSA doped PANI nanoparticles and (b) CSA doped PANI nanotubes.

The temperature dependence of dc conductivity in the insulating regime is generally described by the variable-range hopping (VRH) model, where the conduction occurs through thermally activated hopping among the localized states [38]. Following the VRH, the conductivity is expressed as:

$$\sigma(T) = \sigma_0 \exp\left(-\frac{T_0}{T}\right)^n \quad (5.1)$$

where T_0 is the characteristic temperature and n is a parameter which depends on the type of conduction mechanism. The value n can be determined from the plot of the reduced activation energy:

$$W = \frac{d(\ln\sigma)}{d(\ln T)} \quad (5.2)$$

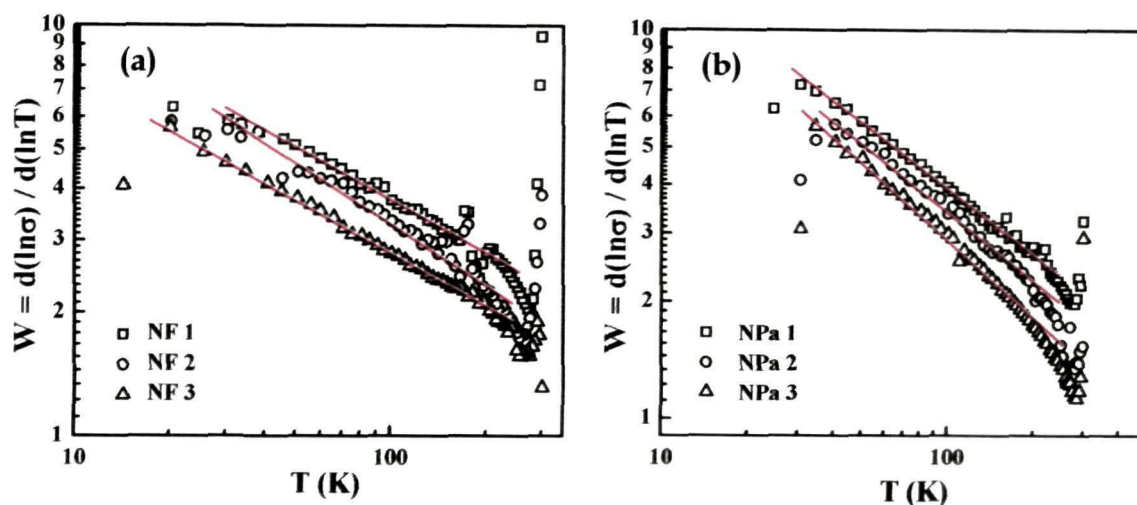


Figure 5.3: Plots of W vs. T for HCl doped PANI (a) nanofibers and (b) nanoparticles.

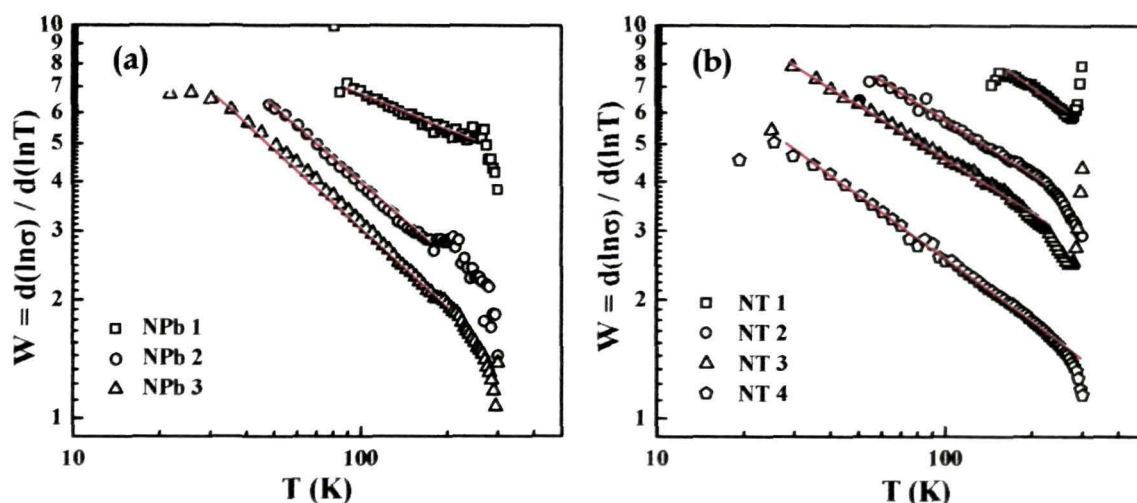


Figure 5.4: W vs. T plots of (a) DBSA doped PANI nanoparticles and (b) CSA doped PANI nanotubes.

The log-log plots of W vs. T of HCl doped PANI nanofibers and nanoparticles are shown in Figures 5.3 (a & b), respectively. The slope of the curve i.e., the value of n is in the range of 0.42 - 0.44 for the nanofibers, and 0.60 - 0.64 for the nanoparticles. W vs. T (log-log) plots for the DBSA doped nanoparticles and CSA doped nanotubes are respectively shown in Figures 5.4 (a & b). The value of n for the DBSA doped nanoparticles comes out to be in the

range of 0.62 - 0.67, while that for the nanotube samples in the insulating regime is found to be in the range of 0.48 - 0.52. This value of n for the nanotubes is close to the Mott's VRH for quasi one-dimensional hopping where $n = 0.5$.

The values of n for the nanofibers and nanoparticles indicate that the conduction mechanism is different from the conventional Mott VRH [231], where the maximum value of n without Coulomb interaction is 0.5. For the Mott VRH, $n = 1/(1+s)$, where $s = 1, 2$ and 3 is the dimension. The conduction in the nanoparticles and the nanofibers occurs by VRH of charge carriers among superlocalized states with and without Coulomb interaction, respectively as observed in fractals [36]. Fractals are self similar i.e., same at almost every length scales. The transport and diffusion in porous disordered medium are often modeled by random walks over fractal structures. A random walk in space itself builds a fractal medium selecting sites according to certain probability rules [232]. The anomalous nature of diffusion in fractal medium leads to superlocalization of electrons. In contrast to Anderson decay law of electronic wavefunctions: $\psi(r) \propto \exp[-r/L_c]$, the wavefunctions of electrons localized on fractals decay more rapidly as: $\psi(r) \propto \exp\left[-\left(r/L_c\right)^\xi\right]$, where L_c is the localization length, $\xi > 1$ is the superlocalization exponent which depends on the Euclidean dimensionality of the system [36]. As a result, the microscopic charge transfer rates on fractals are significantly lower than that of systems with Euclidean dimensionality resulting in a substantial increase in resistance and slowing down of various kinetic processes. Deutscher et al. [104] have predicted that for charge transport by VRH among superlocalized states, $n = \xi/(\xi+d_f) \approx 3/7$ (or 0.43), where d_f is the fractal dimension. Later, Van der Putten et al. [37] generalized the VRH theory among superlocalized states with Coulomb interactions and obtained $n = \xi/(\xi+1) \approx 0.66$. For the present systems, ξ comes out to be ~ 1.77 and d_f is found to be 2.25 in three-dimensional Euclidean space.

The discrepancy observed in the conduction mechanism of the nanostructures might depend on the dopant counterion and the morphology. CSA anion being larger in size aligns the polymer chains and restricts the charge motion to only one direction. The bulky CSA anion fills up the porous polymer creating a Euclidean space for charge transfer. On the other hand, Cl^- ion being very small cannot align the polymer chains making the polymer porous and forcing the geometric dimension of the current path to take fractional values. Similarly, DBSA doped nanoparticles also exhibit fractal conduction. Although, DBSA is a large molecule, it does not have bulky cycloaliphatic rings as in CSA. The long alkyl chain (tail) of DBSA anion in between the chains makes the polymer porous leading to fractal-like conduction.

The fractality arises due to the random distribution of polymer chains connected by inter-chain links [233]. The fractal nature has earlier been observed in conductive blends and composites of PANI forming a percolating cluster [234, 235]. However, fractality in pure PANI has not been observed, although some theoretical studies predicted one-dimensional fractal nature of conducting paths in conducting polymers [236]. In addition, it is also observed from the structural analysis in section 4.2.2 of Chapter 4 that CSA doped nanostructures are more crystalline resulting in better conduction than that of the other doped nanostructures. CSA counterion has C=O group which forms hydrogen bonding with N-H group of PANI leading to ordering of PANI [198]. Hence, the conduction is quasi one-dimensional with weak inter-chain interactions. The small size of Cl^- ion cannot form ordered chains leading to random alignment of chains and hence amorphicity. The lowest conductivity is observed for the DBSA doped nanostructures which might be attributed to the larger inter-chain spacing due to the long alkyl chains leading to reduced inter-chain charge transfer. The schematic of doping and formation of aligned chains with dopant counterions are shown in Figure 5.5.

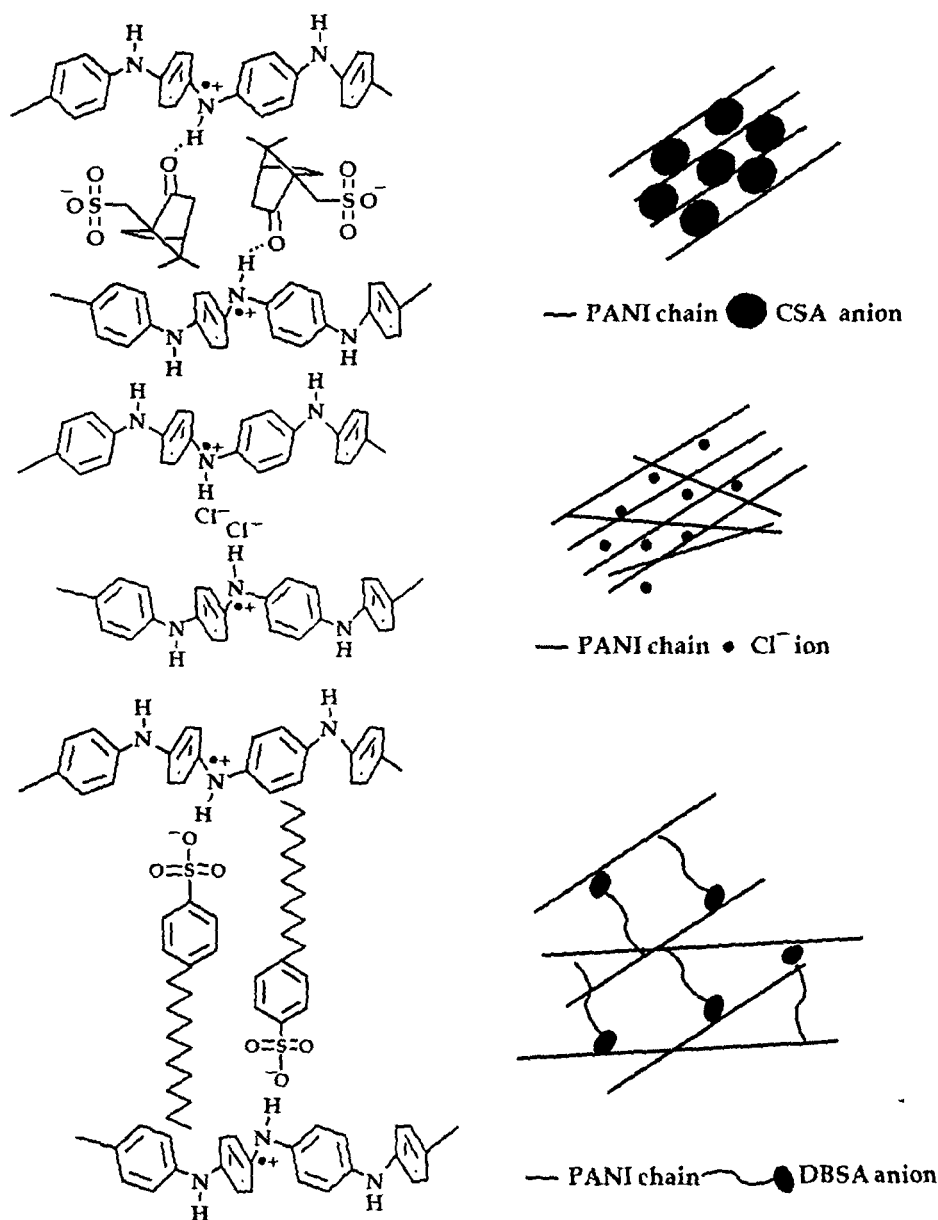
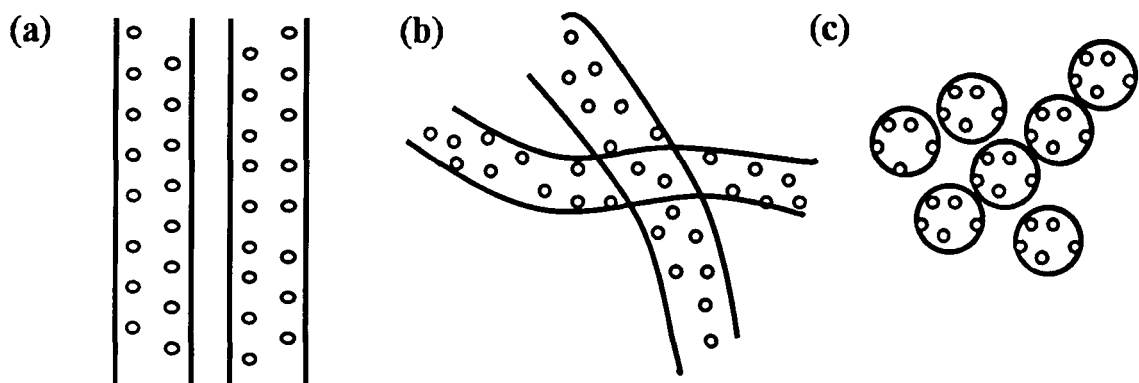


Figure 5.5: Two dimensional schematic representations of dopant counterions in between PANI chains. The hydrogen bonding between C=O group of CSA ion and N-H group of PANI is also shown.

Coulomb interactions between the outgoing electron and the remaining hole come into play in case of the nanoparticles owing to the small size and confinement along all the dimensions. This intriguing feature is not observed in case of the nanofibers or nanotubes. The present theoretical knowledge at hand cannot explain this interesting observation. Our preliminary understanding

suggests that this may arise due to the extended spatial dimension of the nanofibers and nanotubes. Due to the extended dimension, an electron has greater probability to jump to further distance reducing the separation between the electron-hole pair, eventually reducing the interaction. Nonetheless, this interesting feature requires further detailed experimental investigations with particles of different size and variation of dopant types. The present theoretical understanding should also be extended to understand this exciting phenomenon.



◦ **Charge hopping site**

Figure 5.6: Schematic illustrations of (a) Well aligned polymer chains with charge hopping sites inside the CSA doped nanotubes, (b) & (c) Random distribution of hopping sites within the chains inside the nanofibers and the nanoparticles, respectively.

Comparing NF 2, NPa 2, NPb 2 and NT 4 samples, as they contain the same molar concentration of dopant, it is observed that the conductivity value has the following relation $NT\ 4 > NPa\ 2 > NF\ 2 > NPb\ 2$ i.e., the CSA doped PANI has the highest conductivity while DBSA doped has the lowest conductivity. CSA forms the most ordered structures helping in conduction while DBSA increases the inter-chain spacing reducing the macroscopic conductivity. The schematic of hopping sites in the aligned chains of the nanotubes and the randomly distributed hopping sites within the chains of the nanofibers and the nanoparticles are shown in Figure 5.6.

For one-dimensional Mott VRH, the characteristic temperature T_0 is given by [237]:

$$T_0 = \frac{16}{k_B N(E_F) L_c z} \quad (5.3)$$

where z is the number of nearest neighbor chains (~ 4), k_B is the Boltzmann constant and $N(E_F)$ is the DOS at the Fermi level. The average hopping length for one-dimensional Mott VRH is given by [237],

$$R_{hop} = \left[\frac{L_c}{\pi k_B T N(E_F)} \right]^{1/2} \quad (5.4)$$

Assuming one-dimensional Mott VRH conduction for the CSA doped nanotubes, we have plotted $\ln \sigma$ vs. $T^{-1/2}$ for all the nanotube samples as shown in Figure 5.7. A straight line is obtained, in agreement with Eq. (5.1), which suggests that the dc conductivity of the samples in the insulating regime follows Mott's one-dimensional VRH model. The values of the parameters T_0 and σ_0 are obtained from the slope and the intercept of the plots, respectively.

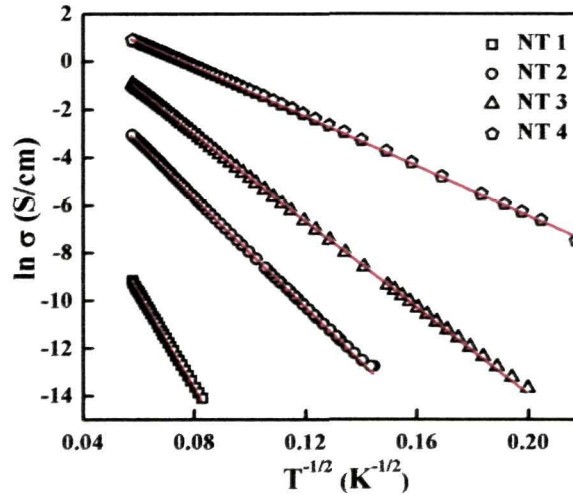


Figure 5.7: $\ln \sigma$ vs. $T^{-1/2}$ plot of the insulating regime (solid symbol) and fits of

$$\sigma(T) = \sigma_0 \exp\left(-\frac{T_0}{T}\right)^{1/2} \quad (\text{line}) \text{ for CSA doped PANI nanotubes.}$$

The values of T_0 for the HCl doped nanofibers have been obtained by plotting $\ln\sigma$ vs. $T^{-3/7}$ in Figure 5.8, and that of the HCl and DBSA doped nanoparticles are obtained by plotting $\ln\sigma$ vs. $T^{-0.66}$ in Figures 5.9 (a & b), respectively. The obtained values of T_0 are very small which indicate that the disorder is sufficiently reduced in the presently synthesized PANI nanostructure systems. Earlier reports reveal high values of T_0 of the order of $\sim 10^4$ K, indicating the presence of strong disorder in the systems [88, 238]. The reduction in disorder is attributed to the control of synthesis at nanolevel which increases the quality of the material [93].

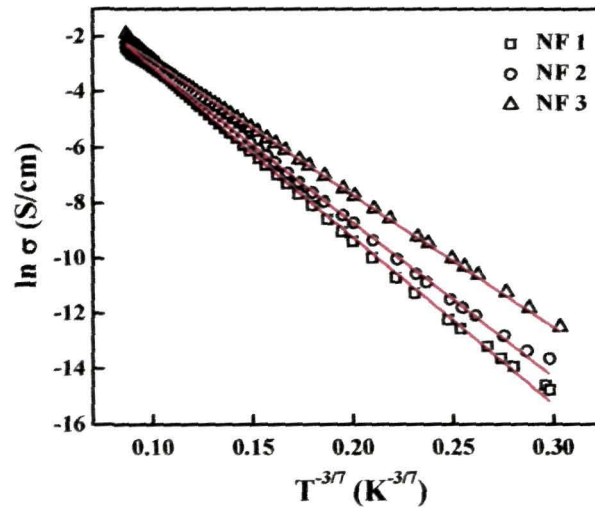


Figure 5.8: $\ln\sigma$ vs. $T^{-3/7}$ plot of the insulating regime (solid symbol) and fits of

$$\sigma(T) = \sigma_0 \exp\left(-\frac{T_0}{T}\right)^{3/7} \quad (\text{line}) \quad \text{for HCl doped PANI nanofibers.}$$

Using a typical value of $N(E_F) = 9 \times 10^7 \text{ eV}^{-1} \text{ cm}^{-1}$ [237], the localization length and hopping energy of CSA doped nanotubes have been calculated and given in Table 5.1. To determine the localization length and hopping distance of the nanofibers and the nanoparticles, we use the generalized VRH model for superlocalized states given by Van der Putten et al. [37]. According to this model, the characteristic energy corresponding to the temperature T_0 is given by:

$$k_B T_0 = \left[\frac{(k+1)c}{B'V_L} \right]^{\frac{1}{k+1}} n^{-1} (1-n)^{1-\frac{1}{n}} \quad (5.5)$$

where $V_L (=Lc^3)$ is the volume of a localized state, k and B' are the parameters related to DOS, as $N(E) = B'|E|^k$, and c is a constant. The hopping distance R_{hop} is given as:

$$\left(\frac{R_{hop}}{L_c} \right)^\xi = (1-n) \left(\frac{T_0}{T} \right)^n \quad (5.6)$$

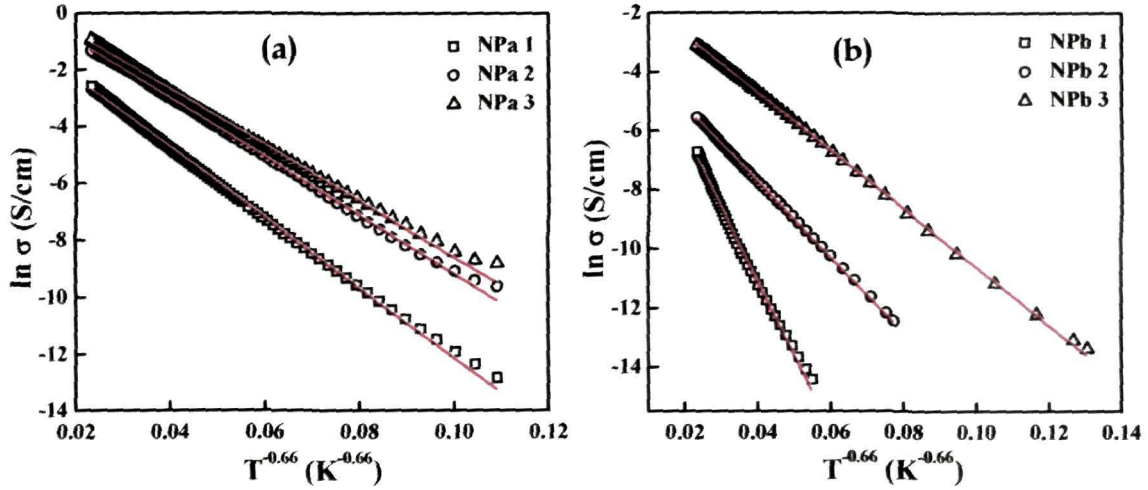


Figure 5.9: $\ln \sigma$ vs. $T^{-0.66}$ plots of the insulating regime (solid symbol) and fits of $\sigma(T) = \sigma_0 \exp\left(-\frac{T_0}{T}\right)^{0.66}$ (line) for (a) HCl and (b) DBSA doped PANI nanoparticles.

For VRH in a fractal network with $n = 3/7$, the DOS is flat i.e., $k = 0$, so that $N(E) = B$, and the superlocalization exponent $\xi = 1.43$ and 1.9 in two- and three- dimensions, respectively. Considering the value of DOS at Fermi level, we have $B = 2.5 \times 10^{19} \text{ cm}^{-3} \text{ eV}^{-2}$ [239] for PANI. Inserting $c = 1$, $k = 0$, $n = 3/7$, $\xi = 1.9$ and the obtained values of T_0 in Eqs. (5.5 & 5.6), L_c and R_{hop} of HCl doped PANI nanofibers are calculated. If the Coulomb interactions between the charge carriers are dominant, a pseudo gap is induced in the DOS. This gap is similar to the Coulomb gap which occurs in the Efros–Shklovskii model for VRH in

exponential localized states. Under the effect of Coulomb interactions, the modified form of Eq. (5.5) for localization length is given as,

$$k_B T_0 = \left(\frac{e^2}{4\pi\epsilon_0\epsilon_r L_c} \right) n^{-1} (1-n)^{1-1/n} \quad (5.7)$$

Table 5.1: Parameters calculated from dc conductivity vs. temperature data in the insulating regime of PANI nanotubes, nanofibers and nanoparticles.

Sample	T_0 (K)	L_c (nm)	* R_{hop} (nm)
CSA doped nanotubes			
NT 1	197	26.15	5.98
NT 2	115	44.85	7.83
NT 3	90	56.83	8.81
NT 4	51	99.62	11.67
HCl doped nanofibers			
NF 1	66	32.49	17.17
NF 2	55	34.56	17.51
NF 3	47	36.43	17.81
HCl doped nanoparticles			
NPa 1	121	66.09	27.83
NPa 2	103	77.62	30.95
NPa 3	99	80.60	31.73
DBSA doped nanoparticles			
NPb 1	246	35.69	19.15
NPb 2	127	69.31	29.67
NPb 3	97	90.07	35.27

* R_{hop} values are calculated at 300 K.

Using $n = 0.66$, $\epsilon_r = 5.5$ and the experimentally obtained values of T_0 in Eqs. (5.6 & 5.7), the values of L_c and R_{hop} of the PANI nanoparticles are

calculated. The values of T_0 , L_c , and R_{hop} for all the nanostructures are given in Table 5.1. The localization length and hopping length increase with doping for all the nanostructures. The obtained localization length values are a few hundreds of angstroms whereas typical value ranges in between some tens of angstroms. This might be due to the reduced disorder in the present set of samples also indicated by the lower values of T_0 .

In the metallic regime, the localization-interaction model can explain the conductivity data. The conductivity expression for this model is given as,

$$\sigma(T) = \sigma(0) + mT^{1/2} + BT^{p/2} \quad (5.8)$$

where the second term arises from electron-electron interactions [47] and the third term is the correction due to localization effects [47]. The details of this model are described in section 2.1.1.4 of Chapter 2.

At temperatures below ~ 20 K, all the samples show a sharp upturn in the conductivity indicating a transition to metallic region. At such low temperatures, the electron-electron interaction effect surpasses the weak localization effects. Similar increase in conductivity has also been reported for PF_6 doped polypyrrole [215, 240] and ion implanted polyaniline films [241]. This has been attributed to the electron-electron interaction effects which modifies the DOS and introduces a conductivity term varying as $T^{1/2}$ at sufficiently low temperatures, as can be seen from Eq. (5.8). The electron-electron interaction effect has two competing contributions – the exchange processes and the Hartree processes. The upturn in conductivity is observed basically due to the dominance of the Hartree processes while the exchange contribution leads to a downturn in conductivity. In the Hartree processes, the mean-free path of electrons increases as a result of elastic scattering, thereby increasing the conductivity [242]. The magnitude of this term is given as:

$$\sigma(T) = 0.915 \frac{e^2}{4\pi^2 \hbar} \left(\frac{4}{3} - \frac{3\tilde{F}}{2} \right) \left(\frac{k_B T}{\hbar D} \right)^{1/2} \quad (5.9)$$

where D is the electronic diffusion coefficient and \tilde{F} is the Hartree coupling strength parameter. The first term represents the exchange processes and the second term represents the Hartree processes. The upturn in conductivity indicating the dominant contribution of Hartree processes, physically mean that the screening radius is small compared to the Fermi-wavelength of the electrons.

5.3 Magnetoresistance studies

Magnetoresistance (MR) is a phenomenon where the resistivity of a material modifies upon application of magnetic field, and is defined as: $MR = \Delta\rho(H)/\rho(0) = [\rho(H) - \rho(0)]/\rho(0)$. The MR has been calculated from the isothermal resistance data $\rho(H)$ collected in field upto 8 T at selective temperatures of 30 K, 50 K, 100 K, 200 K and 300 K. Figures 5.10 (a & b) show the field dependent MR at different temperatures for the HCl doped PANI nanofibers and nanoparticles, respectively. The important observation is that at low temperatures for all the samples, the MR is positive and increases with magnetic field following a non-linear behavior. Interestingly, with increase in temperature, both the magnitude as well as the non-linearity in $MR(H)$ decreases and at temperatures above 100 K, the MR value changes its sign. With further increase in temperature, the data shows that the magnitude of MR increases towards negative direction. For a better visualization, we have plotted the temperature variation of MR value at 8 T for all the nanofiber and nanoparticle samples in Figures 5.11 (a & b). The effect of doping is evident, as it can be seen in the figure that with increasing doping, the positive MR at low temperatures decreases. We also find that the crossover temperature from positive to negative MR decreases and the negative MR at high temperatures increases with doping.

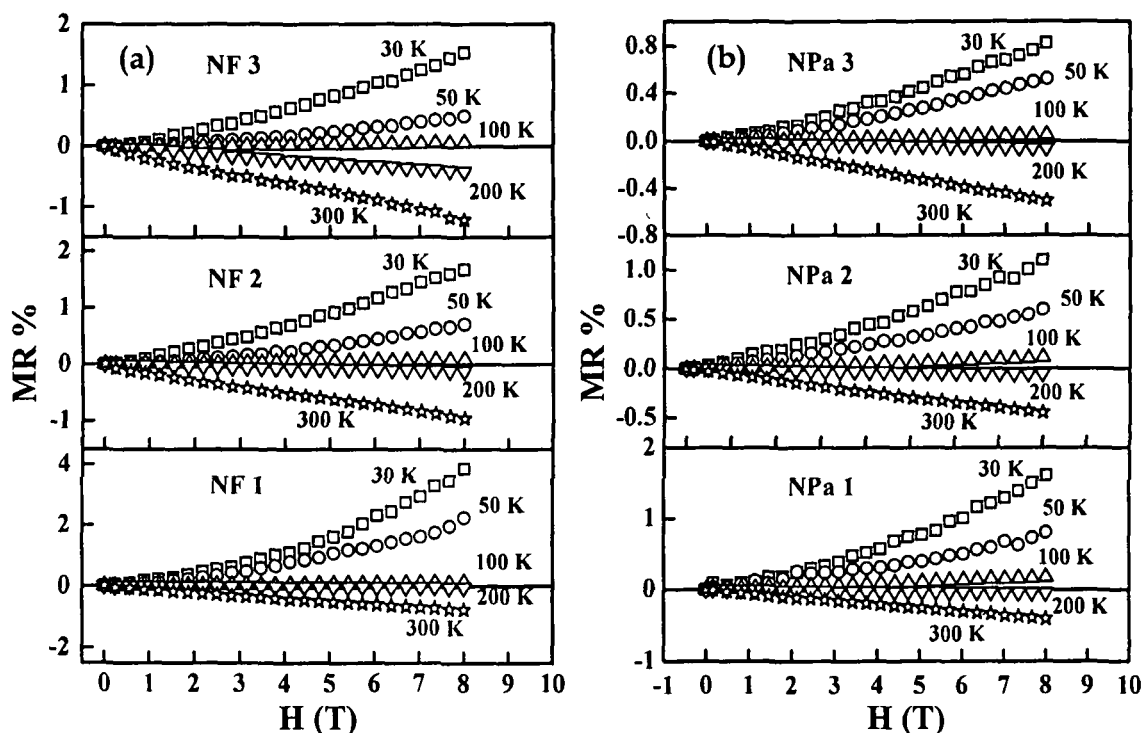


Figure 5.10: MR% of HCl doped PANI (a) nanofibers and (b) nanoparticles at five different temperatures.

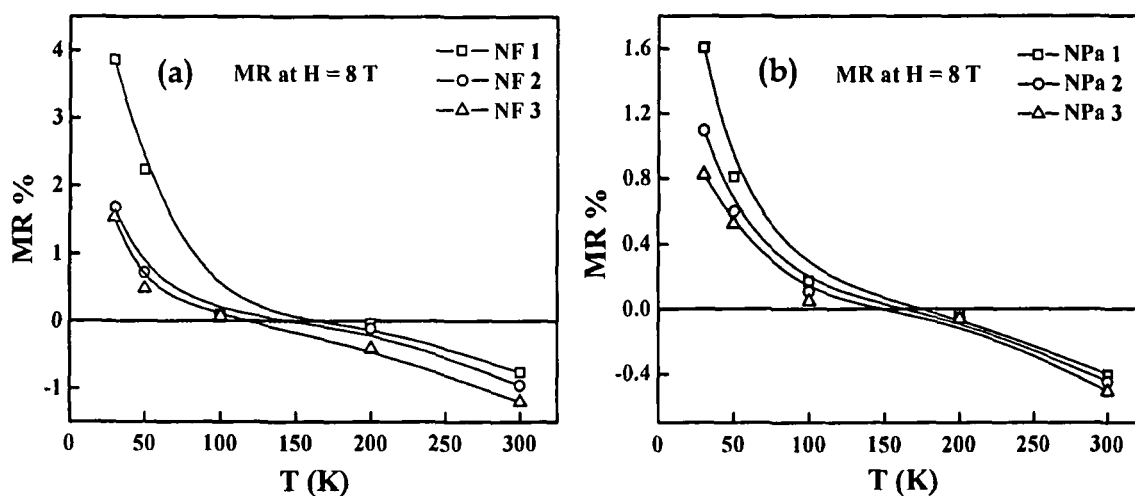


Figure 5.11: Temperature dependence of MR% (at $H=8$ T) for HCl doped PANI (a) nanofibers and (b) nanoparticles.

Figures 5.12 (a & b) represent the field dependent MR of DBSA doped PANI nanoparticles and CSA doped PANI nanotubes, respectively at four different temperatures, viz., 50 K, 100 K, 200 K and 300 K. Similar to the HCl doped nanostructures shown earlier, the MR changes its sign from positive to negative above 100 K. MR% vs. T plots provide a better visualization of the

doping level variation. Figures 5.13 (a & b) show the $MR\%$ (at $H=8\text{ T}$) vs. T plots of DBSA doped nanoparticles and CSA doped nanotubes, respectively. It is observed that the positive MR decreases and negative MR increases with doping for both the DBSA doped nanoparticles and CSA doped nanotubes similar to that observed for the HCl doped nanostructures.

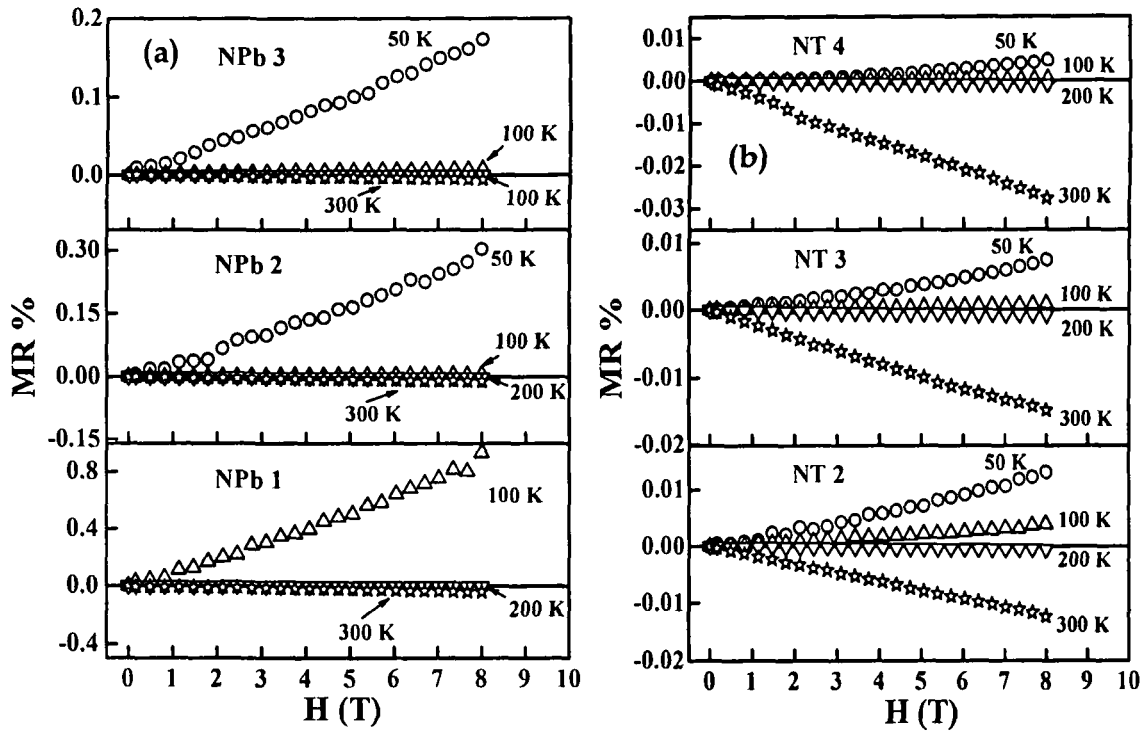


Figure 5.12: $MR\%$ of (a) DBSA doped PANI nanoparticles and (b) CSA doped PANI nanotubes at four different temperatures.

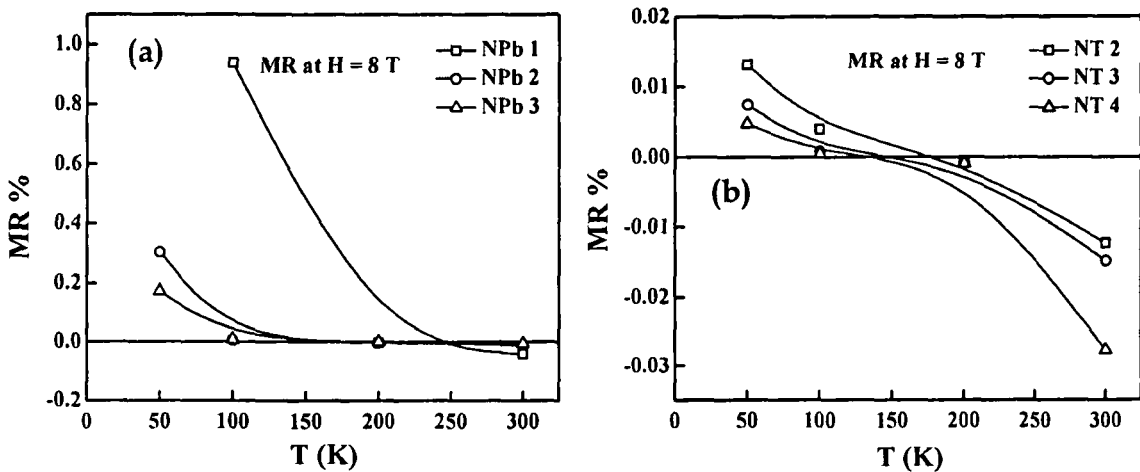


Figure 5.13: $MR\%$ (at $H= 8\text{ T}$) as a function of temperature for (a) DBSA doped PANI nanoparticles and (b) CSA doped PANI nanotubes.

The temperature-induced crossover in *MR* from positive to negative behavior, the increase and decrease in resistance with magnetic field, as well as the modification of *MR* with doping in the present PANI nanostructures is very intriguing. There are several models to explain the *MR* behavior in organic materials such as, hopping *MR* picture [34], electron-electron interaction [243], weak localization [244] and quantum interference phenomenon [140, 142]. The hopping *MR* model is commonly used for disordered systems which exhibit VRH conduction. This model is, however, applicable if the magnetic length $L_H = (\hbar/eH)^{1/2}$ is comparable to the hopping length R_{hop} . The calculated value of L_H at 8 T field comes around 9 nm while the hopping length [calculated from conductivity data in the earlier section] is in the range of 17 - 35 nm for the HCl doped nanofibers, and HCl and DBSA doped nanoparticles, which implies that this model may not be valid for these materials. However, the hopping length for the CSA doped nanotubes is in the range of 5 - 11 nm which is comparable to the magnetic length. This means that the hopping *MR* can explain the origin of positive *MR* in the CSA doped nanotubes but not the negative *MR*. The VRH model applicable in these nanostructures leads to an increase in resistivity under the application of magnetic field, but these systems show both positive and negative *MR* in two different temperature regimes.

The electron-electron interaction model is valid at low temperatures (below 10 - 15 K), where the thermal energy $k_B T$ is less or comparable to field-induced Zeeman energy. The weak localization due to quantum corrections is another mechanism for *MR*, where the applied field affects the interference leading to a decrease in resistivity i.e., negative *MR*. This theory is, however, based on weak spin-orbit coupling while such strong coupling causes an antilocalization effect leading to positive *MR*. In conducting polymers, the spin-orbit coupling is generally weak and thus the positive *MR* cannot be explained with this model. Another effect which results in negative *MR* is the quantum interference of possible hopping lengths. From the above discussion, it appears

that these models can less likely explain the *MR* behavior observed in the present PANI systems.

Recently, studies have shown a reasonable *MR* in non-magnetic organic semiconducting materials which have been explained on the basis of charge carriers [245]. The large low-field magnetoresistance observed in organic semiconductors at room temperature is dubbed as organic magnetoresistance (OMAR). The modification of charge density and its mobility in presence of magnetic field are assumed to be responsible for the *MR* behavior in these materials. The former is valid for the systems with bipolar charge carriers (electron-hole) which form pairs giving rise to an excited state. On the other hand, charge carrier mobility driven *MR* mechanism is evident in systems with single charge carrier which are unlikely to form excited states. The basic premise of this mechanism is that single carriers generate different kinds of charge carriers, where the magnetic field induces an intertype conversion. As different types of carriers have different mobilities; as a consequence a *MR* is observed. The bipolaron model proposed by Bobbert et al. [147] is based on the spin-dependent inter-conversion between polarons and bipolarons; the applied magnetic field can change the bipolaron density and consequently affect the overall charge transport in these non-magnetic semiconductors. The charge carriers in these disordered organic systems interact with the lattice vibrations forming polarons and bipolarons, and the usual conduction occurs through a variable-range hopping of polarons between randomly localized sites. These polarons and bipolarons have different mobilities owing to their different degree of lattice distortion. Due to the energetic and positional disorder, the charge transport in disordered organic semiconductors occurs through a limited number of percolation paths. On such paths, a trapped carrier poses a blockage to the passage of the mobile carriers. According to this model, depending on the spins of the two identical carriers or polarons, a bipolaron is formed as an intermediate state, subsequently allowing the carrier to pass.

In such a case, the spins of two polarons can align either in parallel or antiparallel direction forming triplet and singlet states, respectively. However, the parallel spin alignment (triplet) is usually responsible for a 'spin blocking' state. In the absence of externally applied magnetic field, spins of individual polarons align randomly following an internal hyperfine field arising from the hydrogen atoms. When an external magnetic field is applied, it competes with the internal field; thus manipulating the spin orientation of polarons. Each carrier experiences a different hyperfine field and in the presence of external field, each spin precess around the field. This precession changes the original spin orientation as the carriers now experience different average field, which has large influence on the charge transport [150]. On application of large magnetic field (much greater than the hyperfine field), all the spins are forced to precess around the same field decreasing the possibility of bipolaron formation, as all the spins are in parallel arrangement. This triplet situation thus inhibits the charge transport, as discussed earlier. The details of bipolaron model have been discussed in section 2.1.3.3 of Chapter 2.

Now, we discuss the origin of both positive and negative *MR* i.e., magnetic field-induced increase and decrease of resistance in the context of bipolaron model. At low temperatures with less thermal energy, electrical conduction is realized through hopping of a polaron to a neighboring site, which is already occupied by another polaron. This opens a possibility to form a bipolaron. However, in presence of increasing magnetic field, a triplet state for bipolaron formation is the more probable spin configuration; therefore spin blocking state will arise and resistance will increase. This eventually explains the positive *MR* in the low temperature regime [246]. At elevated temperatures, however, the polarons have necessary and sufficient energy to bypass the previously occupied site and hop to distant unoccupied sites. Thus the magnetic field assists the charge carriers i.e., polarons to hop with relatively large mobility. As a consequence, a negative *MR* is realized at high

temperatures. According to this model, the field dependent MR follows the empirical relation as follows [151]:

$$MR = MR_{\infty} \frac{H^2}{(|H| + H_0)^2} \quad (5.10)$$

where MR_{∞} is the value at infinite magnetic field, H_0 is the characteristic field width. The value of H_0 is dependent on the branching ratio $b = r_{\alpha \rightarrow \beta} / r_{\alpha \rightarrow e}$, where $r_{\alpha \rightarrow \beta}$ is the rate at which a carrier from a singly occupied site α hops into a neighboring singly occupied site β forming a bipolaron, and $r_{\alpha \rightarrow e}$ is the rate at which a carrier from site α bypasses site β and hops into an unoccupied site in the environment. It simply implies that H_0 is directly related to bipolaron formation probability.

To understand the MR behavior in the present PANI systems, we have borrowed the bipolaron model which has been successfully employed in case of organic semiconductors to study OMAR [247]. We are justified in doing this so because single charge carriers are present in these materials as well as signature of polarons as charge carriers is evident in these systems (discussed in section 4.3.2 and Table 4.2 of Chapter 4). However, there are certain differences between the MR behavior observed in the present systems and organic semiconductors. For instance, organic semiconductors exhibit reasonable MR (around 10%) at relatively small magnetic fields ~ 10 mT. Moreover, the OMAR is found to almost saturate within this field regime.

On the contrary, Figures (5.10 and 5.12) show that the MR in the PANI nanostructures is relatively low and continuously changes with applied magnetic field, as high as 8 T, which is quite intriguing. The recent studies of MR behavior in conducting polymers have shown the similar trend, where the MR does not saturate till very high fields [138]. Furthermore, in spite of several experimental findings of MR in conducting polymers, no concrete theoretical understanding has been developed to explain the temperature-induced

transition in MR . In this scenario, we have attempted to analyze our data invoking the theoretical model used to explain OMAR.

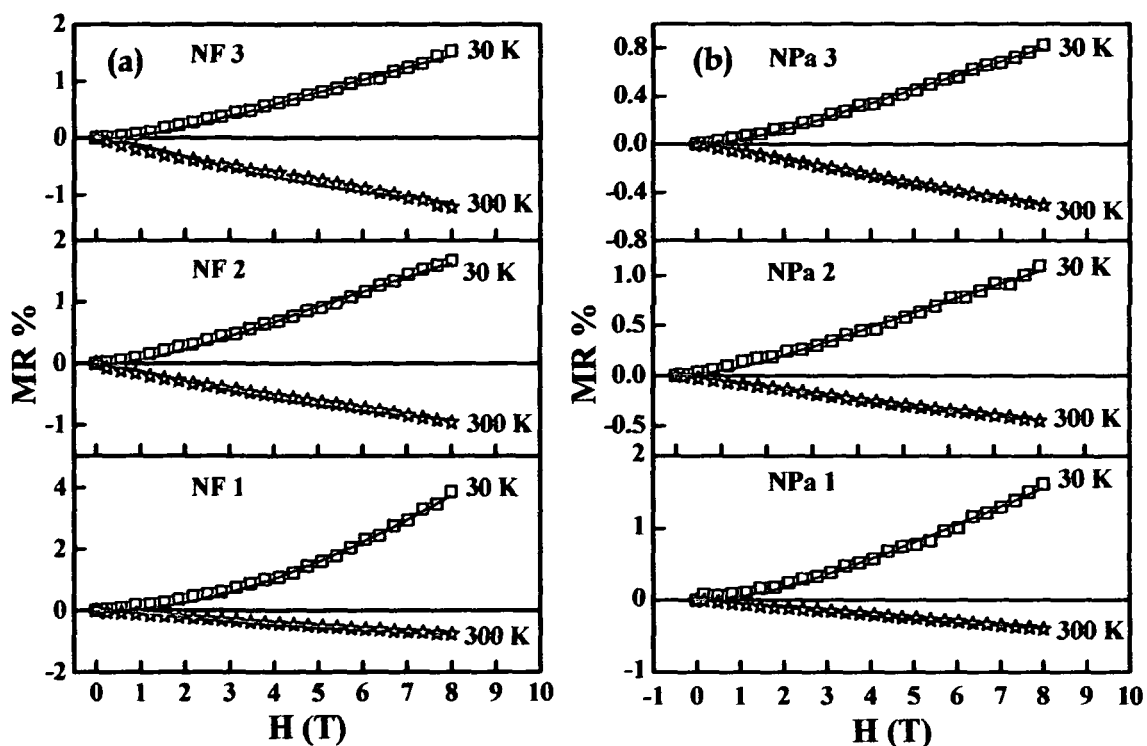


Figure 5.14: Representative fitting of MR according to Eq. (5.10) at 30 K and 300 K for HCl doped PANI (a) nanofibers and (b) nanoparticles.

Figures 5.14 (a & b) show the representative fitting of $MR(H)$ data with Eq. (5.10) for the HCl doped PANI nanofibers and nanoparticles, respectively at temperatures 30 K and 300 K. The figures also show reasonably good fitting of the experimental data using Eq. (5.10). These are two representative plots and we have found similar good fitting for MR at all temperatures, and for all the nanostructure samples. This fitting implies that the theoretical model in Eq. (5.10) can be applied to the present nanostructure samples. The parameters MR_{∞} and H_0 have been extracted from the fitting.

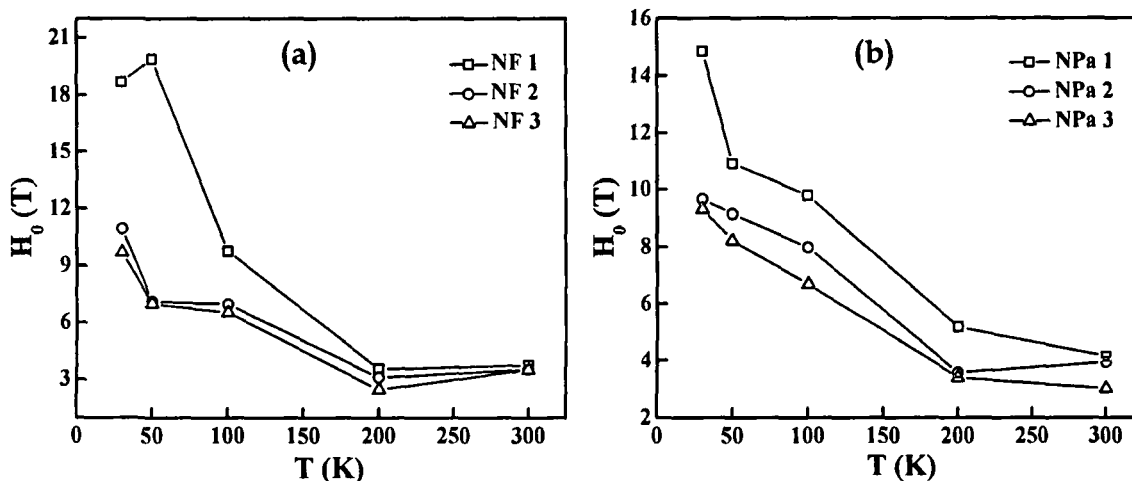


Figure 5.15: Temperature dependence plots of H_0 for HCl doped PANI (a) nanofibers and (b) nanoparticles.

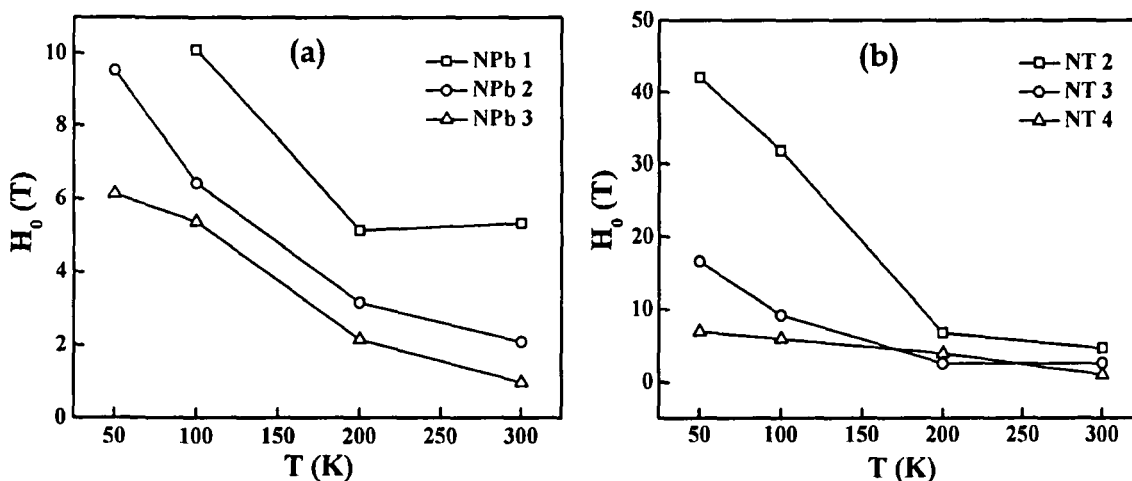


Figure 5.16: Temperature variation of H_0 for (a) DBSA doped PANI nanoparticles and (b) CSA doped PANI nanotubes.

In Figures (5.15 and 5.16), we have shown the H_0 vs. T plots of the nanostructures. It is evident from the figure that at low temperatures H_0 has higher values for all the samples implying that the bipolaron formation probability is high at low temperatures, which agrees with this model. Bipolarons are spin compensated bound polaron pairs which are non-conducting because the hopping probability of these charges in a chain is very small. As more bipolarons are formed, there are less free carriers to carry

current increasing the resistance i.e., positive MR [246]. Moreover, it is observed from the figures that H_0 decreases with doping for the nanostructures. However, at higher temperatures where a negative MR is observed, H_0 values are quite small and do not exhibit any temperature variation. The low values of H_0 imply decreased number of bipolarons at high temperatures, which increases the number of free carriers, hence decreasing the resistance resulting in negative MR . While the temperature variation of H_0 is previously observed in other (Alq_3) compounds [133], but the change in $H_0(T)$ in these nanostructures with doping is quite noteworthy, and deserves further study in similar kind of materials with varying doping concentration as well as doping elements. We find that the bipolaron model can qualitatively explain our data along with its temperature-induced transition. Though there is enough space for better theoretical investigation and further examining the applicability of bipolaron model in conducting polymers, but the present analysis is quite noteworthy.

5.4 Current-voltage characteristics

Temperature dependent steady state current (I) - voltage (V) characteristics in conducting polymers provide useful information regarding the conduction mechanism and the carrier mobility. A non-linear I - V curve often reveals the existence of different conduction mechanisms in the polymer. Generally, at low bias voltages, the current varies linearly with voltage showing Ohmic behavior. At high applied voltages, the I - V characteristics become non-linear and are space-charge-limited. The current can become space-charge-limited only when the injection carrier concentration exceeds the intrinsic carrier concentration. In general, non-Ohmic or non-linear behavior arises due to any of the following two factors: (1) at higher voltages, a relatively higher concentration of carriers in transit to the collector electrode is present between the electrodes which constitute a space-charge, (2) the presence of traps in conducting polymers due to disorder gives rise to highly localized energy levels in the HOMO-LUMO

band gap. These traps filled by injection of carriers become electrically charged contributing to the space-charge as well [248]. Thus the space-charge-limited conduction (SCLC) in a trap-filled solid has two main contributions from injection of carriers and charged traps. SCLC in organic devices can be observed when at least one of the contacts is Ohmic [129]. In the present set of devices both the contacts are Ohmic and hence the occurrence of SCLC is obvious.

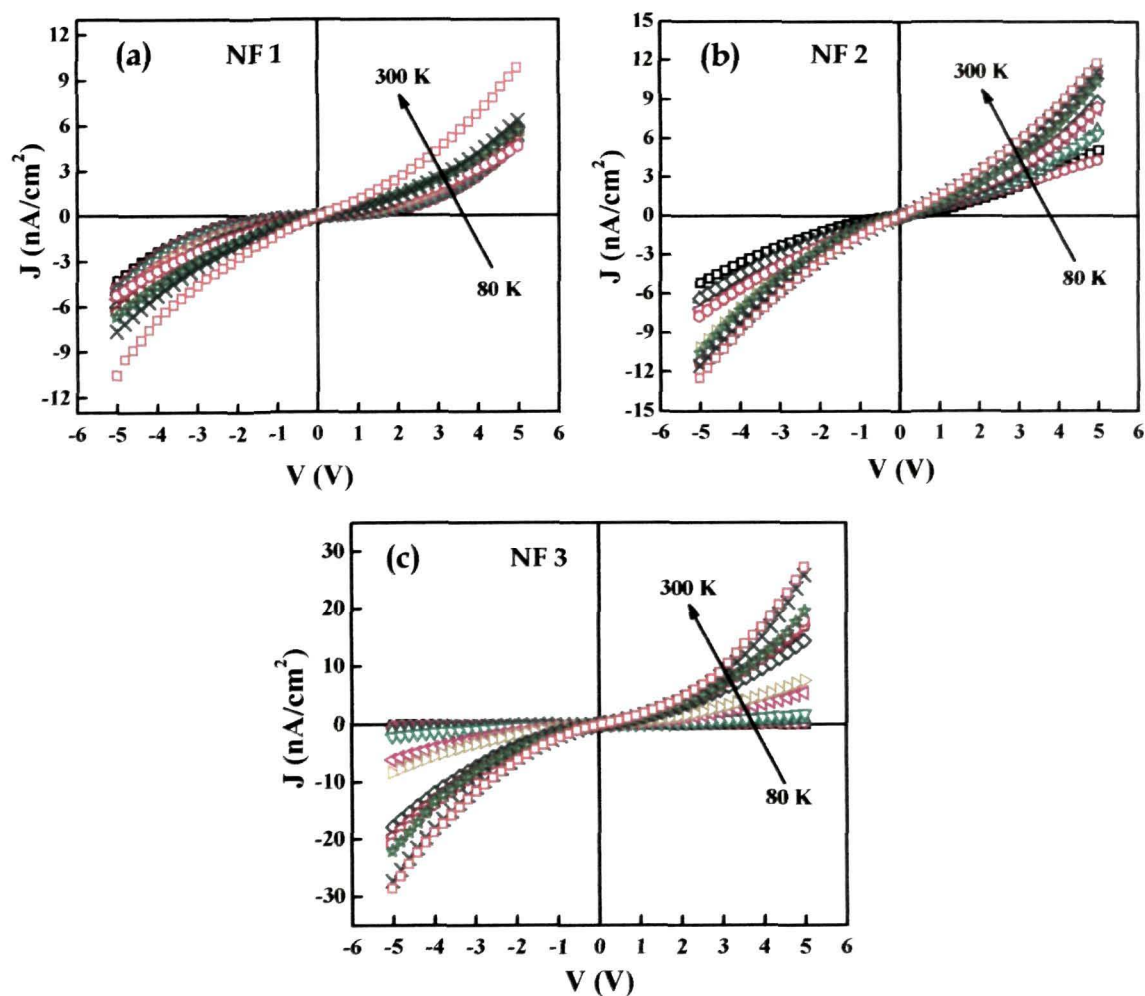


Figure 5.17: J - V characteristics of HCl doped PANI nanofibers (a) NF 1, (b) NF 2 and (c) NF 3.

The experimentally obtained current (I) values has been expressed as current density (J) for ease of discussion and calculations. The isothermal J - V characteristics of the three sandwich structures each of Ag/PANI-HCl

nanofibers/Ag and Ag/PANI-HCl nanoparticles/Ag in the temperature range 80 - 300 K are shown in Figures 5.17 (a, b & c) and 5.18 (a, b & c), respectively.

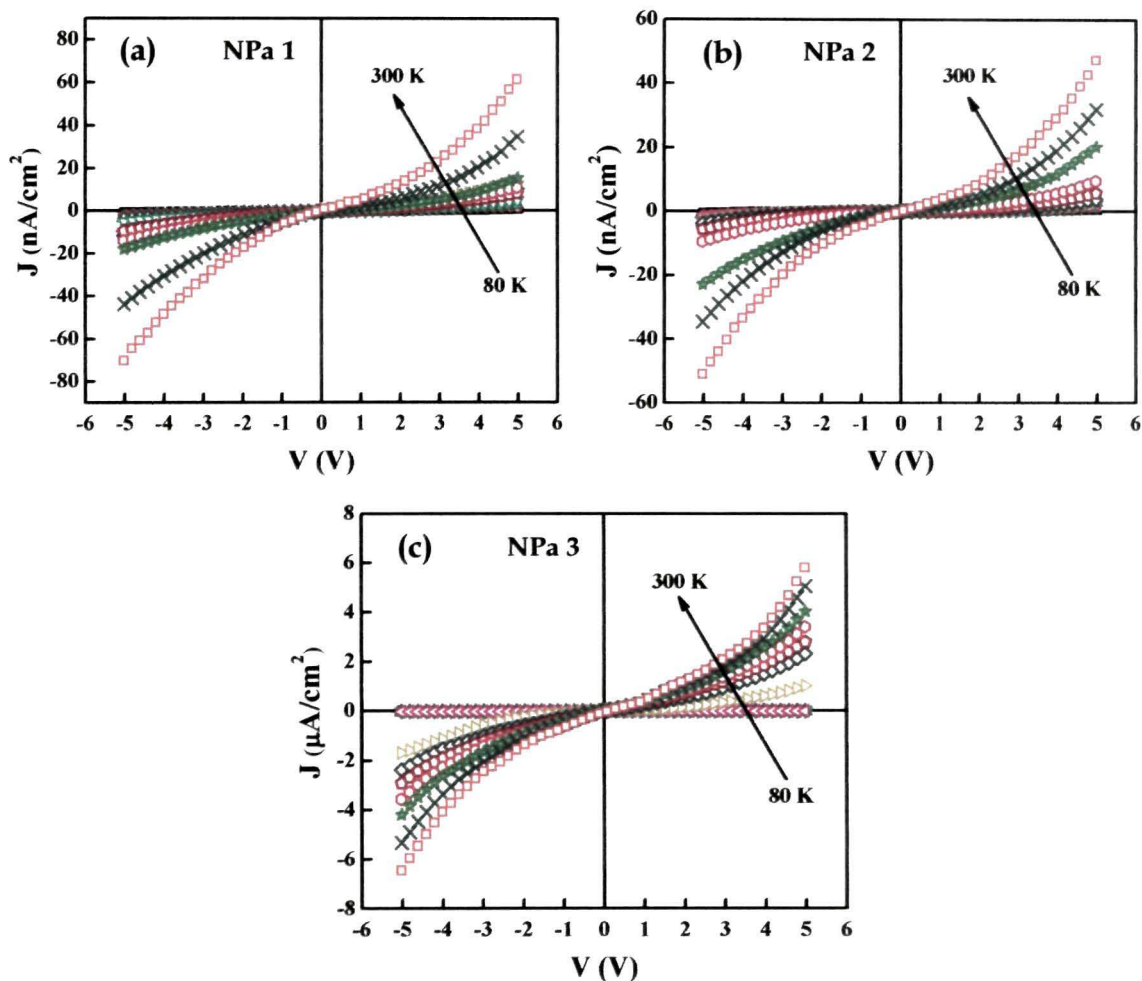


Figure 5.18: J - V characteristics of HCl doped PANI nanoparticles (a) NPa 1, (b) NPa 2 and (c) NPa 3.

Similar J - V curves for DBSA doped nanoparticles and CSA doped nanotubes are plotted in Figures 5.19 (a, b & c) and 5.20 (a, b & c), respectively. Since Ag forms Ohmic contact with PANI, the J - V curves for all the samples are symmetric. Figure 5.21 shows the energy level diagram of the Ag-PANI Ohmic contact.

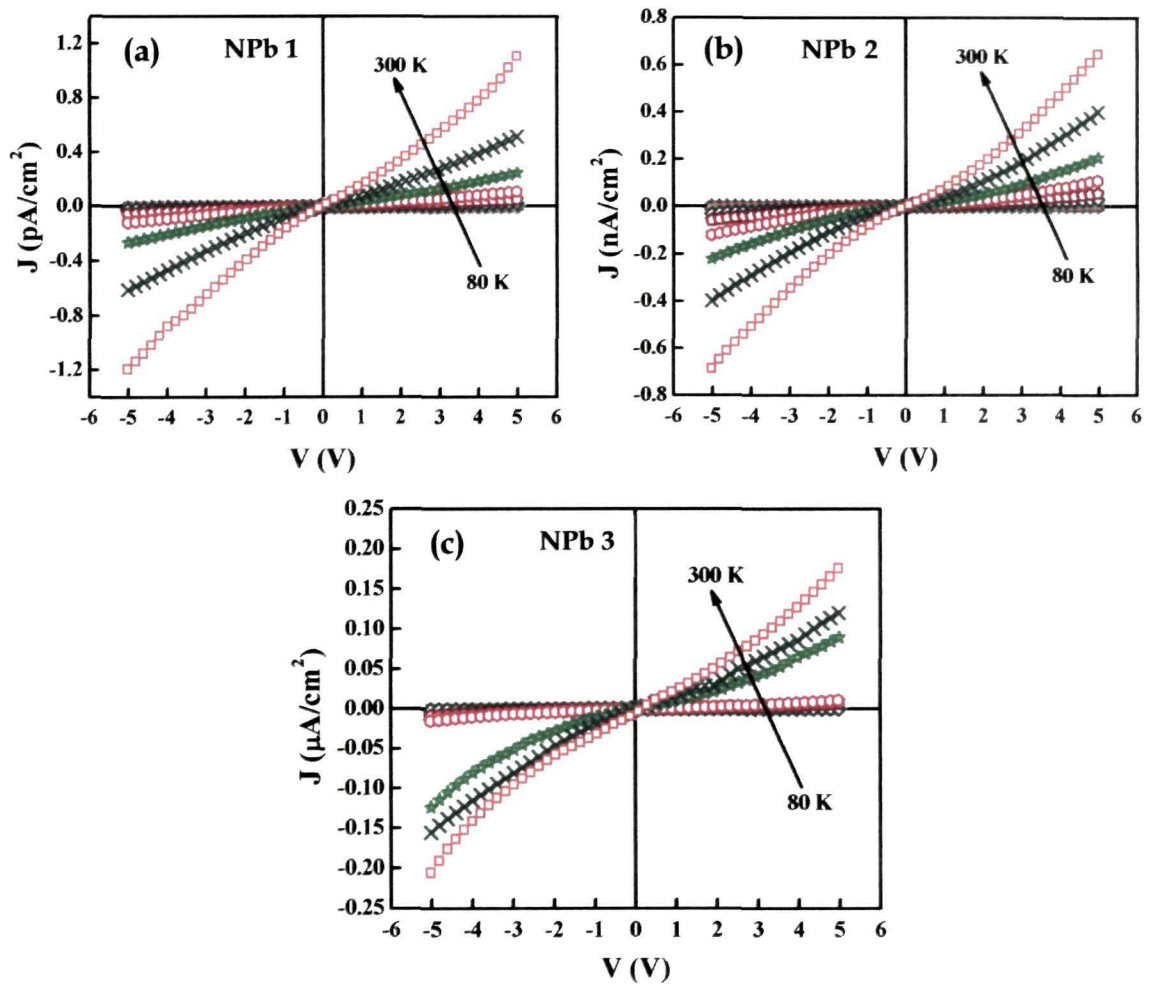


Figure 5.19: J - V characteristics of DBSA doped PANI nanoparticles (a) NPb 1, (b) NPb 2 and (c) NPb 3.

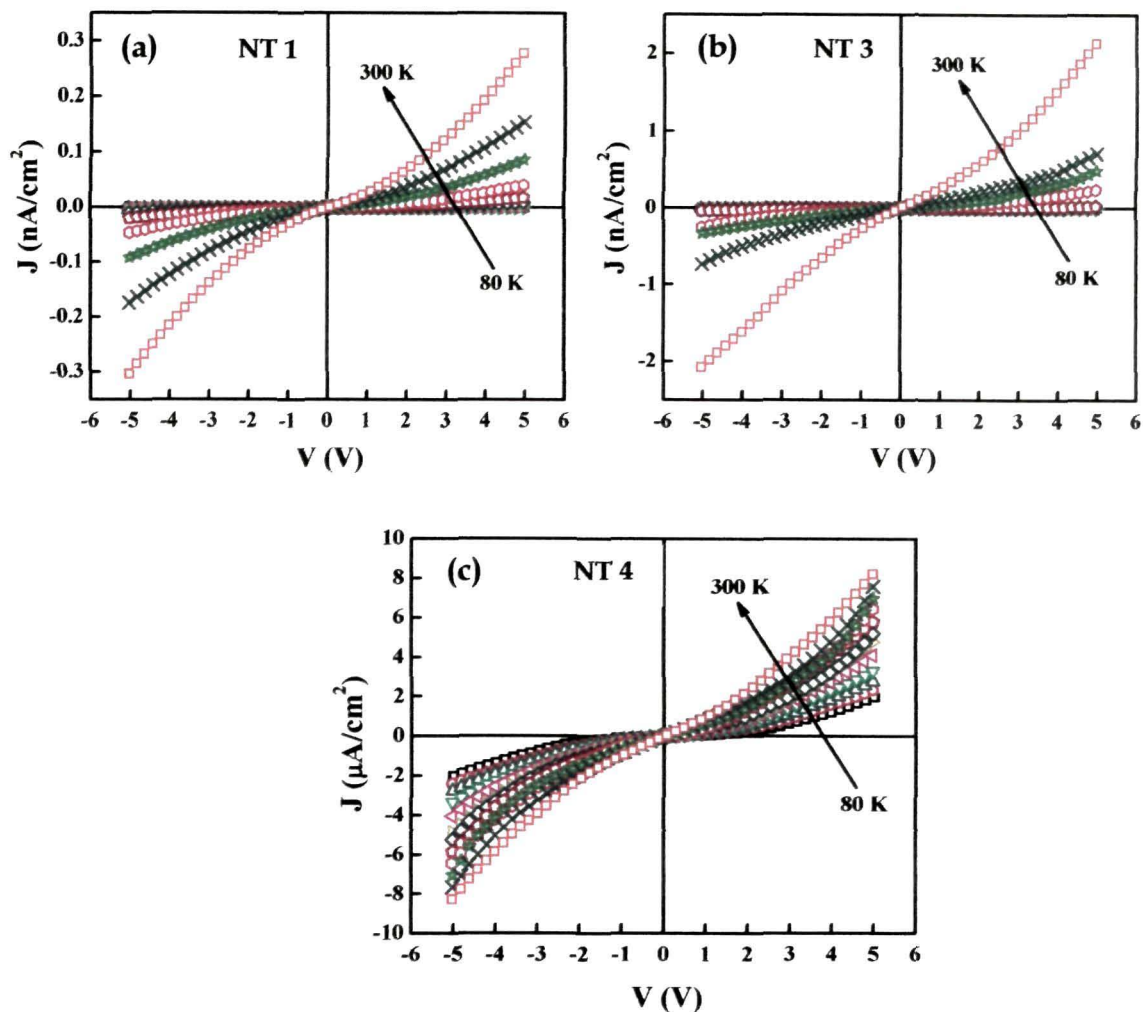


Figure 5.20: J-V characteristics of CSA doped PANI nanotubes (a) NT 1, (b) NT 3 and (c) NT 4.

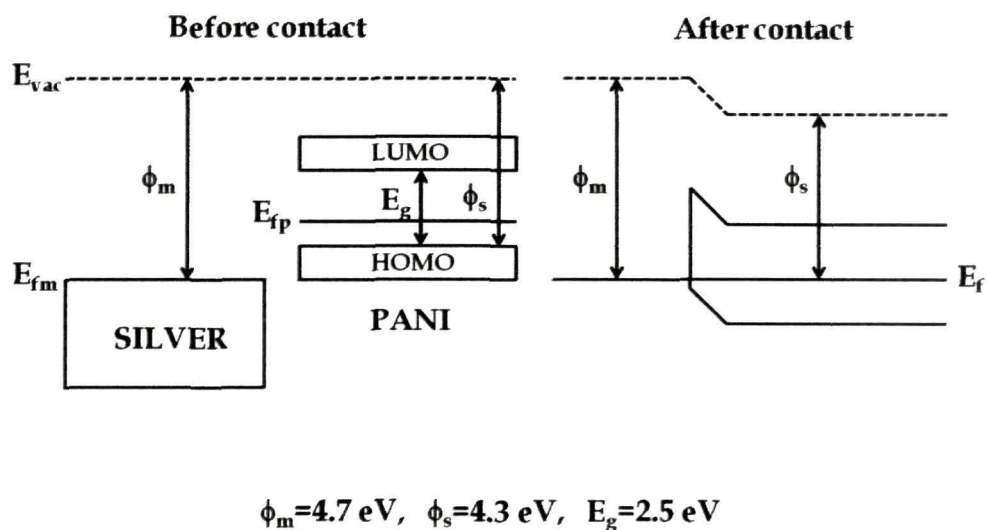


Figure 5.21: Energy level diagram of Ag-PANI Ohmic contact formation.

The nature of charge transport in the samples can be known from the slope of $\ln J$ vs. $\ln V$ curves. Figures 5.22 (a & b) represent the J - V plots of HCl doped nanofibers (NF 1) and nanoparticles (NPa 1), respectively in log-log scale. It is observed that the J - V characteristics exhibit two distinct slopes. In the lower voltage (< 1 V) region, the current is linearly dependent on voltage, indicating an Ohmic behavior. In the higher voltage (> 1 V) region, the J - V curves deviate from linearity and the slope is found to be approximately 2. The non-linear behavior of J at higher voltages is indicative of SCLC in these samples. For all the samples of different nanostructures, the slope is ~ 2 for all the temperatures indicating that the current transport is trap-free SCLC i.e., the concentration of traps is small compared to the free carrier concentration [129]. Since all the samples show similar slopes, only representative J vs. V (log-log) plots have been shown. The details of other power-law behaviors of J with V are given in section 2.1.2 of Chapter 2.

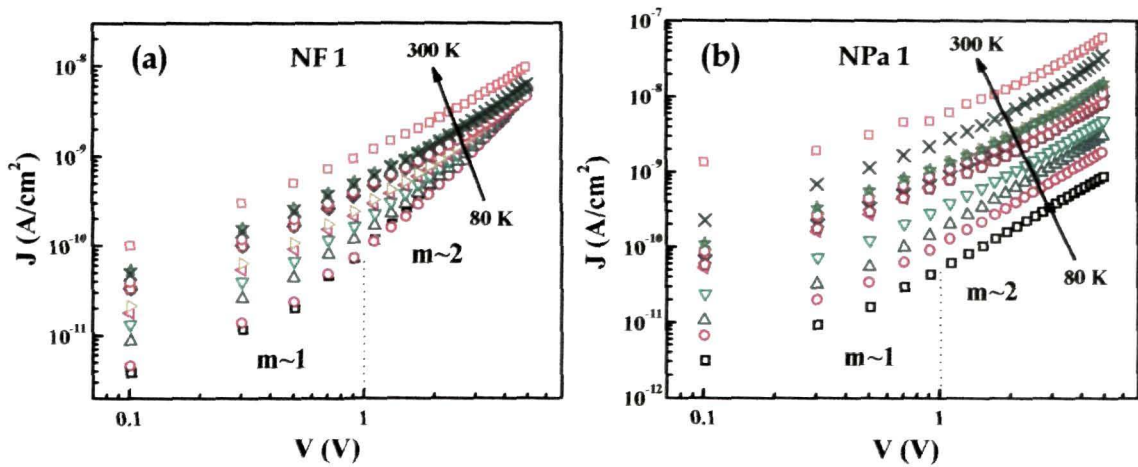


Figure 5.22: Representative J - V characteristics in log-log plots for HCl doped PANI (a) nanofibers (NF 1) and (b) nanoparticles (NPa 1).

The current for trap-free SCLC varies as the square of applied voltage (V), and is expressed by Mott-Gurney law [126]:

$$J = \frac{9}{8} \varepsilon_0 \varepsilon_r \mu \frac{V^2}{d^3} \quad (5.11)$$

where μ is the mobility of carriers, ε_0 is the permittivity of free space, ε_r is the relative permittivity and d is the thickness of the sample. As we have

understood the nature of SCLC occurring in the samples, we are now interested to evaluate the mobility (μ) and examine its field and temperature dependence. Since charge transport in conducting polymers occurs mainly by phonon-assisted hopping between localized states, the mobility strongly depends on electric field and temperature. Mobility usually increases with electric field and temperature. The electric field and temperature dependence of mobility of conducting polymers follows the universal Poole-Frenkel (PF) law of the form [41],

$$\mu(F, T) = \mu_0 \exp(0.89\gamma\sqrt{F}) \quad (5.12)$$

where μ_0 and γ are temperature dependent quantities; μ_0 is the zero-field mobility, γ is the field activation parameter of mobility and $F (=V/d)$ is the applied field. To determine μ_0 and γ for the samples, Eq. (5.12) is inserted in Eq. (5.11) i.e., the Mott-Gurney law, which then takes the form as:

$$J = \frac{9}{8} \varepsilon_0 \varepsilon_r \mu_0 \exp(0.89\gamma\sqrt{V/d}) \frac{V^2}{d^3} \quad (5.13)$$

The parameters μ_0 and γ for each temperature of the samples can be extracted from Eq. (5.13) by plotting $\ln(Jd^3/V^2)$ vs. $(V/d)^{1/2}$ as shown in Figure 5.23.

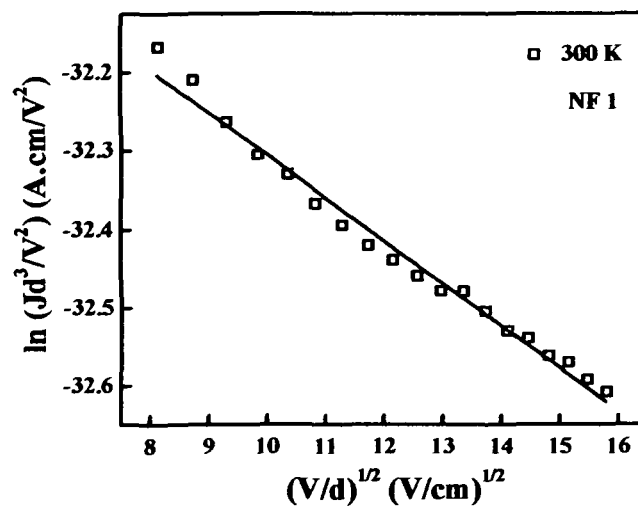


Figure 5.23: Representative plot of the data of space-charge-limited region in the form of logarithm of (Jd^3/V^2) vs. square root of electrical field $(V/d)^{1/2}$.

Figures 5.24 (a & b) represent the zero-field mobility plots for HCl doped PANI nanofibers and nanoparticles at different temperatures, while Figures 5.25 (a & b) represent similar plots for that of DBSA doped PANI nanoparticles and CSA doped PANI nanotubes, respectively.

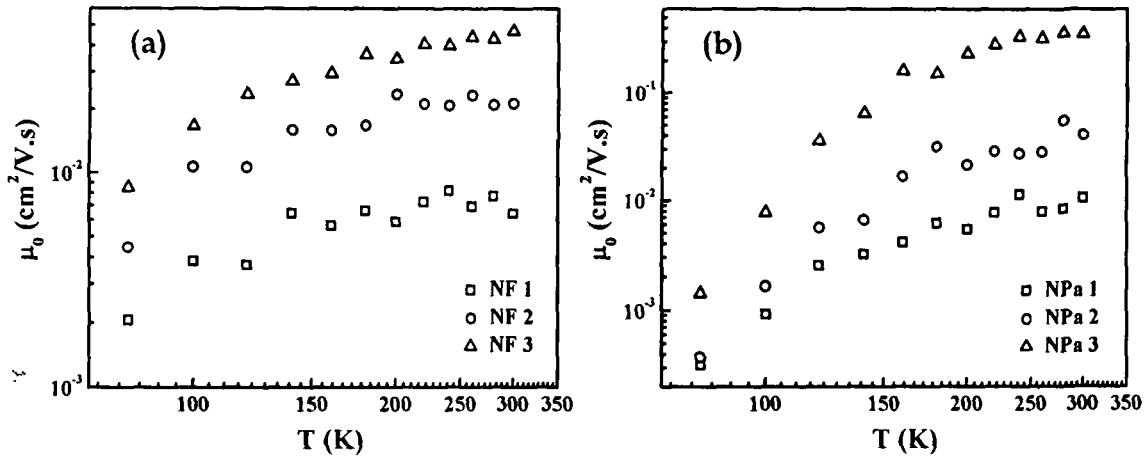


Figure 5.24: Temperature dependence of zero-field mobility (μ_0) for HCl doped PANI (a) nanofibers and (b) nanoparticles.

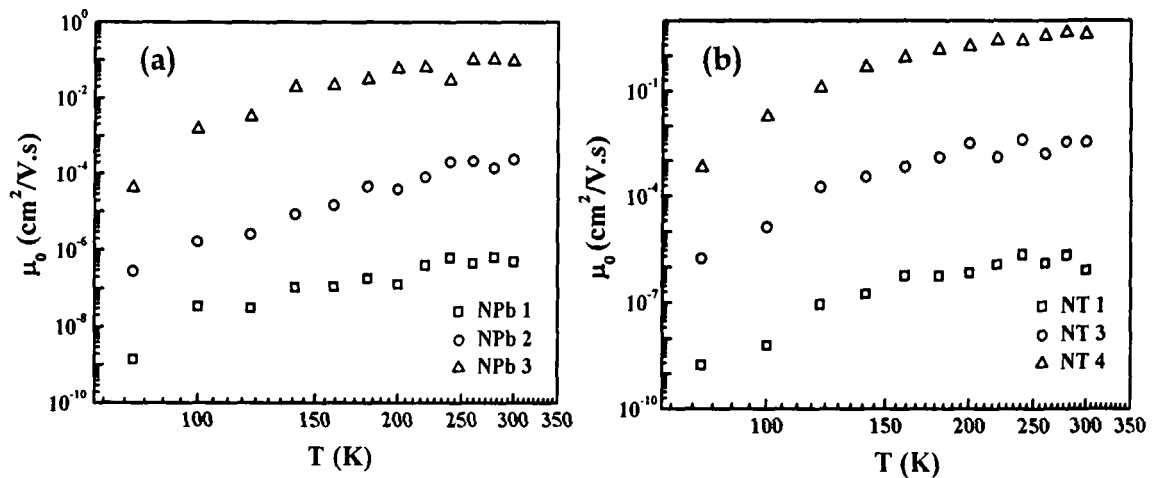


Figure 5.25: Variation of zero-field mobility (μ_0) as a function of temperature for (a) DBSA doped PANI nanoparticles and (b) CSA doped PANI nanotubes.

It is observed from the Figures (5.24 and 5.25), that the mobility increases with temperature and doping. The room temperature mobility of the carriers is of the order of 10^{-2} $\text{cm}^2/\text{V.s}$ for the HCl doped nanofibers while for the HCl doped nanoparticles, there is an increase in mobility by an order with doping from 10^{-2} to 10^{-1} $\text{cm}^2/\text{V.s}$. The lowest mobility is observed for the lowest doped

DBSA nanoparticles (NPb 1) of the order of 10^{-7} $\text{cm}^2/\text{V.s}$, while that for the highest doped is of the order of 10^{-2} $\text{cm}^2/\text{V.s}$. The highest mobility is observed for the CSA doped nanotubes with an increase from 10^{-4} $\text{cm}^2/\text{V.s}$ to 3 $\text{cm}^2/\text{V.s}$. For the same amount of dopant, the room temperature mobility of the nanostructures has the following order: NT 4 > NPa 2 \approx NF 2 > NPb 2. It has been known that charge mobility of polymers is sensitive to chain alignment [249]. Hence, the larger mobility values for the CSA doped nanotubes is ascribed to the better alignment of the PANI chains due to the hydrogen bonding of C=O group of CSA and N-H group of PANI as discussed in section 5.2 of this chapter.

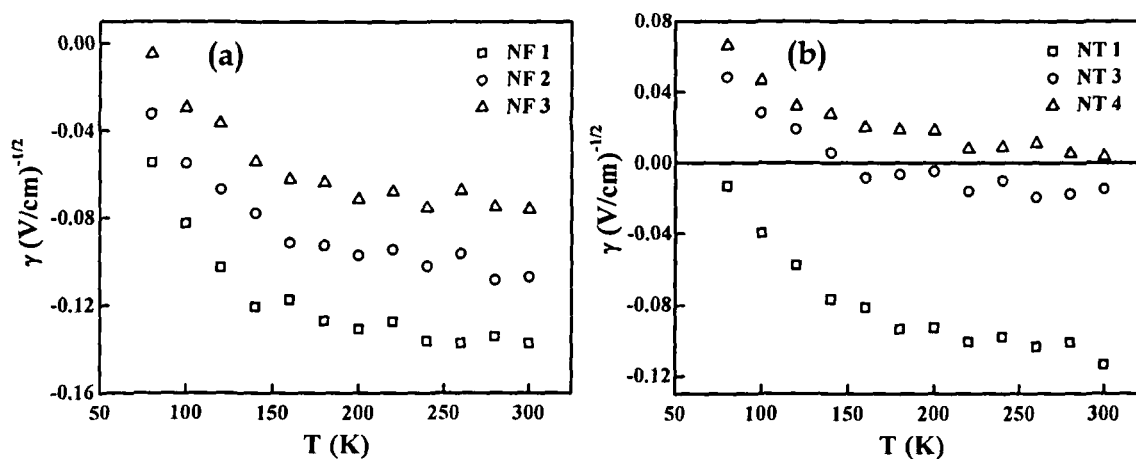


Figure 5.26: Representative plots of the temperature variation of field activation parameter (γ) for (a) HCl doped PANI nanofibers and (b) CSA doped PANI nanotubes.

The field activation parameter γ is found to be negative for all the nanostructures except for the CSA doped nanotubes, where γ exhibits a transition from positive to negative value with doping (Figure 5.26). Under the application of an external electric field F , a hopping charge carrier gets accelerated gaining an electrostatic energy equal to eFa , where e is charge and a is inter-site distance. This electrostatic energy lowers the activation energy required for the charge carrier to jump forward, resulting in a typical electric field dependence of mobility of the form $\log \mu \propto \gamma F^{1/2}$, $\gamma > 0$. Structural disorder or positional disorder can also influence the electric field dependence of

mobility in an opposing manner. The value of γ becomes negative when the positional disorder parameter Σ (measure of fluctuation in inter-site distance) exceeds the energetic disorder parameter $\sigma'/k_B T$ [250], where σ' is a measure of fluctuation in site-energies and k_B is the Boltzmann constant.

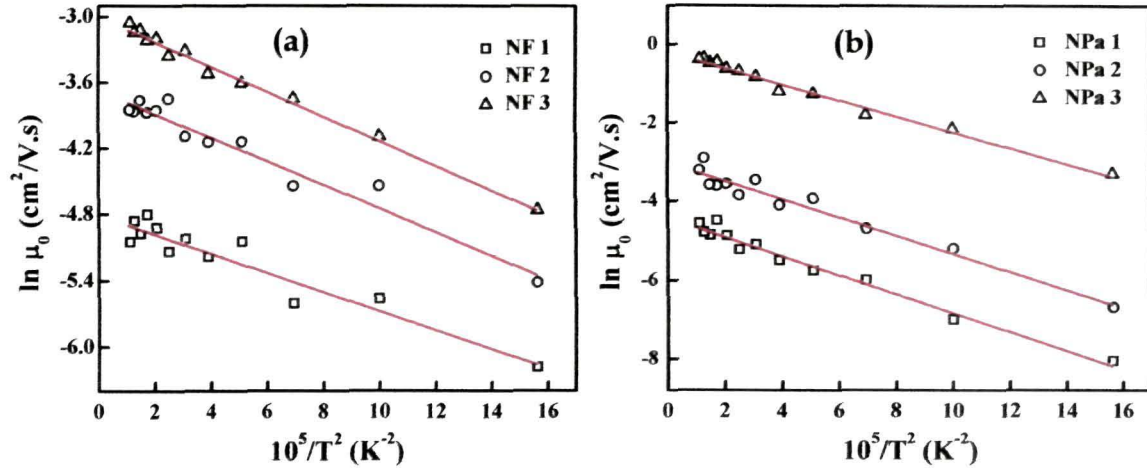


Figure 5.27: Plots of $\ln \mu_0$ vs. T^{-2} for HCl doped PANI (a) nanofibers and (b) nanoparticles. The solid line is the theoretical fit to UGDM.

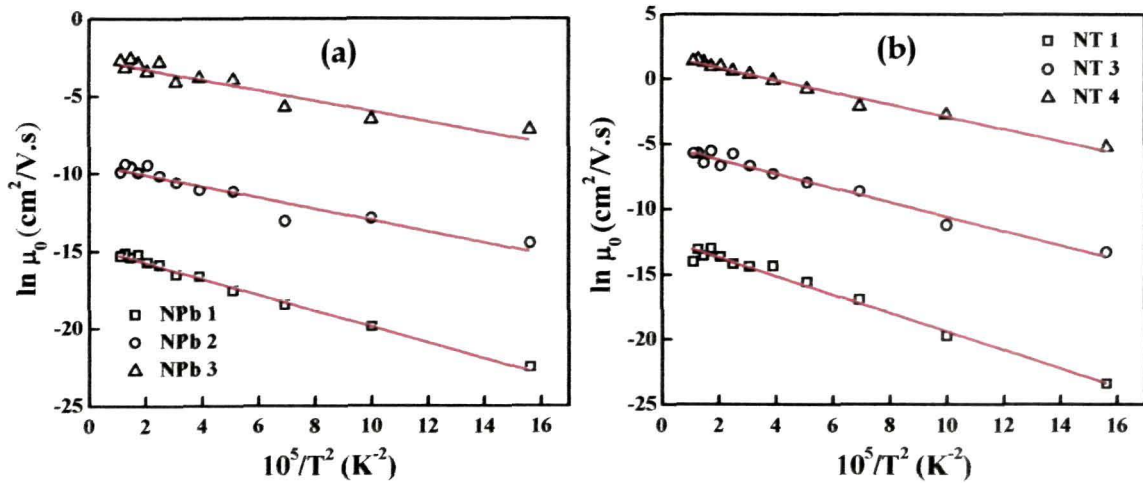


Figure 5.28: $\ln \mu_0$ vs. T^{-2} plots of (a) DBSA doped PANI nanoparticles and (b) CSA doped PANI nanotubes. The solid line is the theoretical fit to UGDM.

The obtained values of μ_0 and γ show a strong dependence on temperature and field. This kind of field and temperature dependence of mobility is a characteristic of many disordered organic semiconductors [251, 252] and is explained using the uncorrelated Gaussian disorder model (UGDM)

proposed by Bäessler [40]. According to this model, the charge transport in disordered organic semiconductors takes place by means of hopping in a Gaussian distribution of site-energies with σ' as the width of the distribution. The Gaussian DOS reflects the energetic spread of transport sites in the polymer chains due to the differences in conjugation lengths and structural disorder. Using the Monte-Carlo simulation of transport of charge carriers in a Gaussian distribution of site-energies, the functional dependence of mobility is expressed as:

$$\mu_{UGDM} = \mu_{\infty} \exp \left[- \left(\frac{2\sigma'}{3k_B T} \right)^2 + C' \left\{ \left(\frac{\sigma'}{k_B T} \right)^2 - \Sigma^2 \right\} \sqrt{F} \right] \quad \text{for } \Sigma \geq 1.5 \quad (5.14)$$

$$= \mu_{\infty} \exp \left[- \left(\frac{2\sigma'}{3k_B T} \right)^2 + C' \left\{ \left(\frac{\sigma'}{k_B T} \right)^2 - 2.5 \right\} \sqrt{F} \right] \quad \text{for } \Sigma \leq 1.5 \quad (5.15)$$

where μ_{∞} is the mobility in the limit $T \rightarrow \infty$, C' is a constant, σ' is the width of Gaussian distribution of sites (σ' is a measure of energetic disorder) and Σ describes the positional disorder. The zero-field mobility μ_0 and field activation parameter γ exhibits $1/T^2$ dependence in this model. The fits to the UGDM are shown in Figures 5.27 (a & b), 5.28 (a & b), 5.29 (a & b) and 5.30 (a & b) and the fitting parameters are given in Table 5.2.

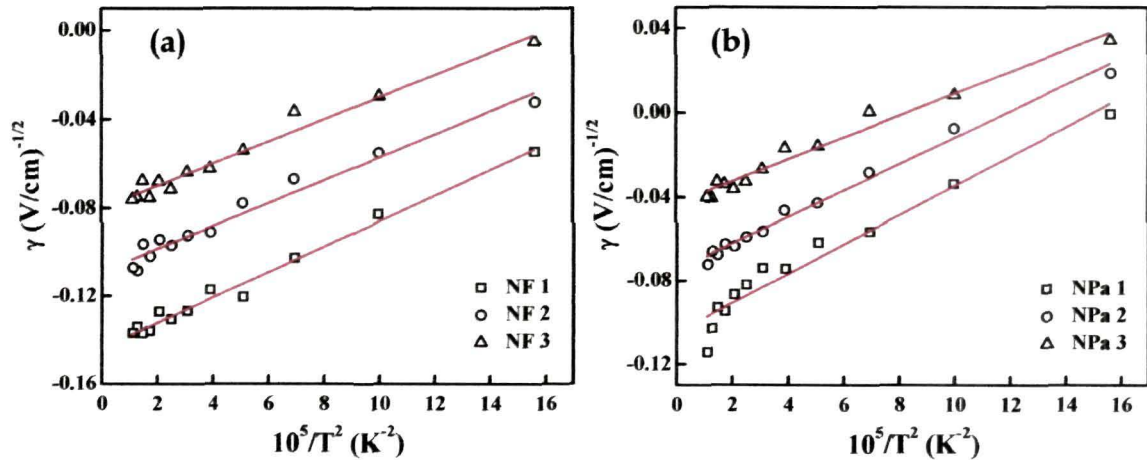
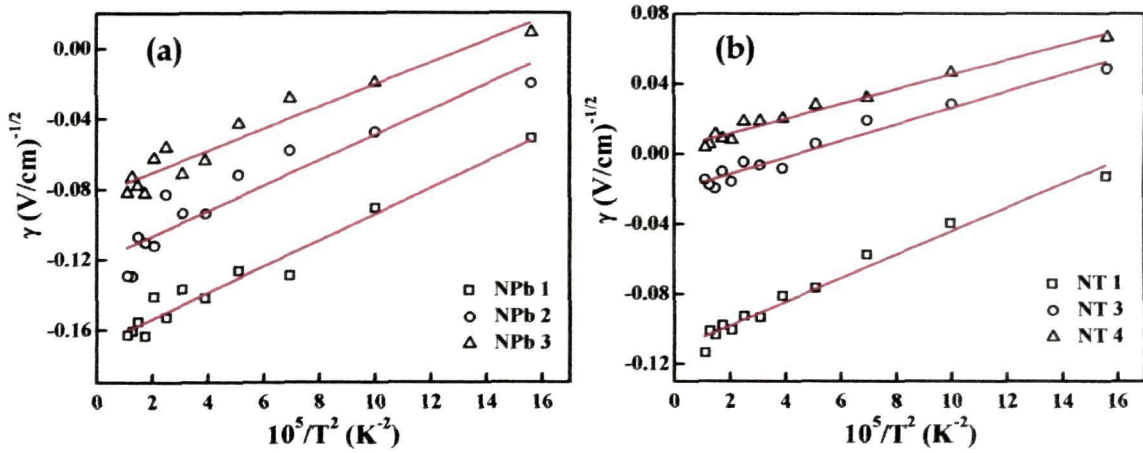


Figure 5.29: Plots of γ vs. T^{-2} for HCl doped PANI (a) nanofibers and (b) nanoparticles. The solid line is the theoretical fit to UGDM.

Table 5.2: Fitting parameters of uncorrelated and correlated Gaussian disorder models.

Sample	σ'_{UGDM} (meV)	σ'_{CGDM} (meV)	μ_{∞} (cm ² /V.s)	C' (V/cm) ^{-1/2}	Σ	a (nm)
HCl doped nanofibers						
NF 1	11.11	12.34	1.35×10 ⁻²	1.17×10 ⁻²	3.5	1.09
NF 2	12.78	14.19	2.66×10 ⁻²	2.34×10 ⁻²	2.1	0.76
NF 3	19.12	21.24	3.35×10 ⁻²	2.99×10 ⁻²	1.6	0.84
HCl doped nanoparticles						
NPa 1	18.39	20.43	1.22×10 ⁻²	1.28×10 ⁻²	2.8	1.40
NPa 2	19.58	21.76	4.93×10 ⁻²	1.21×10 ⁻²	2.4	1.24
NPa 3	20.08	22.31	8.26×10 ⁻²	1.13×10 ⁻²	1.9	0.97
DBSA doped nanoparticles						
NPb 1	23.73	26.36	4.38×10 ⁻⁷	6.40×10 ⁻³	5.1	2.42
NPb 2	24.54	27.27	8.98×10 ⁻⁵	8.81×10 ⁻³	3.7	1.06
NPb 3	29.35	32.61	8.20×10 ⁻²	8.21×10 ⁻³	3.1	1.99
CSA doped nanotubes						
NT 1	27.93	31.04	4.83×10 ⁻⁶	4.22×10 ⁻³	5.1	0.46
NT 3	30.12	33.47	6.14×10 ⁻³	3.86×10 ⁻³	2.3	0.29
NT 4	34.40	38.23	0.60×10 ¹	3.99×10 ⁻³	0.8	0.27

Figure 5.30: Plots of γ vs. T^{-2} of (a) DBSA doped PANI nanoparticles and (b) CSA doped PANI nanotubes. The solid line is the theoretical fit to UGDM.

From Table 5.2, it is observed that the width of the Gaussian DOS i.e., the energetic disorder parameter σ' increases, while the positional disorder parameter Σ decreases with doping for all the nanostructures. Increasing doping increases the ordering of the PANI chains which corroborates well with the XRD results discussed in section 4.2.2 of Chapter 4. Randomly distributed dopant counterions interact with the carriers via Coulombic interactions increasing the energetic disorder and broadening the DOS tail. Doping thus, increases the number of carriers and lifts the Fermi level up while on the other hand creates additional Coulombic traps of opposite polarity in the trap distribution [253]. The effect of nanostructuring cannot be ruled out in the charge transport where the interface between the particles can also act as trapping centers of carriers.

The UGDM could thus, explain some features of the experimental data and provide the PF behavior of the mobility; however there are several discrepancies in the model. In UGDM, the field dependence of mobility is influenced by the energetic disorder parameter σ' and the scaling factor C' . The scaling factor C' is neither a constant for a polymer nor does it correspond to a physical parameter of the polymer. The most important drawback of UGDM is that it cannot reproduce the PF behavior over a wide range of fields, $10^6 - 10^8$ V/cm [254, 39].

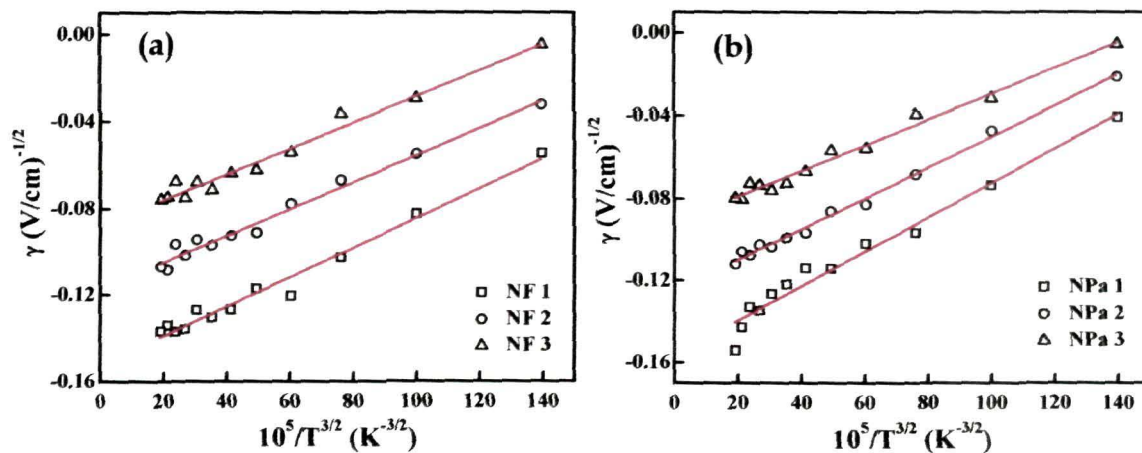


Figure 5.31: γ vs. $T^{-3/2}$ plots of HCl doped PANI (a) nanofibers and (b) nanoparticles. The solid line represents the theoretical fit to CGDM.

Recent calculations and simulations demonstrated that a spatially correlated potential is required for the description of the PF behavior of mobility over a wide range of field, and that the interaction of charge carriers with permanent dipoles located on either dopant or host molecules give rise to PF behavior of mobility [41]. The correlated Gaussian disorder model (CGDM) is therefore based on long-range correlation between charge carriers and the molecular electric dipole resulting in a random potential environment with long-range spatial correlations. In this model, the field and temperature dependence of mobility is given by:

$$\mu_{CGDM} = \mu_{\infty} \exp \left[- \left(\frac{3\sigma'}{5k_B T} \right)^2 + 0.78 \left\{ \left(\frac{\sigma'}{k_B T} \right)^{3/2} - 2 \sqrt{\frac{eFa}{\sigma'}} \right\} \right] \quad (5.16)$$

where a is the inter-site spacing. The main difference of CGDM from UGDM is the predicted temperature dependence of γ ; γ varies as T^{-2} in UGDM but it varies as $T^{-3/2}$ in CGDM. In this model, μ_0 has the same temperature dependence of T^{-2} as that of UGDM. The fits of γ to CGDM are shown in Figures 5.31 (a & b) and 5.32 (a & b). The fitting parameters of CGDM are extracted from the temperature dependence plots of μ_0 and γ and given in Table 5.2. The values of energetic disorder parameter σ' are slightly greater than that obtained from UGDM which is consistent with earlier reports [255].

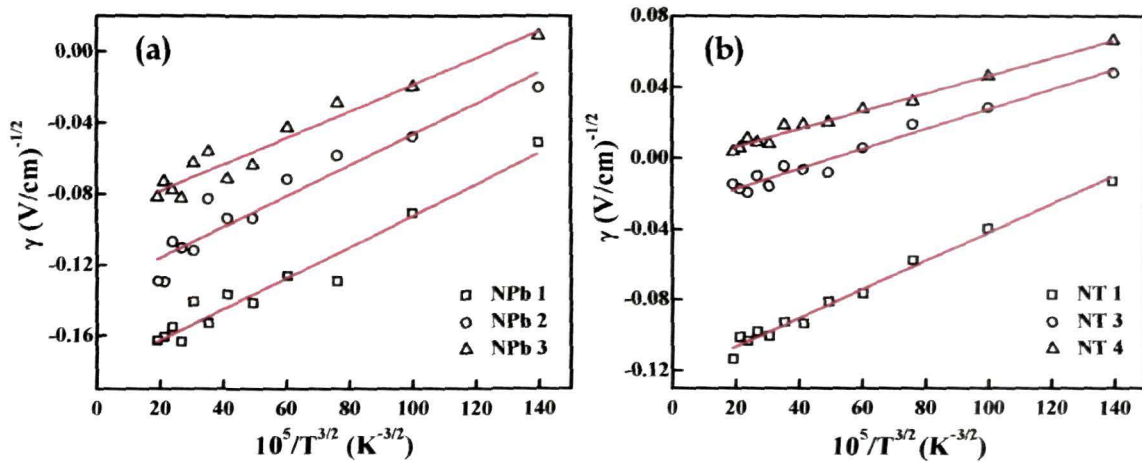


Figure 5.32: γ vs. $T^{-3/2}$ plots of (a) DBSA doped PANI nanoparticles and (b) CSA doped PANI nanotubes. The solid line is the theoretical fit to CGDM.

5.5 Summary

In summary, to understand the complex charge transport behavior in low dimensional PANI systems, viz., HCl doped nanofibers and nanoparticles, DBSA doped nanoparticles and CSA doped nanotubes, dc conductivity, magnetoresistance and current-voltage characteristic measurements were performed. The different nanostructures of PANI show different conduction mechanisms in the temperature range of 5 - 300 K. All the nanostructures exhibit metal-insulator transition at ~ 20 K. The metallic behavior below ~ 20 K is attributed to the dominant Hartree processes in the electron-electron interaction effects. In the insulating regime of the CSA doped nanotubes, the temperature dependence of conductivity is in excellent agreement with the one-dimensional Mott VRH model.

For the nanofibers and the nanoparticles, the conduction in the insulating regime occurs by VRH among the superlocalized states of the polymer, which is different from the conventional Mott VRH, and occurs in fractal systems. The superlocalization of electronic states in HCl doped nanofibers and nanoparticles is attributed to the smaller size of dopant Cl^- ion. Small size of Cl^- ion makes the polymer porous and leads to random orientation of polymer chains forcing the charge hopping to take fractional dimensions instead of Euclidean dimension as in case of CSA doped nanotubes. The bulky CSA counterion fills up the whole space and aligns the PANI chains leading to Mott's one-dimensional VRH. The long alkyl chains in the interstitial space between the PANI chains in case of DBSA doped nanoparticles makes the polymer porous and fractal-like. The Coulomb interaction between the carriers dominates the inter-site hopping in case of the nanoparticles which is attributed to the smaller size and confined morphology. The Coulomb interaction is not observed in case of nanofibers or nanotubes which is attributed to the extended spatial dimension leading to greater probability of hopping of the carriers to distant sites, and hence decreasing the effect of the interaction. The highest conductivity ~ 2.5 S/cm at

300 K is obtained for CSA doped nanotubes which is attributed to better ordering of PANI chains. The lowest conductivity is observed for the DBSA doped nanoparticles, attributed to the larger inter-chain spacing due to long alkyl chains of DBSA. Disorder is sufficiently reduced in the present nanostructure systems indicated by the lower values ($\sim 10^2$ K) of characteristic temperature T_0 . The nanodimensional control of synthesis reduces the disorder of the samples.

The nature of magnetoresistance (MR) measured in field range up to 8 T shows a transition from positive to negative with increasing temperature at around 100 K for the present doped nanostructures. With doping, the value of positive MR at low temperatures decreases, while the negative MR value at high temperature regime increases. Moreover, the transition temperature is found to decrease with doping. This temperature-induced crossover is qualitatively explained invoking the bipolaron model for organic magnetoresistance (OMAR). Electrical transport in this conducting polymer occurs through hopping of polarons. During transport, these polarons form bipolaron as an intermediate state. In presence of high field, spins of polarons are aligned; therefore bipolarons are forced to attain spin triplet state that is not a favorable scenario over the singlet state which is considered at zero fields. This reduces charge movement and hence a positive MR is observed. At higher temperatures, however, thermal energy helps the polarons to hop to distant unoccupied sites, and they avoid forming bipolarons. This excess movement of polarons in high field causes the negative MR .

The current-voltage measurements were carried out in the temperature range of 80 - 300 K to understand the influence of traps on the charge transport mechanism of PANI. In the low voltage region (< 1 V), the current varies linearly with voltage i.e., Ohmic behavior is observed for the nanostructures. Non-linear trap-free space-charge-limited conduction mechanism is observed in the high voltage region (> 1 V). Dopant type and doping level have profound effect on the mobility which can be attributed to the introduction of traps in the

HOMO-LUMO gap. The highest mobility is observed for the CSA doped nanotubes attributed to better chain alignment and ordering due to the hydrogen bonding between C=O group of CSA and N-H group of PANI. The mobility is found to be dependent both on temperature and field exhibiting the universal Poole-Frenkel behavior. The field activation parameter is found to be negative for all the nanostructures except for the CSA doped nanotubes indicative of the dominance of structural disorder over energetic disorder. However, in case of CSA doped nanotubes, a transition from negative to positive value of field activation parameter is observed with increasing doping, indicating the reduction in structural disorder.

The temperature and field dependence of mobility were examined with uncorrelated and correlated Gaussian disorder models. Doping reduces the structural or positional disorder while increases the energetic disorder of the nanostructures. Doping increases the number of carriers, and also additional traps due to the Coulomb interaction between the dopant counterions and the carriers. These additional traps broaden the DOS tail. Morphology of the nanostructures has not been found to affect the space-charge conduction, although the interface between two nanostructures might act as charge trapping centers. The present results are quite interesting from the perspective of PANI nanostructures and require further theoretical and experimental investigations taking into account the morphological aspects of the nanostructures for deeper understanding.

CHAPTER 6

Thermal transport in polyaniline nanostructures

This chapter deals with the heat transport in polyaniline nanostructures. The thermal conductivity and specific heat of the nanostructures have been investigated as a function of temperature, to gain an insight into the nature of carriers and mechanism of heat transfer in these systems. The effect of dopant type and doping level on the thermal transport of the nanostructured polyaniline systems has also been investigated.

6.1 Introduction

The development of organic electronics using conducting polymers has seen dramatic advancements over the past several decades. The beauty of such materials lies in their relative ease of processing at room temperature, potentially low-cost, and inherent mechanical flexibility. Although much effort has been made in understanding the optical and electronic transport properties of these materials and devices, very little has been done to investigate their thermal transport properties. Accurate thermal modeling of organic devices has become increasingly necessary as discrete organic electronic devices are being integrated into more complex arrays and subsystems, in which thermally-induced phenomena will play an important role [256].

Thermal transport or heat transport properties in a material are of primary importance for addressing issues concerning thermal management. While the thermal masses of most organic semiconductors used in devices are

small, the details of heat generation, dissipation, and its impact on the device require the knowledge of local thermal conductivity and specific heat of the materials comprising the device. Moreover, thermoelectric applications such as solid-state energy conversion based on the Peltier effect for cooling and the Seebeck effect for power generation require materials with high electrical conductivity and low thermal conductivity to increase the thermoelectric figure of merit [257]. A detailed study of thermal transport properties of organic polymers is therefore needed to assess their potential in these applications.

Thermal transport studies play an important role to understand the basic heat transport mechanism in materials, and therefore help to improve the material quality suited for application. In case of highly disordered systems like conducting polymers which has interspersed crystalline and amorphous regions, exhibiting an electrically metallic and insulating behavior, respectively, it is of utmost curiosity to know the nature of heat conduction. The charge carriers being polarons which are actually 'electrons dressed up in phonons'; it is indeed intriguing to identify the type and nature of heat carriers in these polymeric systems. Although there are some reports on the experimental determination of thermal conductivity in bulk polymers such as polyacetylene [97], polypyrrole [98] and polyaniline [99], the temperature dependence of thermal conductivity of conducting polymers in a wide temperature range are limited and require severe investigations.

In this chapter, the thermal conductivity and specific heat of different polyaniline (PANI) nanostructures, viz., HCl doped nanofibers (NF) and nanoparticles (NP_a), DBSA doped nanoparticles (NP_b) and CSA doped nanotubes (NT) as a function of temperature have been presented. Different samples of each nanostructure were synthesized by varying the concentration of dopant and numbered accordingly in increasing order of the doping level (details in section 3.2 of Chapter 3). The thermal conductivity (κ) measurements have been carried out in the temperature (T) range of 10 - 300 K while the specific heat measurements were conducted from 158 K - 300 K. The

variation of thermal conductivity and specific heat as a function of doping level of the nanostructures is also investigated. The κ curves exhibit a low- T peak in and around 30 K analogous to that of crystalline materials while at high temperatures, κ increases almost monotonically with T , signifying amorphicity of the system.

6.2 Thermal conductivity studies

The temperature dependence of thermal conductivity (κ) of HCl doped PANI nanofibers and nanoparticles are plotted in Figures 6.1 (a & b), respectively. Figures 6.2 (a & b) represent the κ vs. T plots of DBSA doped PANI nanoparticles and CSA doped PANI nanotubes, respectively. It is observed from the Figures (6.1 and 6.2), that the value of thermal conductivity in these systems is very low, in the range of 0.45 - 1.05 W/m.K. These low thermal conductivities are typical of amorphous materials. The smallest possible thermal conductivity in a solid as predicted by Slack in 1977 is expected, when the mean-free path of the phonons is equal to the smallest distance in the solid [258]. In our case, it is not the inter-atomic distance in the polymer but rather the inter-chain distance (weak inter-chain interaction) that limits the phonon mean-free path and ensures the low thermal conductivity.

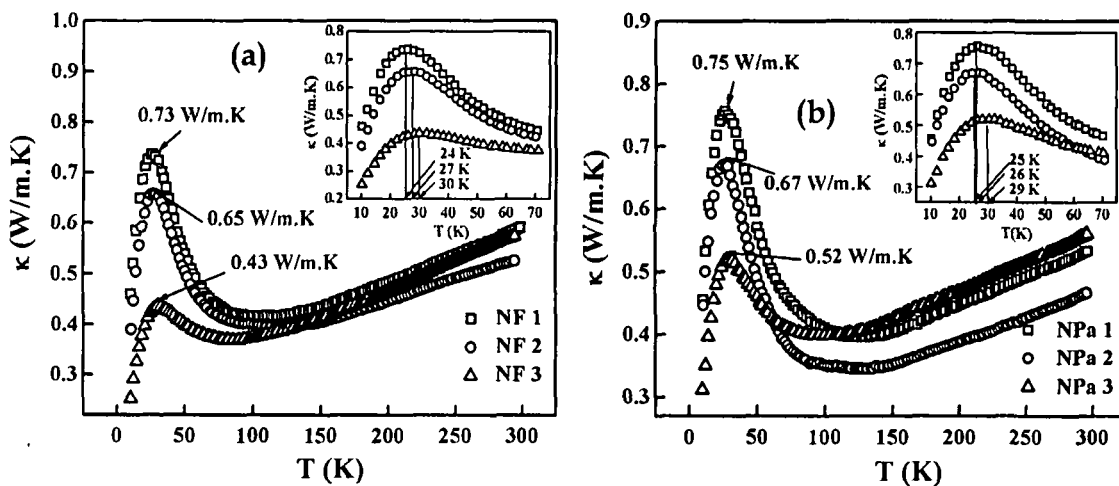


Figure 6.1: Temperature dependence of thermal conductivity has been shown for HCl doped PANI (a) nanofibers and (b) nanoparticles. Inset shows an enlarged view of the peak observed for $\kappa(T)$, with the peak position marked.

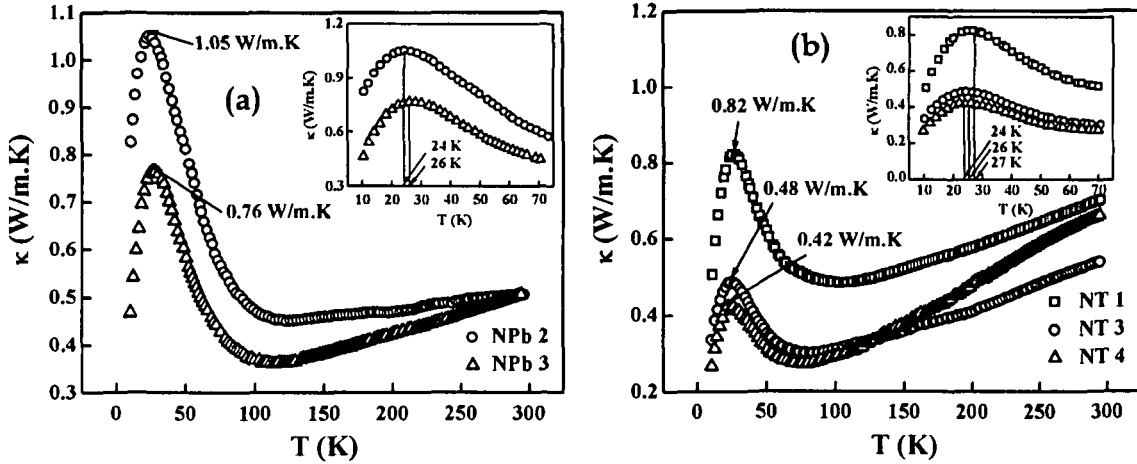


Figure 6.2: Temperature dependence plots of thermal conductivity for (a) DBSA doped PANI nanoparticles and (b) CSA doped PANI nanotubes. Inset shows the enlarged view of the peak seen in the $\kappa(T)$ curves, with the peak temperature marked.

As seen from the Figures (6.1 and 6.2), at low temperatures κ increases with rising temperature and reaches a peak at around 30 K. This feature is commonly observed in crystalline solids, and the maximum occurs at a temperature where the phonon mean-free path is approximately equal to the crystal site-distance, ascribed to the generalized Umklapp process as will be discussed in detail later. At higher temperatures above 100 K, $\kappa(T)$ increases continuously up to the temperature range of measurement i.e., upto 300 K. With increasing dopant concentration, the peak in $\kappa(T)$ is suppressed. Usually, the measured thermal conductivity is assumed to be contributed by electronic part (κ_e) and phonon part (κ_{ph}). The electronic contribution can be estimated from Wiedemann-Franz law which is valid for both metals and semi-metals:

$$\kappa_e = L_0 T \sigma \quad (6.1)$$

where σ is the electrical conductivity, T is the temperature and L_0 is the Lorenz number with a value of $2.45 \times 10^{-8} \text{ W}\Omega\text{K}^{-2}$. Following Eq. (6.1), we have calculated $\kappa_e(T)$ for all the samples while taking $\sigma(T)$ from Chapter 5 results. As illustrated in Figures 6.3 (a & b) and 6.4 (a & b), the calculated $\kappa_e(T)$ for these PANI systems is extremely small. From this estimation, we clearly demonstrate that the total thermal conductivity is mainly due to lattice phonons rather than

the charge carriers in the present PANI systems. This is very likely that in disordered systems like conducting polymers, the phonons assist the charge carriers for electrical transport [38]; hence also participate in the process of heat conduction. This result is in agreement with a recent report on the investigation of thermal and electronic transport behavior by Coates et al. [259]. They found that the link between charge and heat transport is fundamentally different in conjugated polymer systems, than in the vast majority of high conductivity materials where electrons are the carriers of both charge and heat.

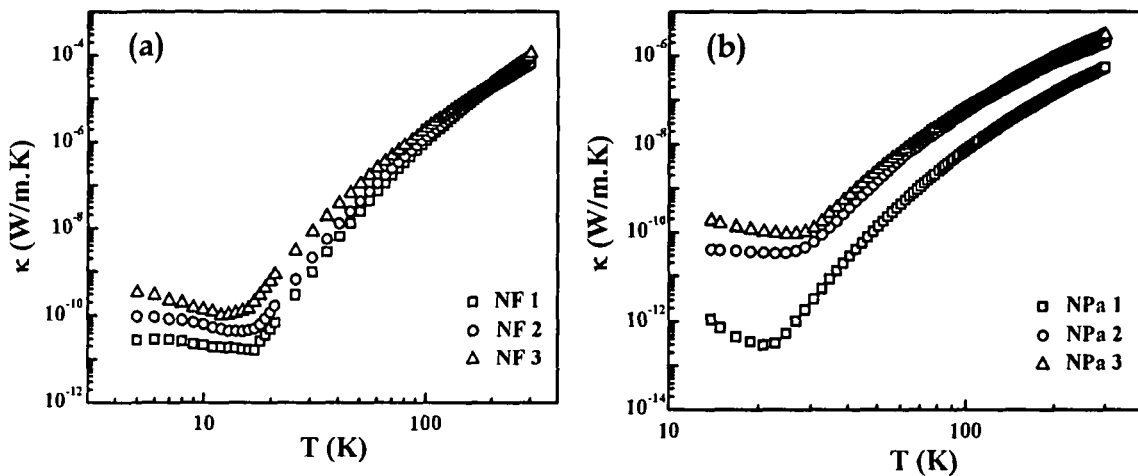


Figure 6.3: κ_e as a function of temperature for HCl doped PANI (a) nanofibers and (b) nanoparticles estimated following Eq. 6.1 using the electrical conductivity data.

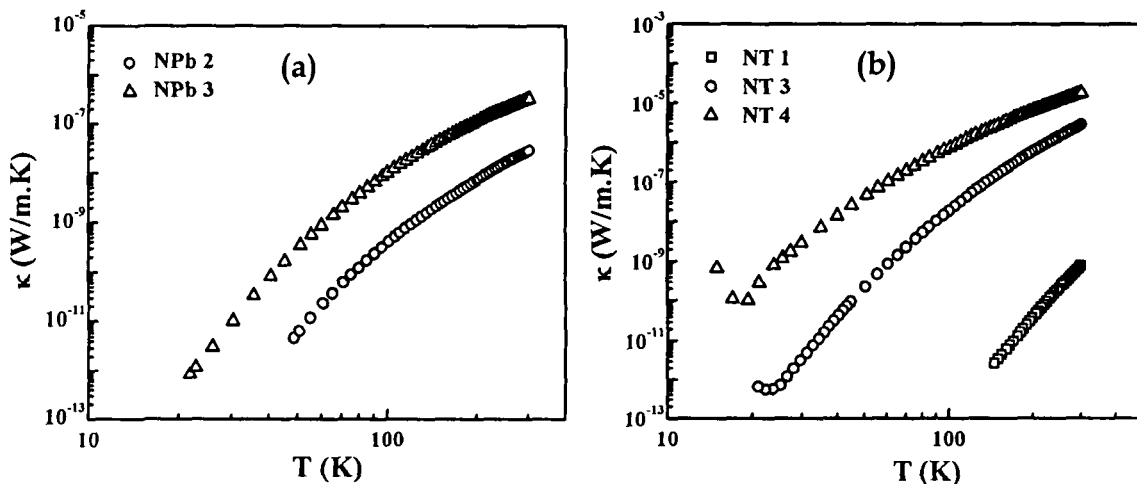


Figure 6.4: Temperature dependence of κ_e for (a) DBSA doped PANI nanoparticles and (b) CSA doped PANI nanotubes calculated following Eq. 6.1 using the electrical conductivity data.

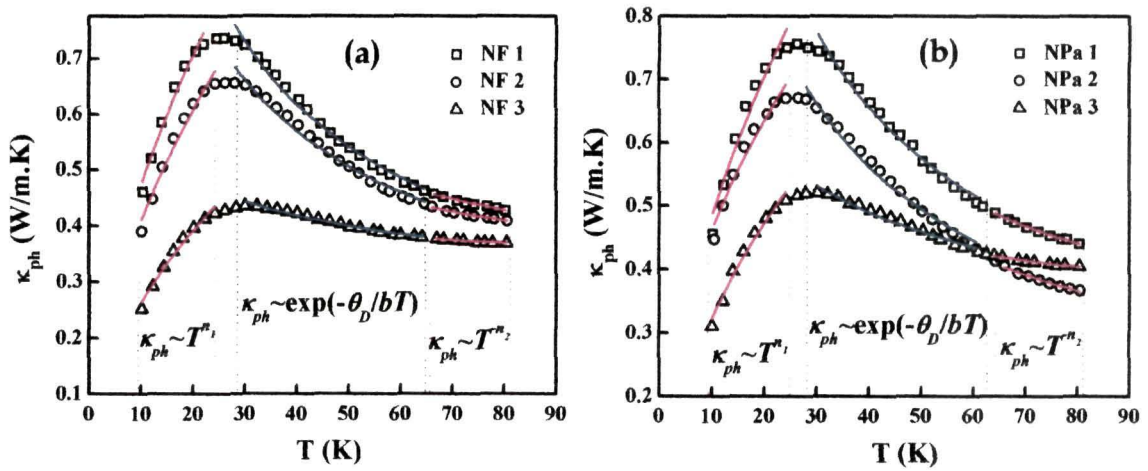


Figure 6.5: Temperature dependence plots of κ_{ph} below 100 K for HCl doped PANI (a) nanofibers and (b) nanoparticles. The different T -dependences due to different scattering processes are identified.

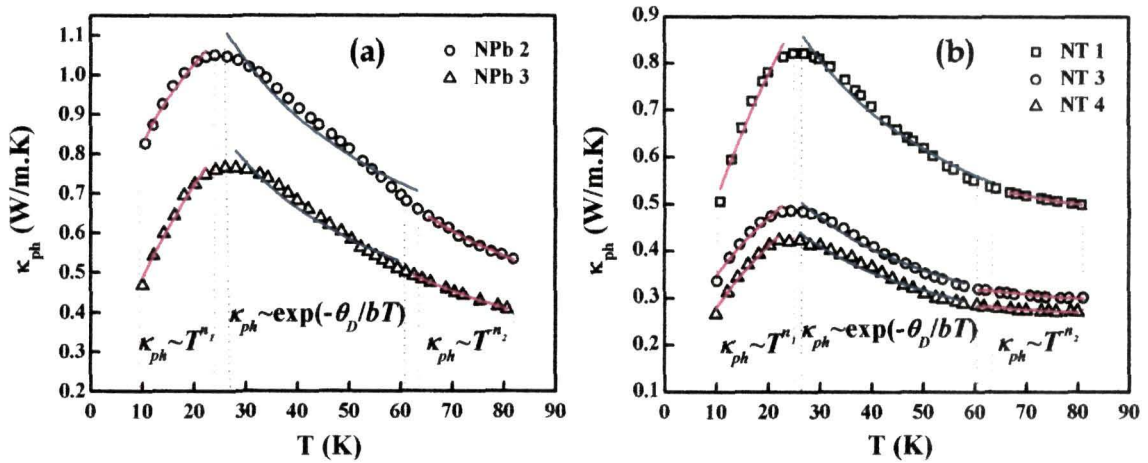


Figure 6.6: Plots of κ_{ph} vs. T below 100 K for (a) DBSA doped PANI nanoparticles and (b) CSA doped PANI nanotubes. The different T -dependences due to different scattering processes are indicated.

Figures 6.5 (a & b) and Figures 6.6 (a & b) display the temperature dependence of phonon contribution to the thermal conductivity (κ_{ph}) of the nanostructures below 100 K which is obtained by subtracting κ_c from the measured κ . It is noticed that the basic feature of the low- T peak observed in Figures 6.1 (a & b) and Figures 6.2 (a & b) remains intact, implying that the peak arises mainly due to phonon contribution. Usually, the low- T peak in κ is a characteristic feature of phonon-only heat conductivity, κ_{ph} of crystalline materials [260] which arises due to the competition between phonon-boundary

scattering and Umklapp phonon-phonon scattering. To be specific, at very low temperatures, when the thermal energy is not sufficient to excite the phonons, the phonon mean-free path is mainly determined by the dimensions of the sample, and the temperature dependence of κ is determined by that of specific heat (T^3 dependence discussed later). However, as temperature increases, the number of phonon increases which results in an increase of κ_{ph} . With further increase in temperature, the mean-free path of phonons depends on temperature as the three-phonon collision Umklapp processes rise exponentially. The Umklapp processes overcompensate the rising phonon population and thus κ_{ph} decreases with further increasing T .

Table 6.1: Values of Debye temperature (θ_D) and exponents, n_1 and n_2 related to temperature dependence of κ_{ph} below and above the peak, respectively [Figures (6.5 and 6.6)] are given for all the samples.

Sample	θ_D (K)	n_1	n_2
HCl doped nanofibers			
NF 1	240	0.58	0.34
NF 2	270	0.57	0.28
NF 3	300	0.57	0.10
HCl doped nanoparticles			
NPa 1	260	0.54	0.46
NPa 2	250	0.46	0.50
NPa 3	290	0.54	0.18
DBSA doped nanoparticles			
NPb 2	240	0.31	0.83
NPb 3	260	0.57	0.73
CSA doped nanotubes			
NT 1	270	0.60	0.26
NT 3	240	0.44	0.21
NT 4	260	0.55	0.16

The peak temperature though depends on the concentration and type of defects, Grimvall [261] anticipated this temperature to be $0.1 \theta_D$, where θ_D is the Debye temperature. From our plots in Figures (6.5 and 6.6), we have roughly estimated the value of θ_D for the present nanostructures and presented in Table 6.1. It is observed that the estimated value of θ_D is in the range of 240 - 300 K for all the nanostructures, which are in fact close to ~ 218 K as reported for PANI nanotubes [262]. The dopant type, doping level and morphology variation does not give any noteworthy information at present, except that with increasing doping, the peak value decreases. However, we speculate that the decrease in the peak value might be due to the enhancement in phonon scattering centers in the form of dopant counterions related to increasing doping level. Nonetheless, detailed studies on different systems with a wide variation of doping levels and different dopants are required to draw a plausible conclusion.

Now, we look into the temperature dependence of κ_{ph} . According to Debye model, the phonon-mediated thermal conductivity follows a T^3 dependence in the low- T limit. However, we have found a much weaker temperature dependence in the present case. For instance, below the peak our data shows, $\kappa_{ph} \propto T^{n_1}$, where the exponent n_1 for different nanostructures tabulated in Table 6.1 is found to be in between 0.4 - 0.6. Such a weak temperature dependence of κ_{ph} is rather intriguing. Similar deviation from T^3 behavior has been previously observed in low-dimensional systems, such as silicon nanowires [263]. This result implies that this unconventional behavior of $\kappa_{ph}(T)$ is related to the finite size-effect of these nanosystems. In the present scenario, the effect of finite size is realized in confinement of phonons, which modifies the phonon dispersion relation leading to a reduction in phonon group velocities [264, 265], which certainly influences the heat transport and can explain the observed $\kappa_{ph}(T)$ behavior in these nanostructures. We would like to mention that the thermal transport is not thoroughly investigated yet in low-dimensional conducting polymers. Hence, more similar experimental studies

on different conducting polymers are needed for systematic comprehension of heat transport behavior in these systems.

As passing over the peak in κ_{ph} , the number of high-energy phonons necessary for Umklapp processes decays exponentially as $\exp(-\theta_D/b'T)$ (b' is a number of order unity, 2 or 3); κ_{ph} is also expected to decrease in a similar fashion. Moreover, in this regime the mean free path also exhibits an exponential decrease with temperature. Indeed, we have obtained an exponential decrease of κ_{ph} as observed in Figures (6.5 and 6.6). At further higher temperatures before the dip in κ_{ph} , the anharmonic scattering mechanism due to phonon-phonon scattering dominates and κ_{ph} is expected to vary as T^{-1} . However, for the present system the T -dependence of κ_{ph} varies as $\sim T^{-n_2}$ as indicated in Figures (6.5 and 6.6). The exponent n_2 obtained from the fitting to $\kappa_{ph} \sim T^{-n_2}$ for the different nanostructures is presented in Table 6.1. It can be seen from the table that the value of n_2 is in the range of 0.1 - 0.8. The deviation from T^{-1} dependence of κ_{ph} can be attributed to the inherent disorder present in conducting polymers, as T^{-1} dependence of κ_{ph} is a characteristic of low-defect bulk crystal related to the anharmonic Umklapp phonon-phonon scattering [266]. The exponent n_2 decreases with doping for all the nanostructures. The smaller value of n_2 is attributed to more defects in the form of dopant counterions from which the phonons get scattered.

The behavior of $\kappa_{ph}(T)$ above 100 K where κ_{ph} increases quasi-linearly with temperature is interesting. Linear fit to the experimental data in this regime yields a temperature dependence of $\sim T^{n_3}$ for all the nanostructure samples as shown in Figures 6.7 (a & b) and 6.8 (a & b). The exponent n_3 for the nanostructures is found to be in the range of 0.4 - 0.8 and is given in Table 6.2. It is to be noted that κ_{ph} , in general, approaches a constant value at high temperatures for crystalline materials. However, in case of quasi-crystals or

amorphous solids such as metallic glasses, a linear increase in $\kappa_{ph}(T)$ at high temperatures is usually observed [267, 268]. The linear temperature dependence in glasses has long been investigated theoretically and experimentally assigning it to the hopping behavior of strongly localized modes via anharmonic interactions with the delocalized phonons [154, 269, 270]. It was proposed by Böttger et al. [156] that the significant heat carriers are the high-frequency Anderson (disorder) localized optical phonons which are coupled by low-frequency delocalized or extended acoustic phonons. Thus the quasi-linear behavior of $\kappa_{ph}(T)$ above 100 K strongly suggests the thermally activated hopping of localized phonons which is analogous to that of Mott's variable-range hopping (VRH) of charge carriers among localized states in disordered systems [231].

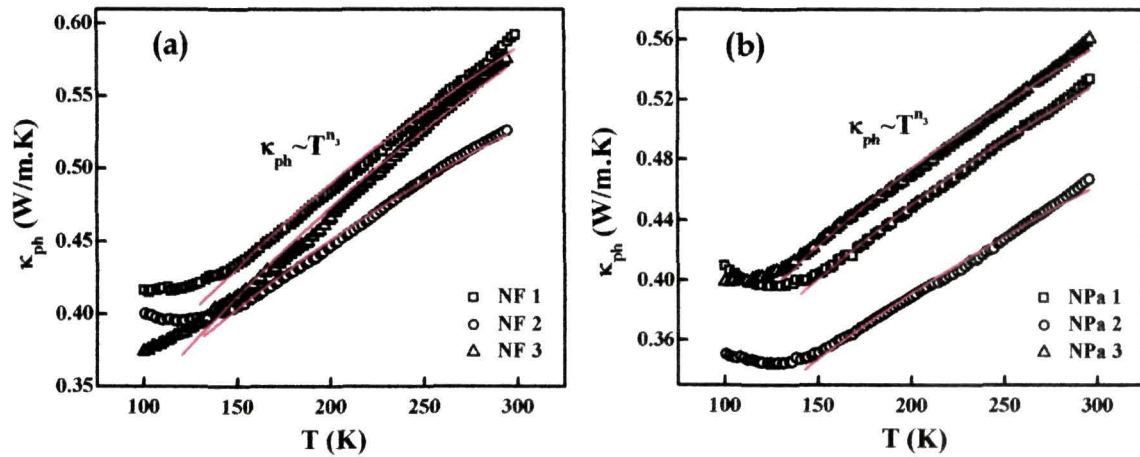


Figure 6.7: Temperature variation of κ_{ph} above 100 K for HCl doped PANI (a) nanofibers and (b) nanoparticles. The fitted lines show quasi-linear dependence of $\kappa_{ph}(T)$ with the exponent n_3 tabulated in Table 6.2.

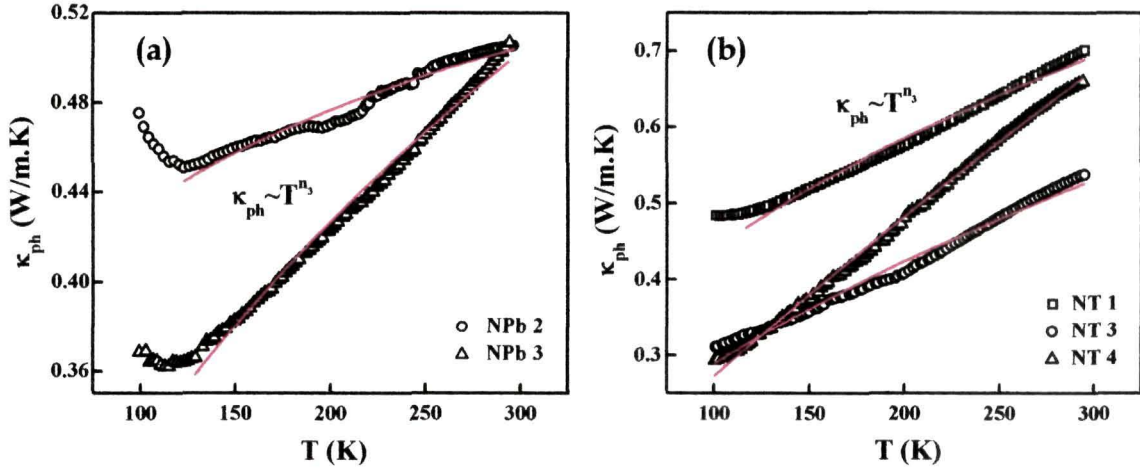


Figure 6.8: Temperature dependence of κ_{ph} above 100 K for (a) DBSA doped PANI nanoparticles and (b) CSA doped PANI nanotubes. The fitted lines show quasi-linear dependence of $\kappa_{ph}(T)$ with the exponent n_3 shown in Table 6.2.

Following this motivation, we have analyzed the hopping contribution of localized phonons using the thermally activated hopping (TAH) model initially developed by Alexander et al. [158, 159], where the localized lattice vibrations are considered to be fractons. The fractal nature of the localized phonons not being evident, later various models have been developed considering the Euclidean nature of localized modes [157]. The TAH model assumes that the phonon spectrum contains low-energy extended phonons and high-energy localized phonons separated by a minimum characteristic frequency ω_c , called the phonon mobility edge. Anharmonic coupling with extended phonons is also a prerequisite for this model. As a localized phonon hops from one state to another favorable state, the extended phonons act as a facilitator mode to attain the conservation of energy and hence contribute to the heat conduction. The characteristic length ξ_c corresponding to the crossover frequency is approximated as $2\pi v_s/\omega_c$. Phonons of wavelength less than this characteristic length scale are localized [154]. In case of silicate glasses, ω_c has been determined from the position of the 'boson peak' in the Raman spectrum [271], however, the appearance of boson peak is ruled out for PANI [208]. Moreover, due to insufficient knowledge of the phonon dispersion spectrum in conducting polymers, we consider the characteristic length ξ_c to be the lowest

possible wavelength (λ) of acoustic phonons as found in literature for polyacetylene which is $\sim 48 \text{ \AA}$ [272]. Taking the average speed of sound in conducting polymers, $v_s = 1.5 \times 10^4 \text{ m/s}$ [273], ω_c is calculated to be $1.96 \times 10^{13} \text{ s}^{-1}$. It is interesting that this value is pretty close to that observed for silicate glasses $\sim 1.4 \times 10^{13} \text{ s}^{-1}$ [154, 274].

Table 6.2: Values of the exponent (n_3) as determined from the fitting of $\kappa_{ph}(T)$ in Figures (6.7 and 6.8) and the anharmonic coupling constant (C_{eff}) as estimated using Eq. 6.2 are given for all the samples.

Sample	n_3	$C_{eff} \text{ (erg/cm}^3\text{)}$
HCl doped nanofibers		
NF 1	0.43	1.38×10^{17}
NF 2	0.38	1.49×10^{17}
NF 3	0.47	1.20×10^{17}
HCl doped nanoparticles		
NPa 1	0.40	1.42×10^{17}
NPa 2	0.41	1.29×10^{17}
NPa 3	0.39	1.50×10^{17}
DBSA doped nanoparticles		
NPb 2	0.14	2.93×10^{17}
NPb 3	0.48	1.45×10^{17}
CSA doped nanotubes		
NT 1	0.41	1.57×10^{17}
NT 3	0.55	9.31×10^{16}
NT 4	0.82	4.79×10^{16}

Here, we have attempted to theoretically understand the validity of hopping mechanism at higher temperatures. A similar hopping model considering the assumptions of TAH and Mott's VRH was proposed to explain the thermal conductivity arising from localized modes. According to this

model, the thermal conductivity contribution from the hopping of localized phonons is given by [161, 276]:

$$\kappa_{hop}(T) = \frac{192C_{eff}^2 k_B^2 G}{\pi^3 v_s^5 \rho_d^3 \xi_M^3 l_{ph}^2} T \quad (6.2)$$

where C_{eff} is the third-order anharmonic coupling constant, G is a constant of order unity, ρ_d is the mass density, v_s is the velocity of sound, l_{ph} is the localization length of a phonon and ξ_M^3 is the volume of finding a localized phonon (the length scale is taken to be the crossover length ξ_c). Assuming that the thermal conduction at higher temperatures in the present nanostructures occurs through hopping of localized phonons, we have roughly estimated C_{eff} from the slope of $\kappa_{ph}(T)$ in Figures (6.7 and 6.8). Taking $\rho_d = 1.33 \text{ g/cm}^3$ for PANI [277] and $\xi_M \approx l_{ph}$ [278], C_{eff} is obtained and given in Table 6.2. The obtained values of C_{eff} is about 3 - 4 orders greater than that observed for glasses [154, 276]. It is observed from the table that the value of C_{eff} is found to be comparatively less in case of the higher doped CSA nanotubes than that of the other doped nanostructures. This observation suggests that the anharmonic coupling between the localized and extended phonons is reduced which can be attributed to a reduced disorder in the CSA doped systems, as this will arguably lead to less localization of the phonons. This result corroborates well with the X-ray diffraction results (discussed in section 4.2.2 of Chapter 4).

6.4 Specific heat studies

Figures 6.9 (a & b) depict the T -dependence of specific heat at constant pressure (C_p) for HCl doped PANI nanofibers and nanoparticles in the high temperature side above 150 K, where $\kappa_{ph}(T)$ exhibits a linear increase. Figures 6.10 (a & b) represent the T -dependence of C_p for DBSA doped PANI nanoparticles and CSA doped PANI nanotubes, respectively. Though, C_p increases continuously with temperature, above $\sim 200 \text{ K}$, the rate of increase decreases significantly. The high- T specific heat behavior observed in the present systems is quite

similar to that observed in other crystalline and amorphous solids, where C_p increases rapidly up to ~ 300 K and then increases gradually to a saturation value at ~ 1500 K [279-282]. It should be noted here that the low- T specific heat data is not available at present due to the low thermal conductivity and/or thermal diffusivity of the samples. Similar to thermal conductivity, specific heat is also mainly contributed by electrons and phonons [260]. Therefore, from our previously observed thermal conductivity data, it can be safely assumed that phonons have major contribution to specific heat. In fact, Long et al. also ruled out the electronic contribution to C_p for PANI nanotubes [262].

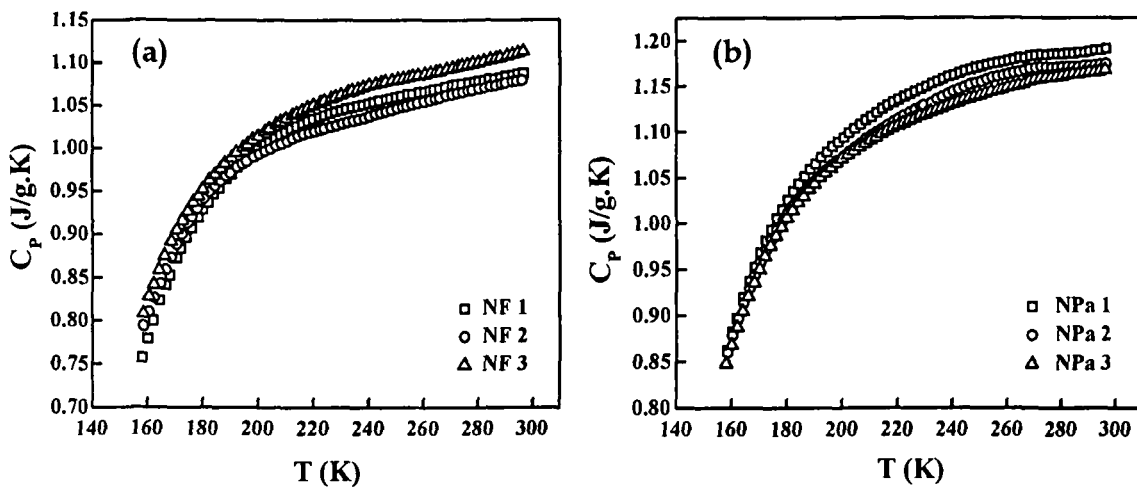


Figure 6.9: Temperature dependence of specific heat C_p for HCl doped PANI (a) nanofibers and (b) nanoparticles.

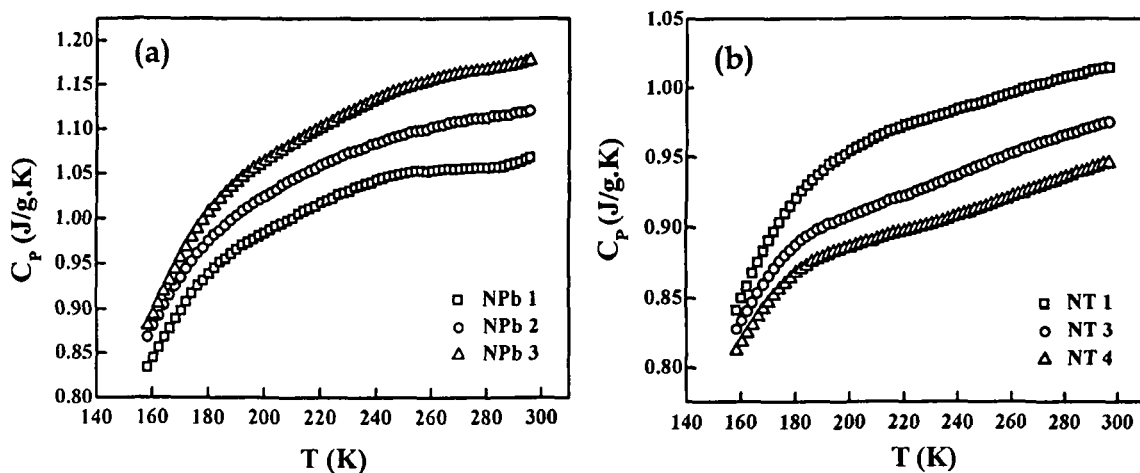


Figure 6.10: Specific heat as a function of temperature for (a) DBSA doped PANI nanoparticles and (b) CSA doped PANI nanotubes.

The specific heat contribution in this temperature regime comes from the localized harmonic vibrational modes. The localized phonons will result in an Einstein-type vibration i.e., localized harmonic oscillation with a specific frequency [282]. Considering optical phonon frequency in conducting polymers to be $\sim 3.6 \times 10^{13} \text{ s}^{-1}$ [238], the Einstein temperature $\theta_E (= h\omega/2\pi k_B)$ is found to be $\sim 275 \text{ K}$. Thus, it can be concluded that the high-temperature ($> 150 \text{ K}$) vibration modes (i.e. optical phonons) are presumably Einstein-type. At present, we cannot tell much about the variation of C_P as a function of doping level and dopants.

6.5 Summary

In summary, based on the thermal conductivity studies of different PANI nanostructures, viz., HCl doped nanofibers and nanoparticles, DBSA doped nanoparticles and CSA doped nanotubes, we have validated the order-disorder model for conjugated polymers, which predicts that conducting polymers are composed of ordered (crystalline) regions surrounded by disordered (amorphous) regions. The low-temperature ($< 100 \text{ K}$) thermal conductivity exhibits a peak reflecting the crystallinity while in the high temperature region ($> 100 \text{ K}$), thermally activated hopping of localized optical phonons confirm the amorphous nature of the polymer. Phonons appear to be the only carriers of heat in these PANI systems. The Debye temperature of the nanostructures is found to be in the range of $240 - 300 \text{ K}$. Extended acoustic phonons are the carriers of heat in the low temperature region. Localized optical phonons, anharmonically coupled to the extended modes perform hops from one site to another carrying heat in the high temperature regime. The anharmonic coupling constant is found to be comparatively less in the higher doped PANI-CSA nanotubes, and is attributed to a reduced disorder which is related to a decreased localization of optical phonons. Measured specific heat shows a rapid increase upto a temperature $\sim 200 \text{ K}$ for all the samples. Above 200 K , specific heat increases rather gradually up to a measured temperature range of 300 K .

The specific heat contribution in this temperature regime is due to localized harmonic vibration modes i.e., optical phonons. The morphology of the nanostructures has not been found to affect the thermal conduction in these PANI systems, although the interface between the nanostructures might scatter the phonons affecting the heat conduction. More studies, both theoretical and experimental, taking into account the morphological aspects of the nanostructures, are required to get a better picture of heat conduction in different nanostructures of conducting polymers.

CHAPTER 7

Magnetic properties of polyaniline nanostructures

This chapter embodies the magnetic properties of polyaniline nanostructures. The magnetization as a function of temperature and magnetic field has been investigated in detail to understand the magnetic behaviour of the charge carrying species in these nanostructures. The effect of dopant type and doping level on the magnetic properties of the nanostructures has also been presented.

7.1 Introduction

Despite the extensive works on conducting polyaniline (PANI), the nature of charge transport and charge carriers is still not fully understood [283, 284]. The complexity in charge transport in this class of materials arises due to an admixture of various factors, such as metal-insulator transition, change in properties of electronic states as a result of protonation, effect of disorder and Coulomb interaction [285]. The major issue that influences the charge transport is the character of disorder, whether homogeneous or inhomogeneous, that results in localization of charge carriers [119, 286]. Besides electrical conductivity, static magnetic susceptibility is also very sensitive to carrier localization. Magnetic susceptibility studies can provide important details of charge carrying species and unpaired spins. The static magnetic susceptibility changes from a temperature dependent Curie-type to a temperature independent Pauli-type paramagnetic susceptibility. While the localized electron spins contribute mostly to Curie-type susceptibility, the Pauli-type

susceptibility is realized due to a contribution from delocalized conducting electrons [284]. Therefore, changes in number of conducting electrons due to doping will presumably leave a mark on electrical conductivity. As a consequence, the magnetic susceptibility is also expected to be modified accordingly.

As discussed, undoped PANI is amorphous from crystallographic consideration. Proton doping in this system results in the formation of crystalline regions, which are conducting by its nature. However, these conducting regimes are separated by insulating amorphous regions rendering a coexisting phase. It is believed that charge carriers in the amorphous regions are localized, while they remain delocalized in the crystalline regions. Further, it has been reported that the charge carriers in protonated PANI are predominantly localized in the amorphous regions giving rise to local moments, and a relatively small fraction of the carriers with extended wavefunctions are found in the crystalline parts of the material [287]. Therefore, considering the different nature of magnetic susceptibility arising from localized and delocalized electrons, the susceptibility measurements prove to be a good probe to reveal the microscopic nature of the charge carriers [288].

Magnetic susceptibility studies have been previously used to understand the nature of charge carriers. For instance, a coexistence of polarons (spin) and bipolarons (spinless) has been shown for non-degenerate ground state polymers such as polyaniline [289, 290] and polypyrrole [291, 292]. In case of PANI and its derivative compounds, magnetic susceptibilities have been extensively studied. A transition from Curie-type to Pauli-type susceptibility has been reported, that supports the order-disorder model [293-295]. Moreover, the Pauli susceptibility, which gives a measure of the finite density-of-states (DOS) at the Fermi level, has been shown to be linearly proportional to the level of protonation for HCl and H₂SO₄ doped PANI [275, 296, 297]. However, contradicting results have also been reported, indicating a decrease in susceptibility with the doping of PTSA, SSA and NSA for PANI materials [289,

298]. A transition from polaron lattice to bipolaron lattice with doping has been suggested with polarons being more stable at low doping levels and bipolarons that at high doping levels [299]. The magnetic properties of PANI have also been found to be strongly affected by the dopant (inorganic or organic) type as well as level of doping [298].

In this chapter, a sincere effort has been made to understand the magnetic behavior of different PANI nanostructures doped with both organic and inorganic acids, viz., HCl doped nanofibers (NF) and nanoparticles (NPa), DBSA doped nanoparticles (NPb) and CSA doped nanotubes (NT)) as a function of temperature and field. The nanostructures have been synthesized by changing the doping level. The different samples have been numbered in increasing order of doping level (details are given in section 3.2 of Chapter 3). A transition from Curie to Pauli-type paramagnetism is observed for all the nanostructures. The magnetization vs. field curves at 10 K show linear behavior at low fields while at higher field values, the curve deviates from linearity.

7.2 Temperature dependence of magnetic susceptibility

The magnetic susceptibility (χ) has been obtained from the magnetization data in the temperature range of 2 - 300 K at 10 kOe magnetic field. The experimentally obtained χ values have been normalized to a two-ring repeat unit of PANI. Usually, the total dc magnetic susceptibility in conducting polymers is contributed by three factors i.e., the atomic core diamagnetic susceptibility (χ_{core}), the Pauli-like paramagnetic susceptibility (χ_P) and the Curie-like paramagnetic susceptibility (χ_C) [300]. Out of these, χ_{core} and χ_P are the temperature independent contributions, while the local moment χ_C exhibits an inverse temperature form. The experimentally obtained magnetic susceptibility data has been corrected for the diamagnetic contributions of the atomic core (χ_{core}) using Pascal constants [301]. The χ_{core} for emeraldine base is -106×10^{-6} emu/mol-2 ring [302], χ_{core} (Cl) is -25×10^{-6} emu/mol, χ_{core} (DBSA) is -257.56×10^{-6} emu/mol and χ_{core} (CSA) is -182.22×10^{-6} emu/mol.

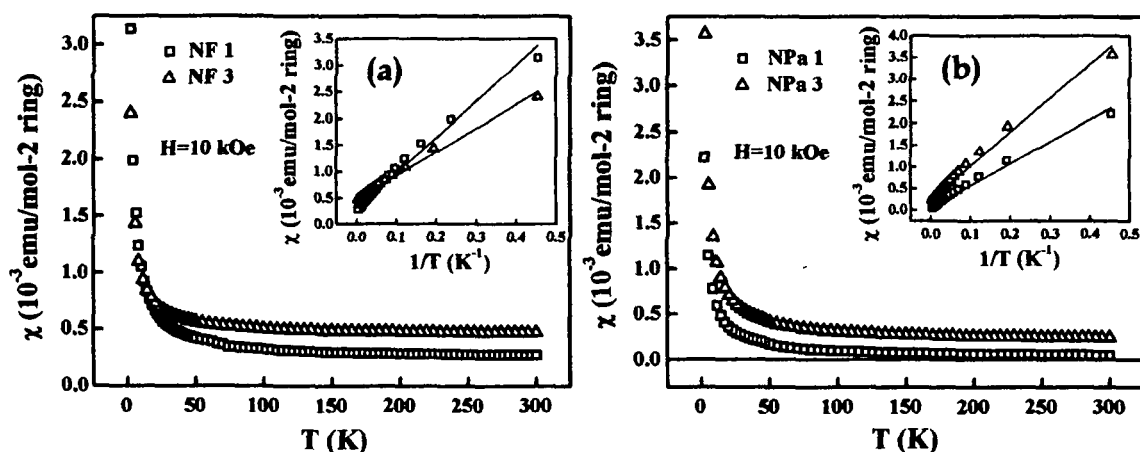


Figure 7.1: Temperature dependent variation of magnetic susceptibility has been shown for HCl doped PANI (a) nanofibers and (b) nanoparticles. Inset shows the linear fitting according to Eq. (7.1).

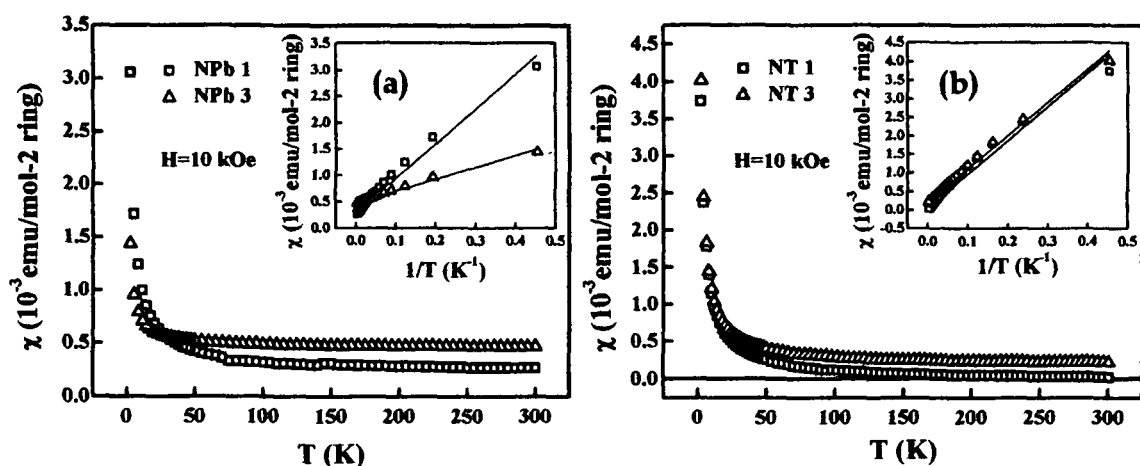


Figure 7.2: Magnetic susceptibility of (a) DBSA doped PANI nanoparticles and (b) CSA doped PANI nanotubes, has been shown as a function of temperature. Inset shows the linear fitting according to Eq. (7.1).

Figures 7.1 (a & b) show the temperature dependence of χ for HCl doped PANI nanofibers and nanoparticles, while Figures 7.2 (a & b) show the temperature dependence of χ for DBSA doped PANI nanoparticles and CSA doped PANI nanotubes, respectively. A clear transition from Curie-type to Pauli-type paramagnetic susceptibility is observed from the figures for all the nanostructures. The transition occurs at around 50 K and the magnetic

susceptibility values are almost the same for all the nanostructures. The temperature independent Pauli susceptibility arises from the delocalized charge carriers in the crystalline regions giving a measure of the metallic character, while the temperature dependent Curie susceptibility arises from the localized or trapped charges in the amorphous regions which correspond to the non-metallic character of the polymer. Thus, the magnetic susceptibility can be written as the sum of χ_P and χ_C :

$$\chi = \chi_P + \chi_C = \chi_P + \frac{C}{T} \quad (7.1)$$

where C is the Curie constant. χ_P can be determined from the intercept of the plot of χT vs. T . From χ_P , the density-of-states at the Fermi level $N(E_F)$ can be obtained as:

$$\chi_P = \mu_B^2 N(E_F) \quad (7.2)$$

where μ_B ($= 9.27 \times 10^{-21}$ erg/Oe) is the Bohr magneton. The χT vs. T plots of the respective nanostructures are plotted in the inset of Figures 7.1 (a & b) and Figures 7.2 (a & b). χ_P and C are obtained from the slope and intercept of χT vs. T plots, respectively. $N(E_F)$ values obtained using Eq. (7.2) and C values of all the nanostructures are given in Table 7.1.

From Table 7.1, it is observed that the value of $N(E_F)$ is in the range of 1.3 - 7.5 states/eV-2 rings. Such high values of $N(E_F)$ have not been observed for similar doped bulk PANI materials, where typical value reported for HCl doped PANI is 1.6 states/eV-2 rings [303], 2.39 states/eV-2 rings for CSA doped PANI and 2.61 states/eV-2 rings for DBSA doped PANI [304]. Only exception has been reported for amorphous BF_3 doped PANI, where $N(E_F)$ is found to be 15.2 states/eV-2 rings [305]. Such high value of delocalized carriers associated with crystalline regions suggests very high intrinsic conductivity. This result can also be associated with the low values of Mott temperature T_0 signifying less disorder in the present PANI samples (Table 5.1 of Chapter 5). It is very interesting to note that among all the same molar concentration doped PANI

(NF 1, NPa 1, NPb 1 and NT 3), $N(E_F)$ value is highest for the CSA doped nanotubes which shows the highest conductivity (discussed in section 5.2 of Chapter 5) as compared to the other doped nanostructures. χ^P and hence $N(E_F)$ gives a good estimate of the intrinsic metallic nature of the polymer, which the bulk conductivity often fails to measure as it is governed by inter-chain, inter-particle, inter-grain boundaries of the sample. It can also be observed from the table that the $N(E_F)$ value increases with doping irrespective of the type of the dopant, whether organic or inorganic.

Table 7.1: Value of density of states at the Fermi level [$N(E_F)$] and Curie constant (C) of the nanostructures.

Sample	$N(E_F)$ (eV/states-2 ring)	C (emu.K/mol)
HCl doped nanofibers		
NF 1	4.2	0.0068
NF 3	7.2	0.0044
HCl doped nanoparticles		
NPa 1	1.6	0.0050
NPa 3	7.5	0.0077
DBSA doped nanoparticles		
NPb 1	4.2	0.0065
NPb 3	7.2	0.0022
CSA doped nanotubes		
NT 1	1.3	0.0090
NT 3	6.5	0.0089

The data from magnetic measurements rather support well the results of electrical conductivity measurements discussed in Chapter 5. The enhancement of temperature independent Pauli susceptibility with doping or protonation in the present study is similar to the previous studies of protonated PANI, where the result has been described following a model which suggests a segregation of

unprotonated insulating and protonated metallic regimes in the polymer [275]. With protonation, metallic phases are promoted and insulating phases diminish, resulting in an enhanced conductivity. The increase of temperature independent Pauli susceptibility and the decrease of temperature dependent Curie susceptibility on protonation strongly support this model implying the increase of protonated metallic phases.

7.3 Field dependence of magnetization

Isothermal magnetization (M) as a function of magnetic field (H) of the nanostructures has been measured in the magnetic field range upto ± 70 kOe at 10 K. Figures 7.3 (a & b) represent the $M(H)$ curves of HCl doped PANI nanofibers and nanoparticles, respectively and Figures 7.4 (a & b) depict the $M(H)$ curves of DBSA doped PANI nanoparticles and CSA doped PANI nanotubes, respectively. It can be observed from the figures that throughout the whole magnetic field range, the higher doped sample exhibits greater magnetization. Among all the doped nanostructures, CSA doped nanotubes exhibit higher value of magnetization for the same concentration of dopant signifying larger number spins i.e., more carriers are generated in CSA doped PANI. This result identifies CSA as an efficient dopant protonating more $-N=$ sites, as compared to HCl or DBSA. It is to be noted from the figures that with increasing magnetic field, the magnetization increases almost linearly at low magnetic fields (upto 10 kOe). However, at higher magnetic fields, magnetization deviates from linear behavior. This probably originates from the enhanced atomic core diamagnetic contribution and/or due to Langevin function parameter which adds non-linearity to magnetic behavior at enhanced field value. According to Langevin theory of paramagnetism, the magnetization, M is expressed as: $M/M_s=L(A)$, where M_s is the saturation value of magnetization, $L(A)$ is the Langevin function with argument $A = \mu_m H/k_B T$, where μ_m is the atomic magnetic moment, k_B is the Boltzmann constant and T is the temperature [306]. The Langevin function is expanded as $L(A) = A/3 -$

$A^3/45 + 2A^5/945 - \dots$. For a smaller value of A , $L(A)$ can be approximated upto $L(A) = A/3$, hence $M/M_s = \mu_m H/3k_B T$ which shows a linear field dependence of magnetization. However, at higher A value non-linear term in $L(A)$ comes into play, rendering a non-linear $M(H)$. It becomes obvious that a combination of low temperature and high magnetic field causes a high value of A and consequently a non-linear $M(H)$.

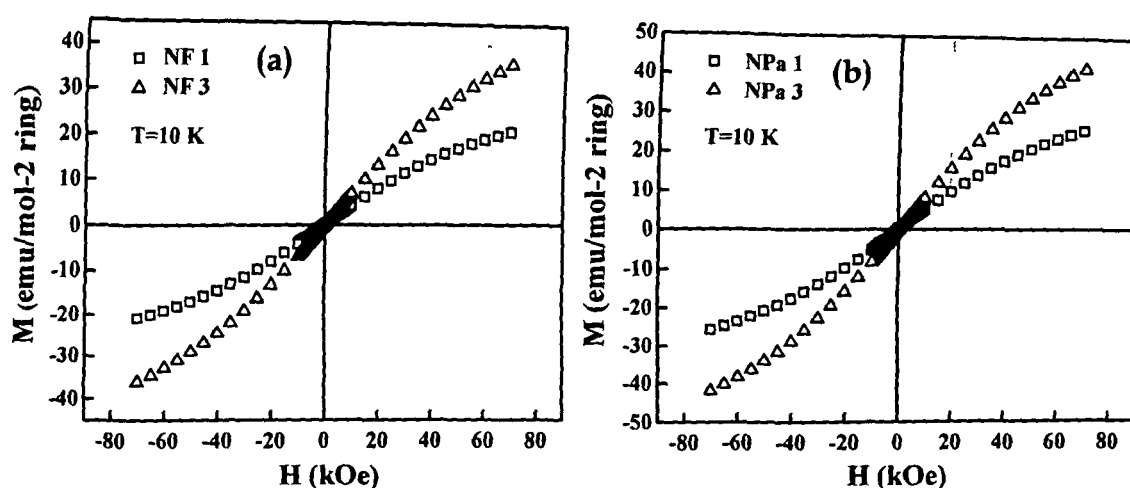


Figure 7.3: Magnetization vs. field plots of HCl doped PANI (a) nanofibers and (b) nanoparticles.

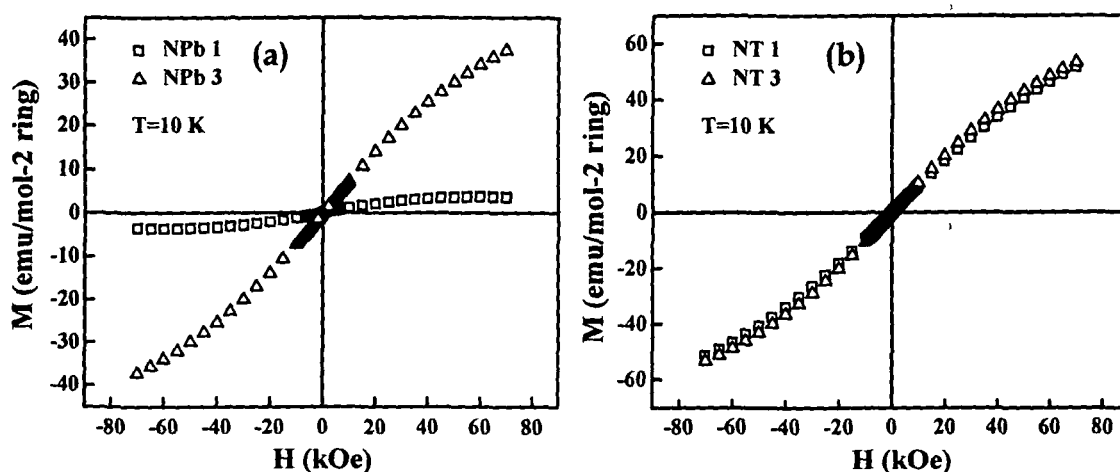


Figure 7.4: Plots of magnetization vs. field for (a) DBSA doped PANI nanoparticles and (b) CSA doped PANI nanotubes.

In the present study, $M(H)$ data have been collected at low temperature i.e., at 10 K. At lower fields, it is evident from the Figures (7.3 and 7.4), that magnetization increases almost linearly showing a paramagnetic nature. However, as field increases $M(H)$ becomes non-linear for all the samples, though the onset field for non-linearity is different for different samples. Therefore, the high-field $M(H)$ behavior can be explained with Langevin theory of paramagnetism. Nonetheless, an enhanced diamagnetic contribution from atomic core cannot be ruled out completely, and the non-linearity can be attributed to both the effects discussed above. Finally, no remnant magnetization is observed, which is indicative of the paramagnetic nature of the polymer and confirms polaron as the major charge carrier in PANI. Similar behavior, even magnetization reducing to zero at high fields has been reported for doped PANI materials [298, 307].

7.4 Summary

In summary, temperature and field dependent magnetization measurements have been performed on different PANI nanostructures, viz., HCl doped nanofibers and nanoparticles, DBSA doped nanoparticles and CSA doped nanotubes. A clear transition from Curie to Pauli susceptibility at ~ 50 K is observed. The Curie spins arise from the localized carriers in the amorphous regions while the Pauli spins come from the delocalized carriers in the crystalline regions. The Pauli susceptibility gives a measure of $N(E_F)$ and hence the intrinsic metallic conductivity of the polymer. CSA doped nanotubes exhibit the highest value of $N(E_F)$ indicating more metallic character. With doping, the metallic phases are promoted while the insulating phases diminish. The magnetization vs. field curves at 10 K exhibit linear behavior at low fields (upto ~ 10 kOe) while at high fields (> 10 kOe), the curves deviate from linearity. The non-linearity arises due to the increased diamagnetic contribution of atomic core and/or Langevin function parameter which adds non-linearity to the magnetic behavior at higher field values. For higher doped samples, the

magnetization is found to be higher indicating an enhancement in the number of carriers with doping. The value of magnetization is found to be highest in the CSA doped nanotubes, which confirms CSA to be an efficient dopant in comparison to HCl and DBSA. Dopant type, whether organic or inorganic does not affect the magnetic properties. Morphology of the nanostructures has not been found to affect the magnetic behavior of the PANI nanostructure systems.

CHAPTER 8

Conclusions and future prospects

This chapter outlines the main conclusions drawn from the present work. The scope of future studies in the emerging field of conducting polymer nanostructures have also been discussed briefly at the end of this chapter.

8.1 Conclusions

The present work deals with the synthesis, characterization, and studies of electrical and thermal transport, and magnetic properties of polyaniline (PANI) nanostructures, namely, nanofibers, nanoparticles and nanotubes synthesized by interfacial polymerization and self-assembly methods. PANI nanofibers doped with hydrochloric acid (HCl) were synthesized by interfacial polymerization technique. PANI nanoparticles doped with hydrochloric acid and dodecyl benzene sulfonic acid (DBSA), and camphor sulfonic acid (CSA) doped PANI nanotubes were synthesized by self-assembly method. The effect of doping level and dopant type on the properties has also been investigated. The major conclusions drawn from the present work are given below:

1. High resolution transmission electron microscopy (HRTEM) reveals the size of the nanostructures. The average diameter of the HCl doped nanofibers is found to be 11.5 nm while that of the HCl doped nanoparticles is found to be 3 nm. The length of the fibers varies from a few nanometers to several micrometers. The diameter of the nanoparticles did not change with doping as the concentration of the surfactant (sodium dodecyl sulfate, SDS) used for

controlling the morphology was kept constant. In interfacial polymerization, the diameter of the fibers depends on the dopant acid used and not on the concentration; hence no change in size is observed. The average size of the DBSA doped nanoparticles increases with doping from 6 to 35 nm. The average inner and outer diameters of the CSA doped nanotubes also increase with doping. The inner diameter increases from 38 to 91 nm while the outer diameter increases from 99 to 142 nm with doping. DBSA and CSA being functional dopants, where they act both as dopants as well as structure directing agents, their increasing concentration leads to an increase in micellar size and consequently the diameter of the nanostructures increases.

2. X-ray diffraction studies of the nanostructures reveal the characteristic peaks of PANI at $2\theta = 20^\circ$ and $2\theta = 25^\circ$ ascribed to the parallel and perpendicular periodicity of the chains, respectively. The intensity of the peaks is found to increase with doping indicating the increase in ordering of chains. The crystallinity is found to be highest for the CSA doped nanotubes which is attributed to the hydrogen bonding between C=O group of CSA and N-H group of PANI chains. The peak at $2\theta = 6.4^\circ$ which arises due to the periodicity between dopant counterion and N atom of PANI is found to increase in case of the nanofibers indicating that the ordering takes place along the length of the fibers. This peak is not observed for the higher doped CSA nanotubes which is attributed to the larger size of the CSA counterions that disrupts the ordering.
3. Vibrational spectra of the PANI nanostructure systems were studied using Fourier transform infrared spectroscopy (FTIR) and Raman spectroscopy. Both FTIR and Raman spectroscopy indicate polaron as the major charge carriers in these PANI systems, and the peak corresponding to delocalized polarons increases with doping. Raman spectroscopy confirms the formation of ES-I type crystalline structure of PANI. In Raman spectra, the peak corresponding to $C_{\text{ring}}-N-C_{\text{ring}}$ torsion angle increases with doping

indicating the decrease in the torsion angle. This decrease in torsion angle improves the π -stacking of the PANI chains which is favorable for charge transport. Further, the Raman peak corresponding to C–C stretching increases while that of C=C decreases with doping. This indicates a transformation of quinoid rings into benzenoid rings with doping and that at higher doping levels; the benzenoid rings are more in concentration.

4. DC conductivity studies performed in the temperature range of 5 - 300 K indicated different charge transport mechanisms for the different PANI nanostructures. The conduction mechanism depends on the dopant counterions and the morphology of the nanostructures. The nanostructures exhibit metal-insulator transition at ~ 20 K. The metallic behavior below 20 K is attributed to the Hartree contribution of electron-electron interaction effects. For the CSA doped nanotubes, the conduction in the insulating regime appear to occur by Mott's quasi one-dimensional variable-range hopping (VRH).

The conduction in the insulating regime of the HCl doped nanofibers and nanoparticles, and DBSA doped nanoparticles is fractal-like i.e., the electronic states are superlocalized. The conduction in the HCl doped nanofibers occurs by VRH among superlocalized states without Coulomb interaction while that for the HCl and DBSA doped nanoparticles, the conduction occurs by VRH among superlocalized states with Coulomb interaction. The superlocalization of the electronic states in case of the HCl doped nanostructures is ascribed to the small size of the dopant counterion Cl^- . Due to the small size of Cl^- , the PANI chains orient in a random manner and make the system porous forcing the charge hopping to take fractional dimensions unlike the CSA doped nanotubes. CSA counterion being bulky in size fills up the interstitial space between the polymer chains, and the hydrogen bonding between C=O group of CSA and N–H group of PANI aligns the chains, leading to Mott's quasi one-dimensional VRH. For the case

of DBSA doped nanoparticles, the long alkyl chains of DBSA counterion makes the polymer porous and hence the conduction fractal-like. The Coulomb interaction between the initial and final states dominates the charge transport in case of the nanoparticles, which is attributed to the small size and confined morphology. The Coulomb interaction is not observed in case of nanofibers or nanotubes. This has been attributed to an extended spatial dimension leading to greater probability of hopping of carriers to distant sites and hence decreasing the effect of the interaction.

The conductivity observed is highest for the CSA doped nanotubes and lowest for the DBSA doped nanoparticles. The better alignment of PANI chains in CSA doped nanotubes is the reason for high conductivity, while the larger inter-chain spacing of the chains due to the long alkyl chains of DBSA counterion leads to lower inter-chain hopping probability and hence less conduction. Disorder is found to be amply reduced which is indicated by the lower values ($\sim 10^2$ K) of characteristic temperature of hopping T_0 as compared to that observed in earlier studies, where T_0 is $\sim 10^4$ K. The reduction in disorder is attributed to the nanodimensional control of synthesis.

5. The isothermal magnetoresistance (MR) has been measured at five different temperatures of 30 K, 50 K, 100 K, 200 K and 300 K and magnetic field upto 8 T. A temperature-induced modification in the nature of MR from positive to negative is observed above around 100 K. Both the positive and negative MR increases monotonically with magnetic field. With doping, positive MR decreases while the negative MR increases. This change in sign of MR with temperature is qualitatively understood using the bipolaron model which was originally proposed to explain organic magnetoresistance (OMAR). General charge transport in conducting polymers occurs through hopping of polarons. With the application of increasing field, the spin state of two polarons in consideration, forcefully attains a triplet state which is not

favorable over the singlet state that is seen as the natural spin configuration at zero magnetic fields, to form a bipolaron. At low temperatures with less thermal energy, therefore polarons exhibit reduced mobility to avoid forming bipolarons in the presence of magnetic field, which explains the positive *MR* in these materials. With increasing temperature, however, higher thermal energy helps the polarons to hop to distant unoccupied sites, avoiding the already occupied neighboring sites. The applied field in this case helps higher distant hopping adding more conduction which favors a negative *MR*.

6. Isothermal current-voltage characteristics in the potential range of 0 - 5 V and temperature range of 80 - 300 K were carried out to determine the mobility of the carriers and the influence of disorder on conduction. Ohmic behavior prevails in the low-voltage region (< 1 V) while trap-free space-charge-limited conduction occurs in the high-voltage (> 1 V) region. The highest mobility is observed for the CSA doped nanotubes attributed to better ordering of PANI chains which corroborates well with the XRD and dc conductivity results. The mobility is dependent on field and temperature exhibiting the universal Poole-Frenkel behavior. The field activation parameter is found to be negative for all the nanostructures except for the CSA doped nanotubes, indicating the dominance of structural disorder over energetic disorder. For the CSA doped nanotubes, the field activation parameter changes from negative to positive value with doping indicating that the structural disorder is reduced which is supported by the XRD results. The disorder parameters were extracted employing the uncorrelated and correlated Gaussian disorder models. Doping reduces the structural disorder but enhances the energetic disorder. Increasing doping leads to an increase in the number of carriers, and also the counterions that maintains the charge neutrality. The Coulombic interaction between the dopant

counterions and charge carriers act as charge trapping centers broadening the density-of-states (DOS) tail.

7. Thermal conductivity (κ) measurements were carried out in the temperature range of 10 - 300 K to understand the nature of carriers and mechanism of heat transport. Phonons appear to be the major heat carriers in these PANI systems, as the electronic contribution to κ is found to be quite insignificant. At low temperatures around 30 K, κ exhibits a peak reflecting the crystalline nature of the nanostructures. The peak value decreases with doping indicating an increase in phonon scattering centers in the form of dopant counterions. The Debye temperature of the nanostructures is found to be in the range of 240 - 300 K. On the higher temperature side above 100 K, a quasi-linear increase of κ with T indicates the presence of amorphous regions. The κ vs. T curves thus validates the order-disorder model of conducting polymers which proposes the existence of ordered (crystalline) and disordered (amorphous) regions in these polymers. Above 100 K, the conduction occurs by thermally activated hopping of localized optical phonons via anharmonic coupling with the extended acoustic phonons. Acoustic phonons are responsible for heat conduction in the lower temperature (< 100 K) side while the optical phonons are responsible for heat conduction in the higher temperature (> 100 K) side.

The value of anharmonic coupling constant (C_{eff}) is found to be relatively less in the higher doped PANI-CSA nanotubes and is ascribed to the reduction of disorder, which in turn reduces the localization of optical phonons. The reduced disorder in the CSA doped nanotubes is supported by the XRD results. The specific heat measurements were carried out in the temperature range of 158 - 300 K. The specific heat is found to increase rapidly upto ~ 200 K and then increases gradually to a saturation value. The specific heat contribution in this temperature regime is due to the localized harmonic vibrational modes i.e., the optical phonons.

8. Magnetic susceptibility (χ) measurements carried out at 10 kOe magnetic field in the temperature range of 2 - 300 K, showed a transition from Curie-type to Pauli-type paramagnetism at ~ 50 K. The Curie spins arise from the localized carriers in the amorphous regions while the Pauli spins come from the delocalized carriers in the crystalline regions. The susceptibility is found to increase with doping. Pauli susceptibility gives a measure of the density-of-states at the Fermi level, $[N(E_F)]$ and hence the intrinsic metallic character, which is not reflected in the bulk conductivity studies due to the dominance of inter-chain, inter-particle and inter-grain resistance of the samples. The $N(E_F)$ values (1.3 - 7.5 states/eV-2 rings) are found to be quite high in comparison to that reported for bulk samples (1.6 - 2.6 states/eV-2 rings). Such high values of $N(E_F)$ correspond to a larger concentration of delocalized carriers in the crystalline regions and hence very high intrinsic conductivity. This is due to the sufficient reduction in disorder indicated by the lower T_0 values from the dc conductivity results. For the same level of doping, $N(E_F)$ is found to be highest for the CSA doped nanotubes indicating more metallic nature and supports the dc conductivity results as well. With doping, $N(E_F)$ increases indicating that the protonated metallic phases are promoted and the unprotonated insulating phases diminished.

The magnetization vs. field curves at 10 K in the range of 0 - 70 kOe exhibit linear behavior at low fields (upto ~ 10 kOe) while at high fields (> 10 kOe), the curves deviate from linearity. The non-linearity arises due to the enhanced atomic core diamagnetism and/or Langevin function parameter adding non-linearity at high fields. The magnetization values are high for the higher doped nanostructures. CSA doped nanotubes exhibit larger values of magnetization indicating CSA to be an efficient dopant as compared to HCl and DBSA, protonating more $-N=$ sites. The curves show no remnant magnetization indicating paramagnetic behavior of the spins confirming that the polarons are the major charge carriers in PANI.

8.2 Future prospects

Conducting polymer nanostructures have unique properties as they combine the characteristics of conducting polymers and the merits of nanostructures. These properties can be exploited for their better performance in devices. The disordered nature of conducting polymers is a limitation for use of these materials for application purposes. However, it has been observed from the present thesis that the control of synthesis at the nanoscale has adequately reduced the disorder. Single conducting polymer nanostructures would be more ordered as compared to their bulk counterpart, which would lead to efficient performance of the nanodevices. Although, the effect of nanostructuring has been observed in our studies, the study of transport properties in single nanostructures is required for use of these materials as nanodevices. The thermal conductivity studies presented in this thesis are completely new and have not been explored earlier. The results have been explained using models available for crystalline and amorphous systems for different temperature regions. Theoretical studies are required to understand the heat transport behavior in the whole temperature range. Specific heat measurements could not be conducted below 158 K due to experimental limitations. Further experimental and theoretical studies are required to understand the behavior of specific heat in the low temperature side. The temperature dependence studies of thermal conductivity and specific heat in other conducting polymers such as polypyrrole, polythiophene and poly(3,4-ethylenedioxythiophene) to understand the heat transfer mechanism can also be potential future research problems.

References

1. Shirakawa, H., et al. Synthesis of Electrically Conducting Organic Polymers: Halogen Derivatives of Polyacetylene, $(\text{CH})_x$, *J. Chem. Soc. Chem. Commun.* 578-580, 1977.
2. Saxena, V., and Malhotra, B. D. Prospects of conducting polymers in molecular electronics, *Curr. Appl. Phys.* **3**(2-3), 293-305, 2003.
3. Ryu, K.S., et al. Redox supercapacitor using polyaniline doped with Li salt as electrode, *Solid State Ionics* **152-153**, 861-866, 2002.
4. Snook, G.A., et al. Conducting-polymer-based supercapacitor devices and electrodes, *J. Power Sources* **196**(1), 1-12, 2011.
5. Argun, A.A., et al. Multicolored Electrochromism in Polymers: Structures and Devices, *Chem. Mater.* **16**(23), 4401-4412, 2004.
6. Mortimer, R.J., et al. Electrochromic organic and polymeric materials for display applications, *Displays* **27**(1), 2-18, 2006.
7. McQuade, D.T., et al. Conjugated Polymer-Based Chemical Sensors, *Chem. Rev.* **100**(7), 2537-2574, 2000.
8. Sotomayor, P.T., et al. Construction and evaluation of an optical pH sensor based on polyaniline-porous Vycor glass nanocomposite, *Sensors and Actuators B* **74**(1-3), 157-162, 2001.
9. Baughman, R.H. Conducting polymer artificial muscles, *Synth. Met.* **78**(3), 339-353, 1996.
10. Jager, E.W.H., et al. Microfabricating conjugated polymer actuators, *Science* **290**(5496), 1540-1545, 2000.
11. Joo, J. and Lee, C.Y. High frequency electromagnetic interference shielding response of mixtures and multilayer films based on conducting polymers, *J. Appl. Phys.* **88**(1), 513-518, 2000.

12. Wang, Y. and Jing, X. Intrinsically conducting polymers for electromagnetic interference shielding, *Polym. Adv. Technol.* **16**(4), 344-351, 2005.
13. Wu, C.-Q. and Sun, X. Nonlinear optical susceptibilities of conducting polymers, *Phys. Rev. B* **41**(18), 12845-12849, 1990.
14. Sarmah, S. *Development of conducting polymer based nanocomposites for multifunctional applications and swift heavy ion irradiation studies*, Ph.D. Thesis, Tezpur University, Assam, India, 2011.
15. Peierls, R.E. *Quantum theory of Solids*, Oxford University Press, Oxford, 1955.
16. Kiebooms, R., et al. Synthesis, electrical and optical properties of conjugated polymers, in *Handbook of Advanced Electronic and Photonic Materials and Devices*, H.S. Nalwa, ed., Academic Press, San Diego, CA, 2001, Vol. 8, p. 1-86.
17. Chiang, C.K. et al. Conducting polymers: Halogen doped polyacetylene, *J. Chem. Phys.* **69**(11), 5098-5104, 1978.
18. Murthy, N.S., et al. A hexagonal structure for alkali metal doped poly(p-phenylene), *Solid State Commun.* **78**(8), 691-695, 1991.
19. Gurunathan, K., et al. Electrochemically synthesised conducting polymeric materials for applications towards technology in electronics, optoelectronics and energy storage devices, *Mater. Chem. Phys.* **61**(3), 173-191, 1999.
20. Freund, M.S. and Deore, B.A. *Self-Doped Conducting Polymers*, John Wiley and Sons Ltd, United Kingdom, 2007.
21. Bredas, J.L., and Street, G.B., Polarons, bipolarons, and solitons in conducting polymers, *Acc. Chem. Res.* **18**(10), 309-315, 1985.
22. Bredas, J. L., et al. The role of mobile organic radicals and ions (solitons, polarons and bipolarons) in the transport properties of doped conjugated polymers, *Synth. Met.* **9**(2), 265-274, 1984.

23. Scott, J.C., et al. Electron-spin-resonance studies of pyrrole polymers: Evidence for bipolarons, *Phys. Rev. B* **28**(4), 2140-2145, 1983.
24. Bredas, J.L. Bipolarons in doped conjugated polymers: A critical comparison between theoretical results and experimental data, *Mol. Cryst. Liq. Cryst.* **118**(1), 49-56, 1985.
25. Banerjee, S. *Synthesis, swift heavy ion irradiation and characterization of conducting polymer based nanostructured materials for biomedical and sensor applications*, PhD Thesis, Tezpur University, Assam, India, 2012.
26. Heeger, A.J., et al. Solitons in conducting polymers, *Rev. Mod. Phys.* **60**(3), 781-850, 1988.
27. Pasveer, W.F. *Charge and energy transport in disordered π -conjugated systems*, PhD Thesis, Eindhoven University of Technology, Eindhoven, The Netherlands, 2004.
28. Philips, P.J. Polymer crystals, *Rep. Prog. Phys.* **53**(5), 549-604, 1990.
29. Campbell, I.H. and Smith, D.L. Physics of polymer light-emitting diodes, in *Semiconducting Polymers: Chemistry, Physics and Engineering*, G. Hadziioannou and P.F. van Hutten, eds., Wiley-VCH, Weinheim, 2000, p. 333-363.
30. Losio, P.A. *Charge transport and mirrorless lasing in organic semiconductors*, PhD Thesis, ETH Zürich, Zürich, Switzerland, 2007.
31. Heeger, A.J., et al. Solitons in conducting polymers, *Rev. Mod. Phys.* **60**(3), 781-850, 1988.
32. Mott, N.F., Conduction in glasses containing transition metal ions, *J. Non-Cryst. Solids* **1**(1), 1-17, 1968.
33. Conwell, E.M. Impurity band conduction in germanium and silicon, *Phys. Rev.* **103**(1), 51-61, 1956.
34. Shklovskii, B.I. and Efros, A.L. *Electronic Properties of Doped Semiconductors*, Springer, Berlin, 1984.
35. Sheng, P., et al. Hopping conductivity in granular metals, *Phys. Rev. Lett.* **31**(1), 44-47, 1973.

36. Levy, Y.E. and Souillard, B. Superlocalization of electrons and waves in fractal media, *Europhys. Lett.* **4**(2), 233-237, 1987.
37. Van der Putten, D., et al. Evidence for superlocalization on a fractal network in conductive carbon-black-polymer composites, *Phys. Rev. Lett.* **69**(3), 494-497, 1992.
38. Mott, N.F. and Davis, E. *Electronic Processes in Non-Crystalline Materials*, Clarendon Press, Oxford, 1979.
39. Gill, W.D. Drift mobilities in amorphous charge-transfer complexes of trinitrofluorenone and poly-*n*-vinylcarbazole, *J. Appl. Phys.* **43**(12), 5033-5040, 1972.
40. Bäessler, H. Charge transport in disordered organic photoconductors a monte carlo simulation study, *Phys. Stat. Sol. B* **175**(1), 15-56, 1993.
41. Dunlap, D.H., et al. Charge-dipole model for the universal field dependence of mobilities in molecularly doped polymers, *Phys. Rev. Lett.* **77**(3), 542-545, 1996.
42. Gommans, H.H.P. *Charge transport and interface phenomena in semiconducting polymers*, PhD Thesis, Eindhoven University of Technology, Eindhoven, The Netherlands, 2005.
43. Anderson, P.W. Absence of diffusion in certain random lattices, *Phys. Rev.* **109**(5), 1492-1505, 1958.
44. Mott, N.F. Review lecture: Metal-insulator transitions, *Proc. R. Soc. Lond. A* **382**(1), 1-24, 1982.
45. Tzamalīs, G. *Optical and transport properties of polyaniline films*, PhD Thesis, University of Durham, Durham, United Kingdom, 2002.
46. Zallen, R. *The Physics of Amorphous Solids*, Wiley, New York, 1983.
47. Lee, P.A. and Ramakrishnan, T.V. Disordered electronic systems, *Rev. Mod. Phys.* **57**(2), 287-337, 1985.
48. Kim, B.-J., et al. Preparation of polyaniline nanoparticles in micellar solutions as polymerization medium, *Langmuir* **16**(14), 5841-5845, 2000.